Chair of Nonferrous Metallurgy

Doctoral Thesis

Recycling of chromium-containing residues from the stainless steel industry with a focus on the reduction kinetics

Dipl.-Ing. Manuel Leuchtenmüller, BSc

February 2019

AFFIDAVIT

I declare on oath that I wrote this thesis independently, did not use other than the specified sources and aids, and did not otherwise use any unauthorized aids.

I declare that I have read, understood, and complied with the guidelines of the senate of the Montanuniversität Leoben for "Good Scientific Practice".

Furthermore, I declare that the electronic and printed version of the submitted thesis are identical, both, formally and with regard to content.

Date 12.02.2019

Signature Author
Manuel, Leuchtenmüller
Matriculation Number: 01035193

Acknowledgement

The investigations and the experimental studies of the present thesis were conducted at the Chair of Nonferrous Metallurgy at Montanuniversitaet Leoben within the group for recycling of heavy-metal-containing by-products.

My special thanks go to Jürgen Antrekowitsch for giving me the opportunity to do a PhD and being part of his research group. During all the time Jürgen not only supported and helped in scientific questions, but also encouraged me to work on demanding projects like the construction of a small-scale electric arc furnace, the implementation and testing of different measurement technologies or the development of a temperature controller for one of the Chair's induction furnaces. Additionally, Jürgen made it possible to take part in conferences around the world for scientific exchange, which were great experiences that included lots of interesting discussions.

Further thanks go to Helmut Antrekowitsch head of the Chair for Nonferrous Metallurgy, for providing ideal conditions for a researcher with a wide range of opportunities regarding experimental setups in the melting lab. At the same time, I would like to thank Thomas Link and Erich Troger who always helped with their expertise whenever adaptations were required in order to improve the quality of an experimental setup. Furthermore, I would like to thank all of my colleagues during the past years for many encouraging and creative talks.

Special thanks also go to my corporate partner voestalpine Boehler Edelstahl GmbH & Co KG for the support during the past years. Dr. Christoph Fasching always offered his help and gave constructive feedback when proofreading my works, which was great because I got a different perspective on the results I obtained.

My greatest thanks also go to my parents, Claudia and Ernst Leuchtenmüller for their never-ending support and assistance during all my time at the university.

Finally, and most importantly, I want to thank Sofia Riedl for her help in terms of proofreading as well as assisting and having the necessary patience during the time I worked on this thesis, which definitely helped me a lot.

Acronyms

AOD	Argon Oxygen Decarburization
EAF	Electric Arc Furnace
EOC	Extent of Conversion
ESRF	Electric Smelting Reduction Furnace
HSM	Hot Stage Microscopy
ICP	Inductively Coupled Plasma
MS	Mass Spectroscopy
PID Controller	Proportional Integral Differential Controller
PLC	Programmable Logic Controller
RHF	Rotary Hearth Furnace
SEM	Scanning Electron Microscopy
SPI	Serial Peripheral Interface
STA	Simultaneous Thermal Analysis
TGA	Thermogravimetric Analysis
XRD	X-Ray Diffraction
ZEWA	Zero Waste

Abstract

During the production of stainless steel, a significant amount of by-products such as slags, dusts and mill scale are generated. These materials contain heavy metal compounds, which is why they generally have to be landfilled, although some of them have – compared to natural materials used in the construction sector – similar properties. Chromium is a widely used alloying element in stainless steel production and because of its high affinity for oxidation, chromium can be found in all oxidic by-products. Austria's legislation limits the maximum chromium concentration in solid materials to 0.25 % for its application in road construction. The legislative limit for other construction sectors is even lower. This is the reason why slags from stainless steel production have to be treated in order to lower the chromium oxide concentration to less than 0.25 %.

Treatment concepts can be divided into pyrometallurgical, hydrometallurgical and mechanical approaches. The most promising one is the carbothermic reduction of a liquid slag because it can extract metal inclusions as well as elements in oxidic form; hence, pyrometallurgical methods yield low final heavy metal concentrations in the treated materials when done properly. In order to achieve high recovery rates, all oxidic compounds have to be fully dissolved in a liquid slag. Thermodynamic calculations of the theoretical equilibrium between chromium and chromium oxide in a carbothermic reduction process showed that the process temperature has to be at least 1,600 °C. Additionally, the oxide activity and slag viscosity are assumed to have an influence on the achievable final concentration.

Small-scale trials that were performed in an induction furnace pointed out that the final concentrations depend on the treatment duration, which is why the whole treatment process was assumed to be limited kinetically. Therefore, kinetic investigations were performed to get information about the necessary treatment time dependent on the process temperature. Since the process temperature has a major influence on the reaction rate, an exact control was necessary. For this task, a temperature controller was developed. The evaluation of trials in the melting lab led to the development of a kinetic model that describes the reaction rate for a specific chromium oxide concentration and temperature. This can be used to estimate the necessary time to reach a desired concentration for a given starting concentration. Experiments in the EAF were performed to get information about the influence of the furnace type on the reduction kinetics. While the chromium concentration course showed a similar course – this means the speed-limiting step of the reaction mechanism seems to be comparable – an exact comparison was not possible, because the furnace lacks an accurate temperature control system.

Kurzfassung

Während der Edelstahlherstellung fallen neben dem Hauptprodukt auch sogenannte Nebenprodukte wie Schlacken, Stäube, Zunder und Ähnliches an. Diese Materialien weisen üblicherweise erhöhte Schwermetallkonzentrationen auf, weshalb sie aus heutiger Sicht zumeist einer Deponierung zugeführt werden. Während so einerseits Deponieflächen verbraucht werden, erfordert beispielsweise der Straßenbau den Abbau von natürlichen Rohstoffen, obwohl für denselben Zweck eben solche Reststoffe verwendet werden könnten. Die meisten Edelstahllegierungen beinhalten Chrom, dass aufgrund seines unedlen Charakters in weiterer Folge – in zumeist überwiegend oxidischer Form – auch in allen Nebenprodukten der Edelstahlproduktion zu finden ist. Die österreichische Gesetzgebung hat in der Recycling-Baustoffverordnung für Stahlwerksschlacken eine maximale Chromkonzentration von 0,25 % definiert, was auch für Schlacken aus dem Edelstahlbereich als oberstes Limit für eine Verwertung anzusehen ist. Unbehandelt überschreiten die Materialien aus dem Edelstahlbereich diese Konzentration, weshalb vor der Verwertung ein Aufbereitungsschritt erforderlich ist.

Aufbereitungskonzepte können grundsätzlich in pyrometallurgische, hydrometallurgische und mechanische Verfahren eingeteilt werden. Im Rahmen der Dissertation hat sich die karbothermische Schmelzbehandlung als vielversprechendstes Aufarbeitungsverfahren erwiesen, da hierbei nahezu alle Wertmetalle in Form einer Ferrolegierung rückgewinnbar sind und nur geringe Schwermetallkonzentrationen in der oxidischen Restphase verbleiben. Um hohe Rückgewinnungsraten zu erreichen, ist neben einer hohen Temperatur – thermodynamischen Berechnungen zufolge etwa 1.600 °C – auch auf eine hohe Oxidaktivität, niedrige Viskosität sowie eine optimierte Liquidustemperatur zu achten.

Um den Temperatureinfluss auf die notwendige Behandlungsdauer zu beschreiben, wurden in einem Induktionsofen kinetische Untersuchungen durchgeführt. Da ursprünglich keine genaue Kontrolle der Prozesstemperatur möglich war, musste neben der Möglichkeit zur kontinuierlichen Temperaturmessung auch eine Temperaturregelung entwickelt werden. Die Auswertung der kinetischen Untersuchungen führte zur Bestimmung eines kinetischen Modells, das die Berechnung der notwendigen Behandlungsdauer bei einer gegebenen Temperatur und Chromoxidkonzentration ermöglicht.

Abschließend wurden Versuche in einem eigens konstruierten Lichtbogenofen durchgeführt, um die Ergebnisse aus dem Induktionsofen zu überprüfen. Allerdings erwies sich die Implementierung einer genauen Temperatursteuerung als schwierig. Zwar führten die Versuche im Elektrolichtbogenofen zu ähnlichen Konzentrationsverlaufen für Chromoxid in der Schlacke wie im Induktionsofen, allerdings war ein exakter Vergleich der Reaktionskinetik aufgrund der nicht genau bekannten Temperaturverhältnisse nicht möglich.

Table of Contents

1 Introduction

The production and processing of metals is a high energy consuming industrial sector with an enormous demand for natural resources that generates by-products which often have to be landfilled. The production volumes increased at high rates during the past decades for nearly all metals, leading to an increasing negative impact on the environment. The dumping of by-products does not only increase the amount of land use, but also causes pollution of large areas when not done properly. An example is the Ajka alumina plant accident that happened in Hungary in 2010.

Nowadays, social and environmental responsibility requires the sustainable management of natural resources as well as a strong emphasis on lowering the quantity of materials that have to be landfilled. This situation forced the metallurgical industry and their research partners to spend huge effort to the development of methods and processes to reuse the by-products as resources in other industries or to recycle valuable compounds in order to decrease both the quantity of landfilled materials and the amount of raw materials required in the production process. Blast furnace slag is an example of a by-product that is reused as a raw material in the construction industry. Its range of application is wide and extends from road construction and the cement industry to hydraulic engineering. However, not all wastes can simply be reused in other industrial areas because some materials contain environmentally harmful compounds. This is the reason why a lot of them – like residues from the stainless steel industry that contain many different elements – still have to be landfilled. The composition of the by-products from the stainless steel industry is influenced by the alloying elements used. These elements are contained not only in the produced steel, but also in the by-products, generally in the form of oxides. Some oxides are harmful, which is why they have to be treated as hazardous waste. One of the most problematic elements that prevent the recycling and reuse of stainless steel residues is chromium. It is used as an alloying element because it increases the steel's corrosion resistance. However, in most waste streams such as slags, dusts and sludges, it is present in oxidic form. The hexavalent form has a carcinogenic effect, which leads to strict legislative requirements how stainless steel wastes have to be handled and limits the range of application possibilities, especially in the European Union. Therefore, these wastes have to be treated in order to remove or stabilize the potentially toxic elements in the form of harmless compounds. The recent development of environmental legislation forces the complete removal of these elements, which is why the present thesis focuses on the toxic compounds' removal; laboratory leaching tests may not include all possible long-term effects. The removal of toxic compounds from one material enriches it in another one. Consequently, the removal does not only prevent environmental problems, but also generates

an ecological benefit due to the generation of another product. This can be used in order to develop a zero waste approach. Such a recovery can be done in a mechanical, hydrometallurgical or pyrometallurgical way.

In 2017, 48.1 million tons of stainless steel were produced [1]. The production goes hand in hand with the generation of electric arc furnace slag, transfer ladle slag, AOD slag, dust, refractory bricks and mill scale. Table 1 shows that the slags represent the waste stream with the highest amount that is produced. However, the other substances' amounts are also notable.

Table 1: Specific amount of generated waste streams [2]

Solid waste	**Quantity (kg per ton of liquid steel)**
Electric arc furnace slag	100-135
Transfer ladle slag	3040
AOD slag	160
Dust	10-20
Refractory bricks	2-8
Mill scale	10-30 (per ton of rolled steel)

Slags mainly consist of slag-building compounds like lime, quartz, alumina and magnesia. Additionally, some reducible substances such as iron oxide, manganese oxide and chromium oxide can be found. Their concentrations range between 1 % and 5 %. Dust mainly consists of reducible compounds such as iron oxide, zinc oxide, chromium oxide, nickel oxide and so on. The composition of mill scale follows the rolled stainless steel grade's composition. Refractory bricks contain some metal and slag inclusions. Compared to slags, dust and mill scale contain fewer stable slag-building compounds. Therefore, their recycling has to focus on the recovery of valuable elements. In contrast, slag and refractory bricks contain little value, which is why their recovery has to focus on their reuse as a construction material. However, in order to be allowed to utilize slag for the production of asphalt, Austria's legislation limits the maximum chromium concentration in solid materials to 0.25 %. This already represents a special regulation for steelworks slag only. It limits the application to the utilization as an aggregate in asphalt. In order to be able to utilize the slags in other areas of application, the chromium concentrations in the solid must be lower than 90 ppm. Thus, a direct application of slags as a construction material is not possible. The present thesis describes recovery concepts with a focus on a pyrometallurgical approach.

1.1 Recovery Concepts

Possible recovery concepts can be divided into

- pyrometallurgical,
- hydrometallurgical and
- mechanical techniques.

While the pyrometallurgical approach can generally be described as a high energy-consuming concept, it enables the most flexibility regarding the products' quality. Not only does it allow for the utilization of many different residues in a single process, but it also allows the possibility of influencing the resulting slag's properties precisely. In contrast, the hydrometallurgical approach requires less energy, but generates a sludge that is hardly marketable. Finally, the mechanical separation techniques focus on the recovery of metal inclusions. The following section gives a short overview of the different techniques.

1.1.1 Mechanical Approach

Mechanical processes can be used to separate metal inclusions from a mainly oxidic material. Considering the tapping procedure in the electric arc furnace and AOD converter, metal droplets get trapped in the slag. These metallic particles have – compared to the oxides – different physical properties. Therefore, they can be recovered with the help of physical separation methods. Normally, such a treatment includes a crushing or grinding step that liberates the metal inclusions from the oxidic matrix. For small-size inclusions, a wet grinding process is necessary in order to achieve a satisfying recovery rate. A separation step that uses the different physical properties can be applied accordingly. Examples of physical separation methods are centrifugation, sedimentation, gravity separation and magnetic separation. The recovery of metals from oxides often uses magnetic separation because it represents an effective technique. [3,4]

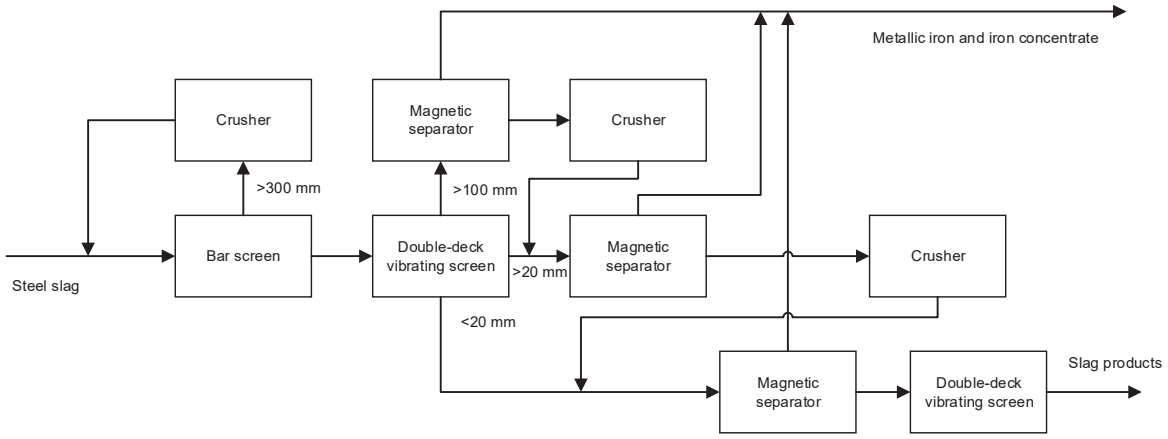

Figure 1: Recovery of metal from steel slag via mechanical methods [3]

The mechanical approach requires less energy – especially compared to the pyrometallurgical processes – which is why the processing costs are lower. However, the technique has some downsides. First of all, it is only applicable to separate substances regarding their physical properties – usually metals from oxides. This is why it is hardly suitable for dust or scale. Additionally, the crushing and grinding steps generate a fine-grained slag that is – without further processing – hardly marketable in the construction sector. Finally, solely physical separation is not to remove potential toxic compounds such as hexavalent chromium oxide. This is in line with a closed plant that was built in 2013 and finally had to be shut down after two years of operation, because it turned out that the resulting slag fraction was hardly marketable [5].

1.1.2 Hydrometallurgical Approach

The hydrometallurgical approach aims for the recovery of valuable elements by leaching them. Processes have mainly been developed for the leaching of steel works dust. The methods differ in the applied leaching solutions that are used. Different acids and alkalis are suitable for the leaching of steel works dust. Examples are sulfuric acid, hydrochloric acid, ammonium chloride, etc. The suggested methods differ in the solutions' concentrations and the leaching temperatures. The main difficulty is the selective leaching of zinc. It is hardly possible to achieve satisfying recovery for zinc without leaching zinc ferrite. If zinc ferrite dissolves, the solution enriches with iron, which requires its removal. This is normally done by a precipitation step. Although it is technically possible, the precipitation lowers the economic feasibility of the whole process. [6]

1.1.3 Pyrometallurgical Approach

A pyrometallurgical recovery process can include solid, liquid and gaseous phases. Depending on the waste characteristics, different approaches have been established. Some waste materials contain high concentrations of valuable elements, which is why their recovery can be done in an economical way. The Waelz process can be seen as an example of such a recovery process. The treatment is done in a Waelz kiln, where a zinc-containing dust fraction is fed. The zinc oxide is then reduced by carbon and vaporizes into the kiln atmosphere, where it is re-oxidized to fine zinc oxide particles which are transported via the off-gas system to a bag house filter system that collects them. This filter dust represents the main product of the process and is called Waelz oxide. However, the process also generates a slag phase that is high in iron and contains minor concentrations of heavy metals. As a result, it is hardly marketable, which is why it has to be dumped, especially when dust from the stainless steel industry is used as a feed material.

This is exactly why the industry strives for a better solution. One approach is the development of a treatment process for the Waelz slag. Another approach can be seen in the replacement

of the Waelz kiln by another process. A new process should be flexible regarding the feed material and involve the zero waste approach. Examples of concepts are listed below; a detailed explanation and discussion can be found in the referring literature [7–10]:

- the rotary hearth furnace (RHF) process
- the electric smelting reduction furnace (ESRF) process
- the Zero-Waste (ZEWA) process
- and the Primus process

2 Hydrometallurgical Leaching Tests

In the context of the recycling of residues from the stainless steel industry, hydrometallurgical processes have been developed especially for the recovery of steel works dust. This chapter provides an overview of some suggested leaching methods. Leaching experiments were executed in order to evaluate their usability for a stainless steel dust. Generally, only little literature is available for the hydrometallurgical recovery of dust from stainless steel production, the reason being that these dusts generally contain less zinc. Additionally, the complex composition caused by the various alloying elements makes selective leaching difficult.

2.1 Leaching Processes

The first step of a hydrometallurgical treatment method is the leaching of zinc. The main goal is a high recovery of zinc with low dissolution of other compounds in order to avoid complex leach purification steps.

2.1.1 Ammonium Chloride Leaching

This method is based on a patent from 1974 and processes the dust in an ammonium chloride solution which dissolves zinc, copper, nickel, lead and cadmium. The leaching reaction is shown in Equation 2.1. Both iron oxide and zinc ferrite only have low solubility in the solution, so it remains in the solid leach residue. For this reason, a small share of zinc bound in the form of zinc ferrite is required to reach high recovery rates. The solution is cleaned via a cementation step with metallic zinc powder. This leads to the precipitation of copper, lead and cadmium; the corresponding reaction can be explained with Equation 2.2. After a solid-liquid separation, the solution mainly contains zinc. Its solubility in the ammonium chloride decreases with decreasing temperature. Hence, the solution is cooled in order to precipitate zinc in the form of zinc oxide. The crystallized zinc oxide contains – depending on the input material – approximately 2 % of chlorine, which is why an additional washing step is necessary in order to reduce the chlorine content. Figure 2 gives a detailed flow chart of the whole procedure [11].

$$ZnO + 2NH_4Cl \rightarrow Zn(NH_3)_2Cl_2 + H_2O \quad (2.1)$$

$$[Pb, Cu, Cd](NH_3)_2Cl_2 + Zn \rightarrow Zn(NH_3)_2Cl_2 + Pb, Cu, Cd \quad (2.2)$$

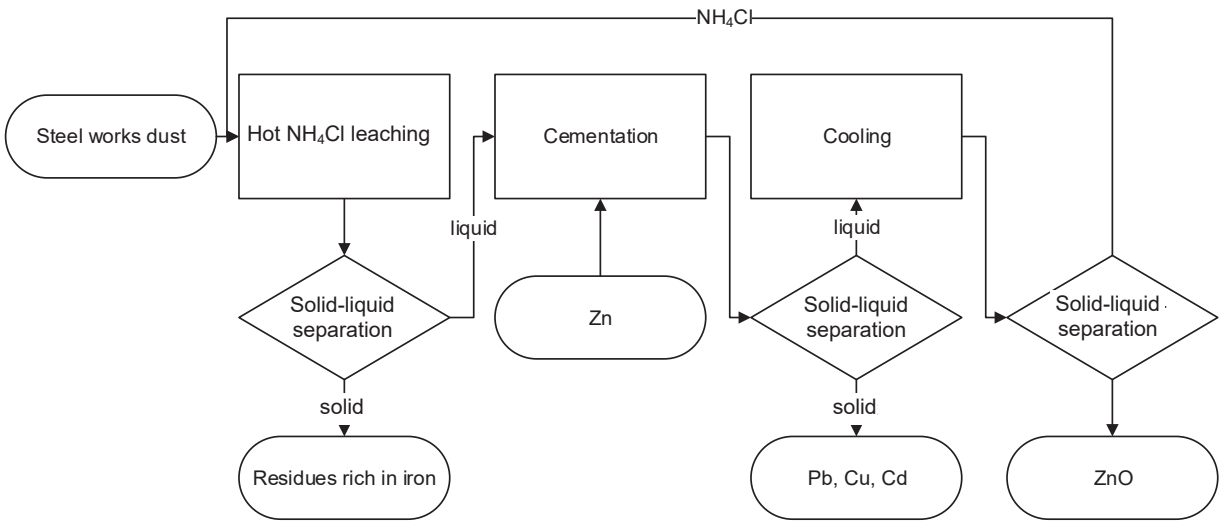

Figure 2: Flow chart for an ammonium chloride leaching procedure

2.1.2 EZINEX Process

The EZINEX process constitutes a modification of the ammonium chloride leaching method. In contrast to the formation of crystalline zinc oxides as described for the process above, the EZINEX process extracts metallic zinc by electrolytic deposition on a titanium cathode, as shown in Equation 2.3. On the graphite anode, the presence of chloride ions usually leads to the formation of chlorine gas (Equation 2.4). This is prevented by a continuous supply of ammoniac that reacts immediately with the formed chlorine gas to hydrochloric acid and nitrogen, as described in Equation 2.5. Finally, the overall reaction leads to Equation 2.6. [12]

Cathode: $Zn(NH_3)_2Cl_2 + 2e^- \rightarrow Zn + 2NH_3 + 2Cl^-$ 2.3

Anode I: $2Cl^- \rightarrow Cl_2 + 2e^-$ 2.4

Anode II: $Cl_2 + \frac{2}{3}NH_3 \rightarrow 2HCl + \frac{1}{3}N_2$ 2.5

Overall reaction: $Zn(NH_3)_2Cl_2 + \frac{2}{3}NH_3 \rightarrow Zn + \frac{1}{3}N_2 + 2NH_4Cl$ 2.6

The electrolysis uses a current density of 300 to 400 A/m² and a zinc concentration of 1020 g/l in the electrolyte. The pH-value has to be in the range between 5.8 and 6.5 in order to prevent the formation of chloramines. In comparison to the electrolysis in sulfuric acid, the cell voltage is lower, which to some extent pays off the higher costs of the NH_3. [12]

Impurity accumulation in the electrolyte requires a continuous purification of the solution. The main impurities to enrich in the solution are mainly alkali chlorides, fluorides, calcium and magnesium. The fluorides partially react with dissolved calcium to insoluble calcium fluoride, which regulates the content of fluorine in the leaching process and therefore prevents its

enrichment. Calcium and magnesium ions are usually precipitated in the form of carbonates by the addition of sodium carbonate. Figure 3 shows the overall flow chart for the EZINEX process. [12]

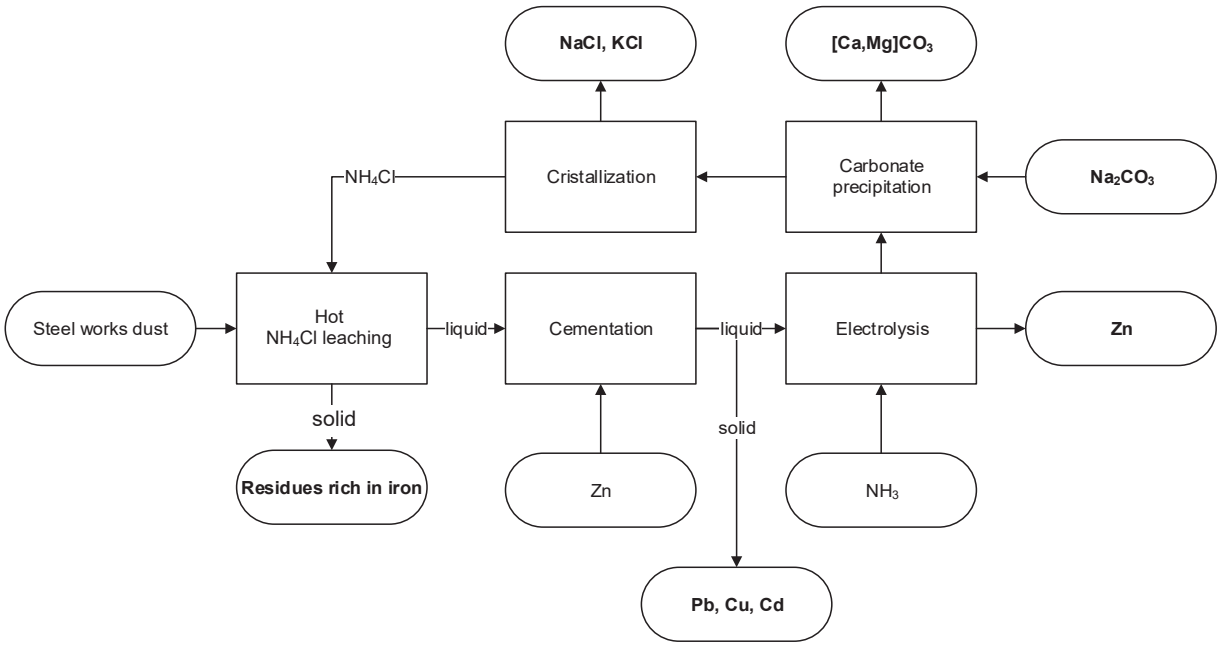

Figure 3 Flow chart of the EZINEX process [12]

2.1.3 ZINCEX Process

The ZINCEX process uses sulfuric acid for the dissolution of the zinc from steel works dust. The main purification and enrichment step is done via solvent extraction that serves as a barrier for numerous impurities. From the aqueous solution of the leaching step, the zinc is selectively extracted into an organic liquid and subsequently re-extracted into a solution with a higher H_2SO_4 concentration. The absorption capacity for zinc in the organic phase depends on the pH-value of the acid according to Le Chatelier, as shown in Equation 2.7. [13]

$$2RH + Zn^{2+} \leftrightarrow R_2Zn + 2H^+ \qquad 2.7$$

Since the zinc is leached selectively, impurities enrich in the aqueous solution from the leaching process. For this reason, a precipitation step is necessary in order to remove these elements from the solution. A flow chart of the whole leaching process can be seen in Figure 4. [13]

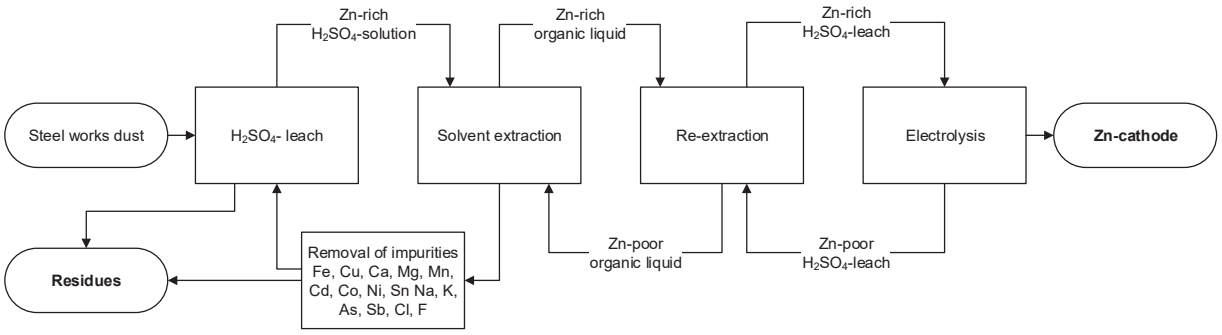

Figure 4: ZINCEX leaching process [13,14]

2.1.4 Soda Leaching

Soda leaching uses sodium carbonate for the leaching step of the residue. The sodium carbonate does not only dissolve zinc, but also lead, copper, cadmium and silicon. Figure 5 shows the flow chart of the Cebedeau process. After the leaching, the solid and liquid phases are separated via centrifugation. The solution undergoes a clarification step where calcium hydroxide is added to precipitate silicon in the form of calcium silicates. The next step is the cementation of more precious elements by the addition of metallic zinc. These elements are mainly lead, cadmium and copper. Additionally, unreacted zinc is present in the lead-enriched material. Metallic zinc is produced via electrolysis from the purified solution. Most of the electrolyte is used directly for a further leaching of steel works dust; however, a small fraction is evaporated in order to precipitate salts to control their concentration in the solution. [15,16]

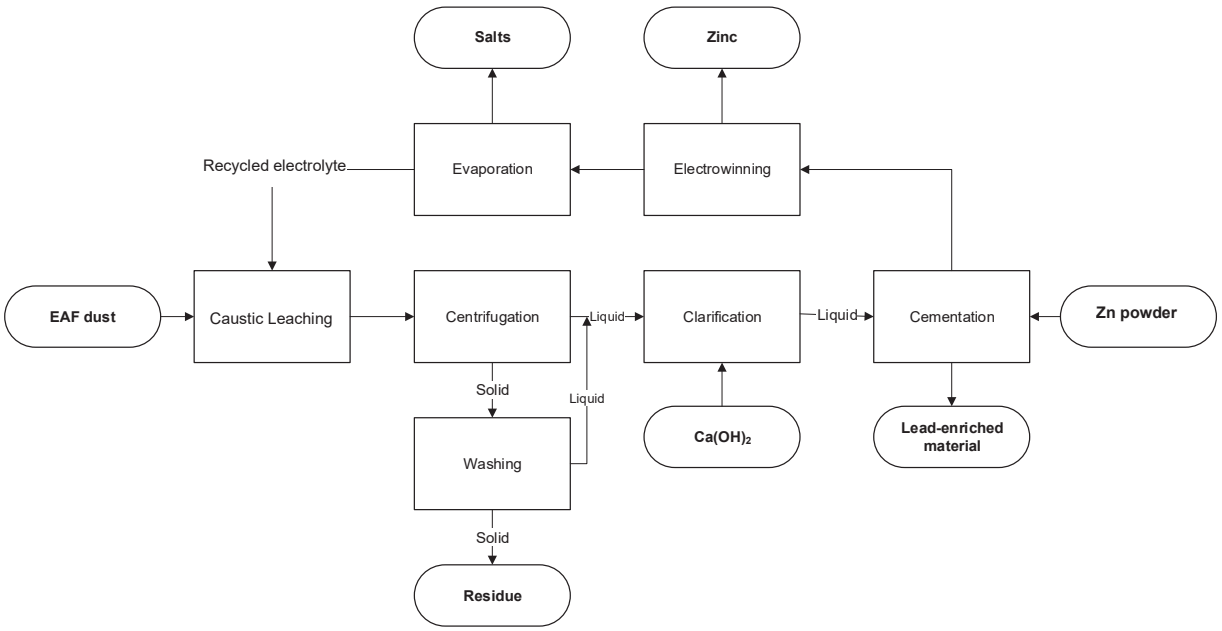

Figure 5: Flow chart of the Cebedeau process [15,16]

2.1.5 Further Leaching Methods

Literature describes more processes; however, the main steps are the same, as already described in this chapter. A more detailed explanation can be found in the referring literature. [15–19]

2.2 Leaching Experiments

The main goal of the hydrometallurgical approach is the recovery of zinc. According to the literature study in the previous chapter, the recovery rates mainly depend on the fraction of zinc bound in the form of zinc ferrite. Therefore, preliminary tests were run in the chemical laboratory to evaluate the potential of hydrometallurgical methods by determining the soluble fraction of zinc.

2.2.1 Leaching through Ammonium Chloride Solution

The ammonium chloride solution consisted of 87.5 g NH_4Cl in 350 ml H_2O. At a constant temperature of 90°C, a magnetic stirrer and 50 g of steel works dust were added. The solid-liquid separation was conducted by vacuum filtration. The solid residues were dried, ground, homogenized and subsequently analyzed by SEM-EDX. From this analysis, the leaching rates displayed in Figure 6 were calculated. The results point out that only 47 % of the zinc contained was leached. Similar leaching rates were achieved for copper, aluminum and magnesium. Additionally, some iron, chromium and manganese were dissolved.

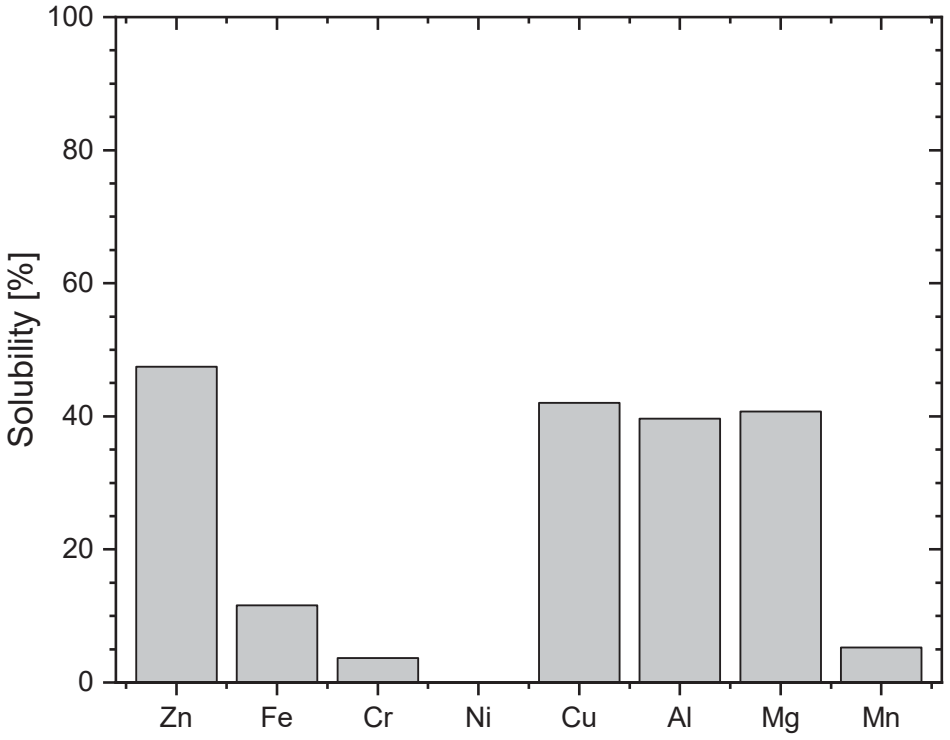

Figure 6: Solubility of different elements in an ammonium chloride leaching

2.2.2 Sulfuric Leaching

In addition to the ammonium chloride leaching, a sulfuric leaching procedure was performed. Sulfuric acid can not only leach zinc oxide, but also zinc ferrite when its concentration and temperature are increased. The solubility of zinc ferrite depends on the concentration and temperature. For this reason, experiments were conducted in the form of a so-called “neutral-leaching” with a sulfuric acid concentration of 15 g/l and a temperature of 50 °C as well as a so-called “hot-acidic leaching” with a sulfuric acid concentration of 120 g/l and a temperature of 95 °C. For both experiments, 50 g of steel works dust were leached in 350 ml solution. The leaching time for both trials was two hours. The solid-liquid separation was performed by vacuum filtration. The solid residues were dried, ground, homogenized and subsequently analyzed by means of REM- EDX. This analysis was used to calculate the leaching rates.

The leaching rates of the neutral leaching are displayed in Figure 7. The solubility of zinc reached 39 %, which is lower than the 47 % from the ammonium chloride leaching test. Other compounds show – compared to zinc – lower dissolution rates. While aluminum was dissolved during the ammonium chloride leaching, it remained in the leaching residue for the neutral leaching. In contrast, the dissolubility of iron, chromium and nickel increased.

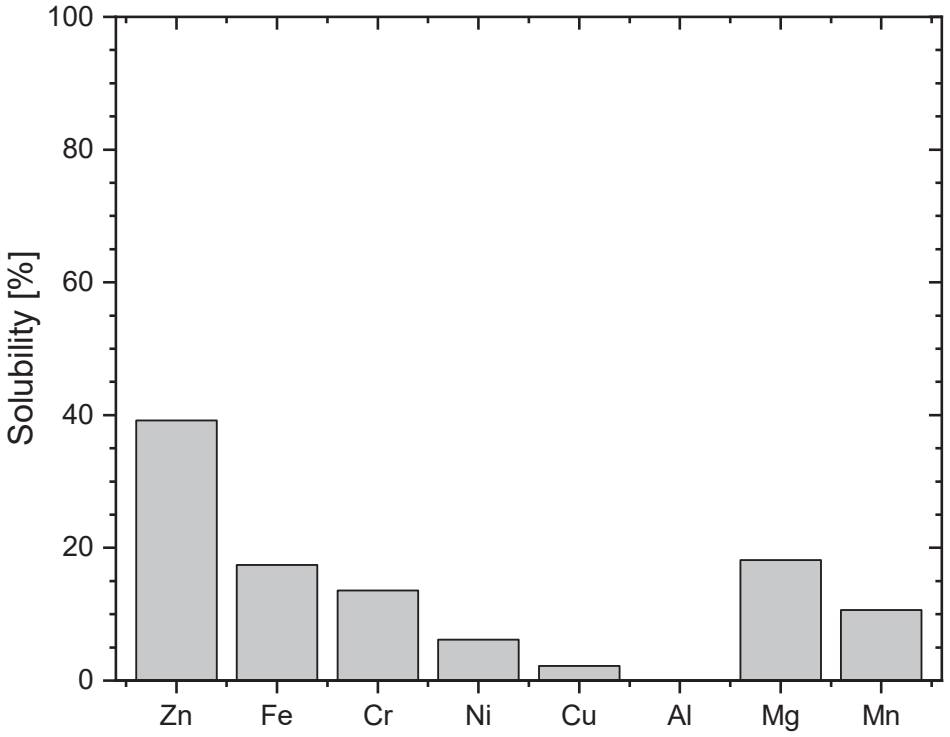

Figure 7: Solubility of different elements in a 15 g/l H_2SO_4 and 50 °C leaching

Finally, the results of the hot acidic leaching are displayed in Figure 8. The higher acid concentration in combination with the higher temperature led to a leaching rate of almost 90 % for zinc. The majority of other compounds present in the dust were dissolved, as well. Consequently, the solution produced requires a complex and expensive purifying step, which is why hot acidic leaching cannot be used to recover zinc from the stainless steel dust. The data from the sulfuric leaching tests performed can be used to estimate the amount of zinc that is bound in the form of zinc ferrite to about 50 %.

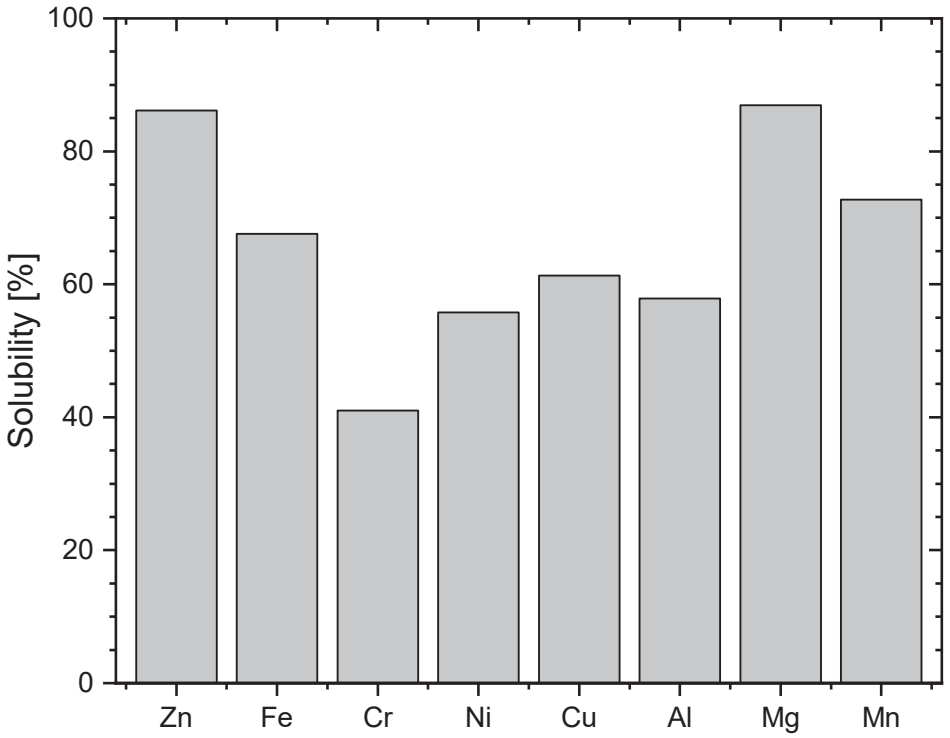

Figure 8: Solubility of different elements in a 120 g/l H_2SO_4 and 95 °C leaching

2.3 Conclusion

The preliminary tests show the difficulties that occur when applying hydrometallurgical methods to process dust from the stainless steel industry. On the one hand, the dissolution of zinc ferrite should be prevented because it requires an expensive precipitation step of iron. On the other hand, the sole dissolution of zinc that is not bound in zinc ferrite leads to low recovery rates. Within the sulfuric acid leaching experiments, the high acid concentration resulted in a complex solution that requires difficult and expensive purification steps. Additionally, dust from the stainless steel industry generally has lower concentrations of zinc compared to dust from carbon steel production. Finally, leaching and precipitation generate residues that once more require landfilling. Therefore, the hydrometallurgical processing has to be considered as a less promising approach, which is why further research was conducted using pyrometallurgical methods. However, if it is possible to physically separate the dust in order to get a higher zinc concentration with only small amounts of zinc ferrite, the hydrometallurgical approach has to be reevaluated.

3 Pyrometallurgical Fundamentals

The current thesis investigates a reduction treatment similar to the ZEWA process with a focus on the chromium oxide reduction. During the treatment, reducible compounds in the slag react with a reduction agent and form a metal phase, or if its boiling point is lower than the process temperature, it evaporates into the off-gas system. The technical feasibility has been demonstrated in the past; however, there is no data available on the reaction kinetics. Considering wastes from the stainless steel industry, chromium oxide can be described as one of the most challenging compounds. On the one hand, its reduction requires a higher reduction potential and on the other hand, environmental legislation dictates low concentration limits in the final product. As a result, the chromium oxide's reduction kinetics have a major influence on the economic feasibility of the whole process. For this reason, the following section describes the most important adjustable parameters of a smelting reduction treatment. These are:

- the process temperature
- the liquidus temperature
- the oxide activities
- the viscosity of the melt
- the reduction agent

3.1 Process Temperature

The temperature depends on the energy input, the heat capacity of the furnace and the fed materials, the experiment's duration and the heat losses. It can be easily adjusted by increasing the power input into the furnace. It affects the whole process in various ways.
First of all, it influences a chemical reaction's equilibrium. An increasing temperature shifts the equilibrium of an endothermal reaction in the direction of the products. The opposite applies for exothermal reactions. Equation 3.1 displays the endothermal carbothermic reduction of chromium oxide. [20–22]

$$Cr_2O_3 + 3C \leftrightarrow 2Cr + 3CO \tag{3.1}$$

An increased temperature allows for higher recovery rates in respect to chromium. The same is true for the oxides of iron, molybdenum, nickel, zinc, manganese and similar compounds that can be found within the stainless steel industry's wastes. Figure 9 shows the temperature's influence on the achievable reduction degree when assuming a pressure of 1 bar and using a stoichiometric amount of carbon as a reduction agent. The calculations do not consider the formation of carbides. The outlined data illustrates that chromium and manganese oxide require high process temperatures in order to obtain satisfying recovery rates. [21,22]

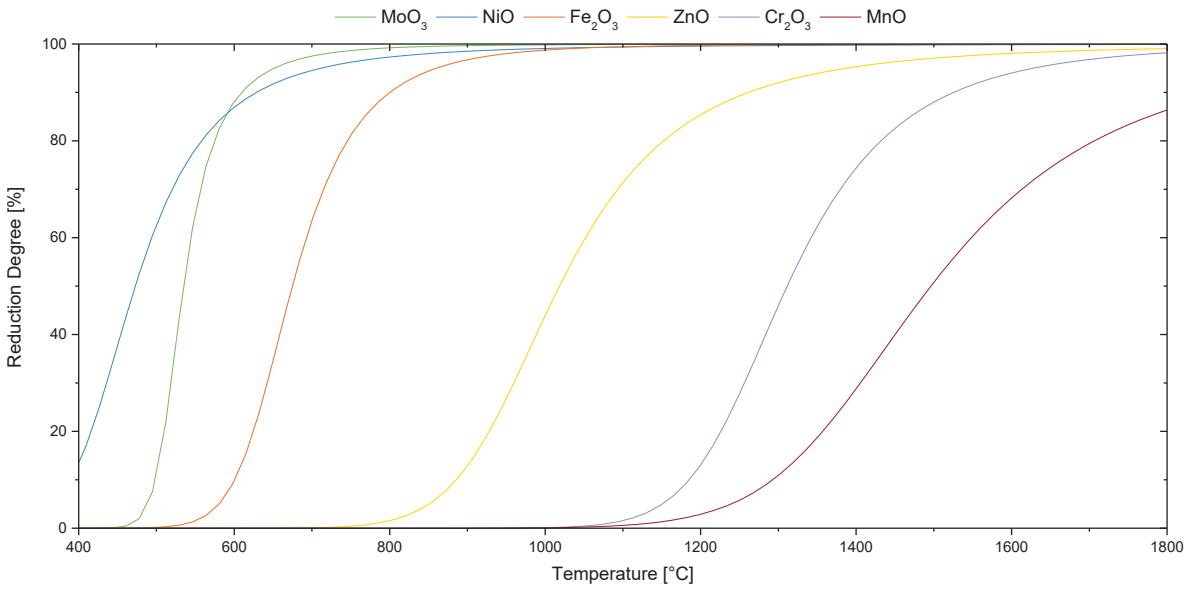

Figure 9: Calculated reduction degrees for the carbothermic reduction of various oxides from wastes in the stainless steel industry in respect to the temperature [21]

Secondly, the kinetics of chemical reactions are mainly determined by the temperature, because it affects the collision rate between atoms and molecules. Therefore, many chemical reactions follow an Arrhenius-like correlation. A detailed description of the kinetic fundamentals can be found later in Chapter 6.

Thirdly, in addition to a direct influence on the reaction kinetics, the temperature leads to a decrease in the melt's viscosity and thus indirectly increases the kinetics. This results from the fact that a lower viscosity means a better mobility of the liquids' ions. Additionally, better flowability is preferable for a good separation between the metal and slag phases, which can further improve the recovery rates. Apart from this, a lower viscosity goes hand in hand with higher diffusion rates for the ions that are present in the melt. A more detailed description is available in Chapter 3.4 [23]

Finally, the temperature affects the oxide activity coefficients, as described in Chapter 3.3.

3.2 Liquidus Temperature

The liquidus temperature is defined as the minimum temperature that is necessary to liquefy a substance so that no solid components are left. Regarding slags, the melting process usually starts with the formation of low-melting phases which subsequently dissolve the remaining solid compounds. If the temperature of a melt is higher than its liquidus temperature, all solid material is dissolved. If a melting reduction treatment takes place below the liquidus temperature, solid phases exist. These solids may contain valuable elements or compounds that are supposed to be recovered. Obviously, the recovery rate decreases when solid phases are present, because it requires the diffusion of different substances through the solid material.

Additionally, the separation between metal and slag is limited. Therefore, the liquidus temperature defines the lower limit of the process temperature. Depending on the process conditions, it may be beneficial to protect the refractory from corrosion by adjusting the slag composition so that the solubility of the refractory material is minimized. Figure 10 shows the quaternary system CaO-MgO-SiO_2-Al_2O_3. Considering high corrosive conditions, magnesia-containing refractory materials are used frequently. Furthermore, a slag mixture located in the periclase precipitation area can improve the lifetimes of the refractories.

The chemical composition of slags determines their liquidus temperature, but it also influences the oxide activities, their viscosity, their electric conductivity, etc.

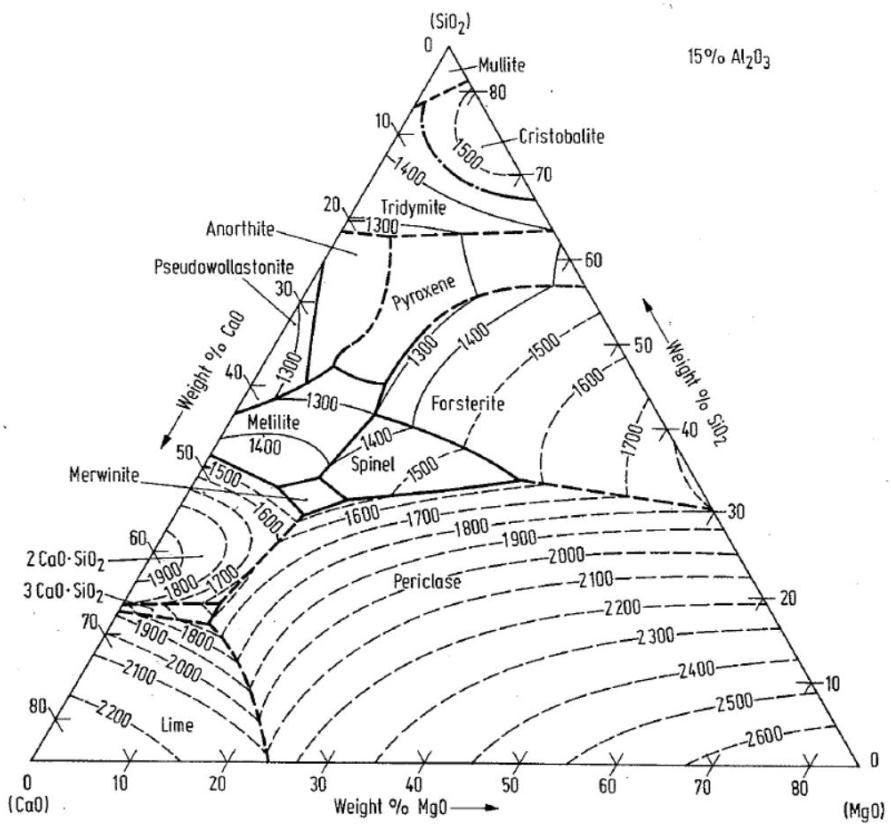

Figure 10: Illustration of the quaternary system CaO-MgO-SiO_2-Al_2O_3

3.3 Oxide Activity

Generally, the use of concentrations in equations from physical chemistry is only valid for solutions that behave analogous to ideal gases. Real solutions have to deal with complex interactions, which is why the concept of an effective concentration – the activity – has been developed. Considering slags, some oxides show significant deviation from ideal behavior. If the chromium oxide's activity in Equation 3.1 exceeds its concentration, the thermodynamic equilibrium shifts to the product. Recovery processes can make use of this if the chromium oxide's activity can be increased. Interactions between different chemical compounds cause

the deviation between ideal and real behavior. In other words, the oxides' activities are determined by a slag's composition. [24–26]

Various authors have studied the influencing factors on chromium oxide's activity [27]. Generally, the slag's basicity constitutes an important factor. Xiao et al. examined the CaO-SiO_2-CrO_x system at a temperature of 1,600 °C [28]. They measured the electromotive force by the use of an oxygen probe. The exact experimental setup can be seen in the referring literature [24]. The measured voltage was then used to calculate the chromium oxide's activity. Figure 11 summarizes the results of the experimental data. Considering the chromium concentration of the slag, the data was split into four groups. For all groups, the activity coefficient increases with an increasing CaO to SiO_2 ratio. This correlation was also found by other authors [6,29]. Therefore, recovery rates of chromium may be increased by increasing a slag's basicity B_2.

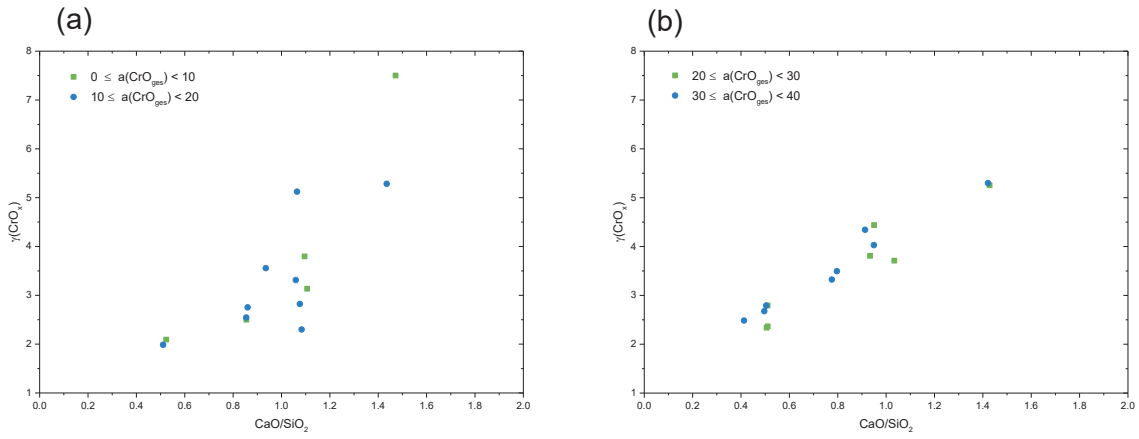

Figure 11: Influence of the CaO/SiO_2 ratio on the activity coefficient for chromium oxide in the CaO-SiO_2-CrO_x system [28]

Generally, lower basicity leads to the inclusion of metal cations such as chromium in the silicate networks, which can be described as a more stable dissolution in the slag. In contrast, increasing basicity breaks these networks and releases the metal cations.

3.4 Viscosity

Viscosity is the resistance of a fluid flow. If a liquid has low viscosity, it exhibits high flowability and vice versa. Considering a smelting reduction treatment of a slag, the viscosity influences the separation speed between the slag and the metal phase. Furthermore, it has a correlation with the diffusion rate of ions [30,31]. Therefore, it affects the kinetics of the whole recovery process, which is why it represents an essential element. A slag's viscosity is determined by its temperature and chemical composition. Since a direct measurement is a costly task, mathematical models have been developed. However, models only provide accurate values in

a specific area of composition. Kekkonen et al. give a good overview of the available literature and describe different viscosity models and their principles [32].

Figure 12 and 6 illustrate the temperature's influence on a slag's viscosity. The used slag compositions come from Table 2, which can be found in Chapter 4.3. The values were calculated using five different models:

- Urbain [33]
- Riboud [34]
- Iida [34]
- Iida^{modified} [35]
- NPL [36]

Employing Ubrain's model results – compared to the other methods – in higher values for the viscosity for the given slag systems. Depending on the exact composition, the other models give comparable data. Figure 12a displays a slag system with a CaO to SiO_2 ratio of 1.2. While the result from Iida^{modified} is slightly lower, Riboud, Iida and NPL yield similar viscosities, although all three models use a different approach in their mathematical model. As an example, the temperature dependence is modeled as follows [37]:

- by the Weymann-Frenkel equation for Reboud,
- by the Arrhenius equation for NPL,
- and by a so-called "quasi-structural approach" considering the slag's network parameters and basicity index for Iida [37].

In Figure 12b and c Iida, Iida^{modified} and Riboud give a slightly lower viscosity than the NPL method. The temperatures' influence is similar for all models. However, with increasing temperature, the gap between Urbain and the other models decreases. Figure 13 shows another illustration of the same data. The viscosity is outlined in respect to the slags' basicity B_2. All models illustrate an increasing flowability with increasing basicity for the given slag systems. This decrease is in good agreement with the network-forming character of SiO_2 and the network-destroying character of CaO and the theory that large molecule networks increase the resistance to flow. Compared to the others, the NPL model predicts a lower influence of the basicity. This can be seen in Figure 13. The gap between the different models decreases with increasing temperature. [32]

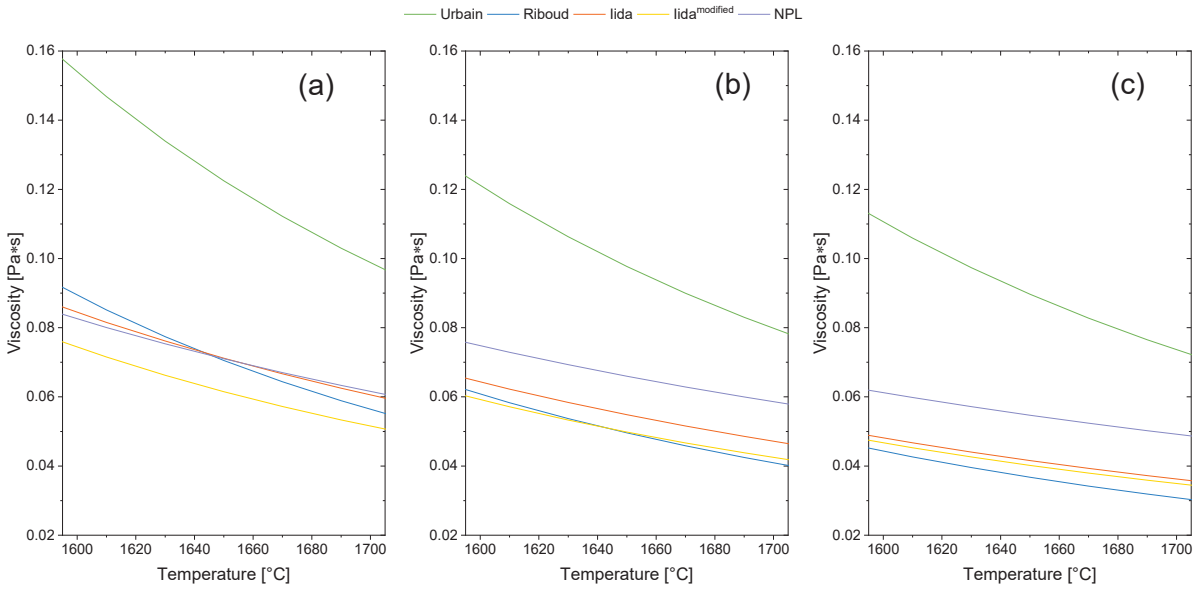

Figure 12: Applying different viscosity models as a function of the temperature for three slag systems. Slag compositions were used from Table 2 (a) EAF 1 (b) EAF 2 and (c) AOD 1

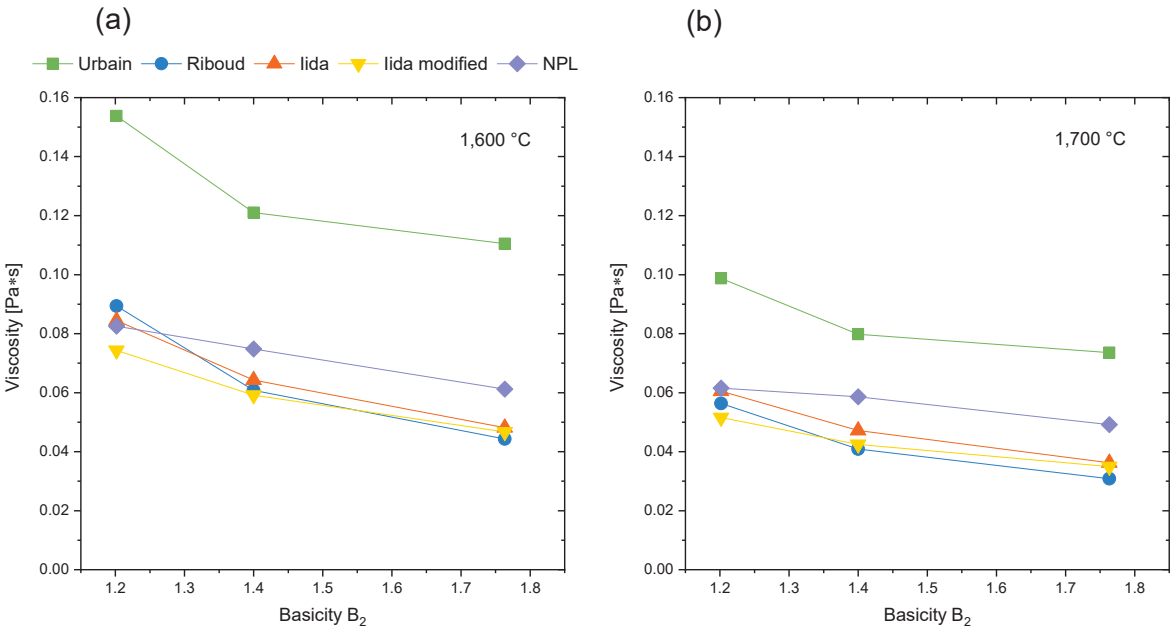

Figure 13: Calculated viscosities for different slag systems and different viscosity models. Compositions for EAF 1, EAF 2 and AOD 1 from Table 2 were used. (a) 1,600 °C and (b) 1,700 °C

The comparison between the different approaches shows that the different models include some divergences; especially, the Urbain model calculates a significantly higher viscosity. So, the viscosity has to be known exactly and measurement is mandatory. However, all models reveal the same tendencies regarding temperature and composition. This is why any model can be used to estimate how the viscosity will be influenced when either the slag composition or the temperature is adjusted.

3.5 Reduction agent

The metallurgical industry uses various reduction agents, but carbon is still the most commonly used one. However, gases such as hydrogen or less noble metals such as aluminum, silicon, calcium, etc. can also be applied. The Richardson-Ellingham diagram in Figure 14 illustrates the temperature dependence on the stability of oxidic compounds and shows the reduction potential of carbon, carbon monoxide and hydrogen. The diagram is usually drawn assuming 1 mol oxygen and an oxide activity of 1 at a pressure of 1 bar. It gives a rough overview of possible reducing agents and required temperatures.

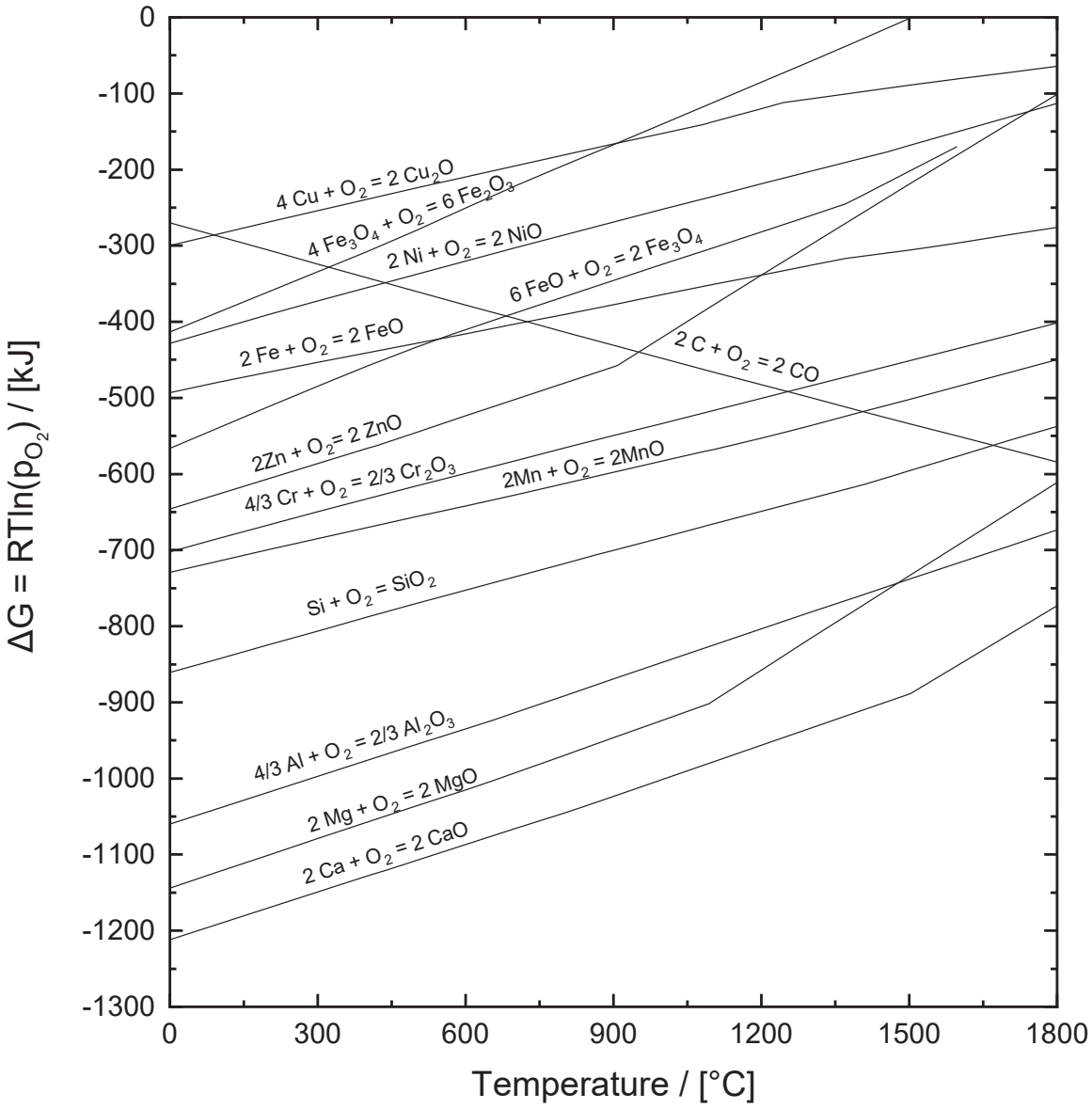

Figure 14: Richardson-Ellingham diagram for various reactions [21]

Thermodynamically, chromium can be reduced by manganese, silicon, aluminum, etc. as well as carbon at a minimum temperature of 1,100 °C. When assuming carbon monoxide and

hydrogen, besides the temperature, the ratio between CO to CO_2 and H_2 to H_2O determines the reduction potential. Considering a pyrometallurgical process that uses carbon as a reduction agent, Equations 3.2 and 3.3 show the reduction of chromium oxide. If hydrogen or water is present, the reaction can also run as depicted in Equations 3.4 and 3.5.

$$CO_2 + C \rightarrow 2CO \quad 3.2$$

$$3CO + Cr_2O_3 \rightarrow 3CO_2 + 2Cr \quad 3.3$$

$$H_2O + C \rightarrow H_2 + CO \quad 3.4$$

$$3H_2 + Cr_2O_3 \rightarrow 3H_2O + 2Cr \quad 3.5$$

These reactions' thermodynamic equilibria are described in Figure 15. The calculations assume an excess of carbon, which is a typical situation in metallurgical furnaces. The data shows that hydrogen reaches a higher reduction potential than carbon monoxide, in particular in the lower temperature range, because the water-gas shift reaction produces a higher ratio between hydrogen and water here. This can be seen in Figure 15c.

The illustrated data indicates that the reduction of chromium oxide requires a temperature of approximately 1,400 °C to 1,500 °C in order to shift the chemical equilibrium to a theoretical recovery rate of almost 100 %.

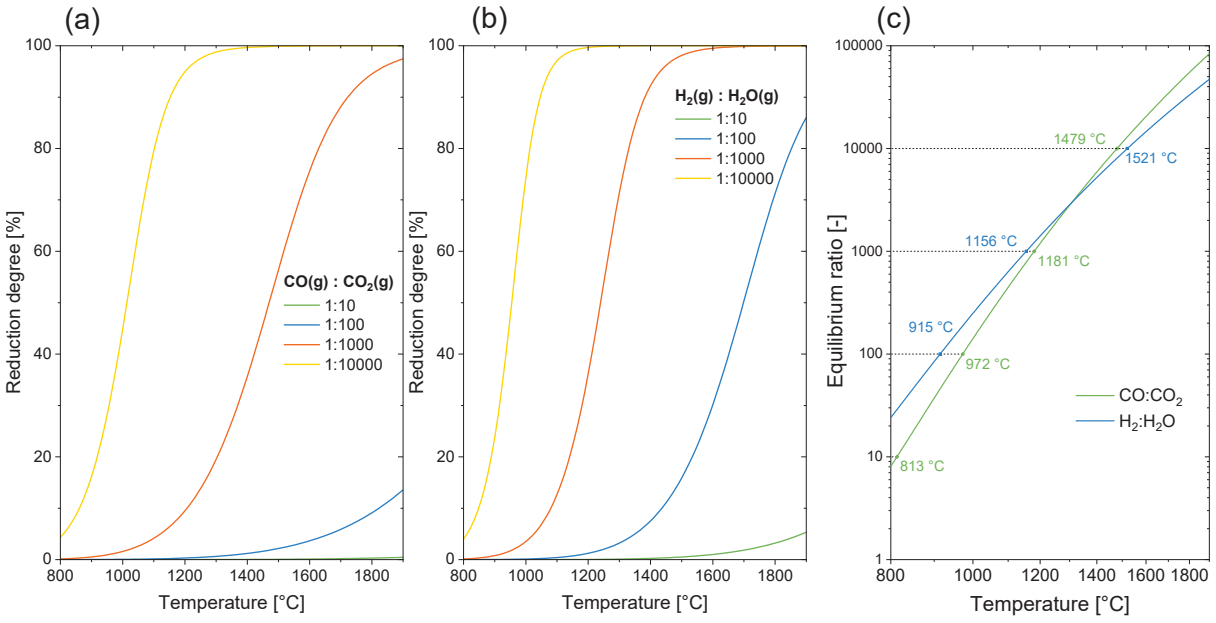

Figure 15: Thermodynamic equilibrium of the chromium oxide's reduction for (a) carbon monoxide, (b) hydrogen and (c) equilibrium of the gas composition when excess carbon is present

Equations 3.6 to 3.10 explain the metallothermic reduction reactions between chromium, manganese, silicon and aluminum.

$$Cr_2O_3 + 3\,Mn \rightarrow 2\,\mathrm{Cr} + 3MnO \quad (3.6)$$

$$Cr_2O_3 + 1.5\,Si \rightarrow 2\,\mathrm{Cr} + 1.5\,SiO_2 \quad (3.7)$$

$$Cr_2O_3 + 2\,Al \rightarrow 2\,\mathrm{Cr} + Al_2O_3 \quad (3.8)$$

$$MnO + 0.5\,Si \rightarrow \mathrm{Mn} + 0.5\,SiO_2 \quad (3.9)$$

$$3MnO + 2Al \rightarrow 3\mathrm{Mn} + Al_2O_3 \quad (3.10)$$

Considering a stoichiometric mixture between the reactants from Equations 3.6 to 3.10, the thermodynamic equilibrium can be calculated using the “Equilibrium Compositions” module from HSC Chemistry 8 [21]. Figure 16a displays the resulting ratios of chromium to manganese, chromium to silicon and chromium to aluminum. Figure 16b is the corresponding plot regarding manganese. Generally, the thermodynamic reduction potential decreases heavily with increasing temperature. For example, the reduction of chromium oxide with a stoichiometric amount of silicon results in an equilibrium ratio of 10^9 for chromium to silicon at 500 °C. This ratio decreases to 10^3 at 1,700 °C. Nonetheless, assuming a sufficient amount of silicon or aluminum as a reduction agent for chromium will de facto reduce all of the chromium oxide. Looking at the manganese oxide reduction, the ratio of manganese to silicon falls below 20 at 1,700 °C. Consequently, a full recovery of manganese is more difficult.

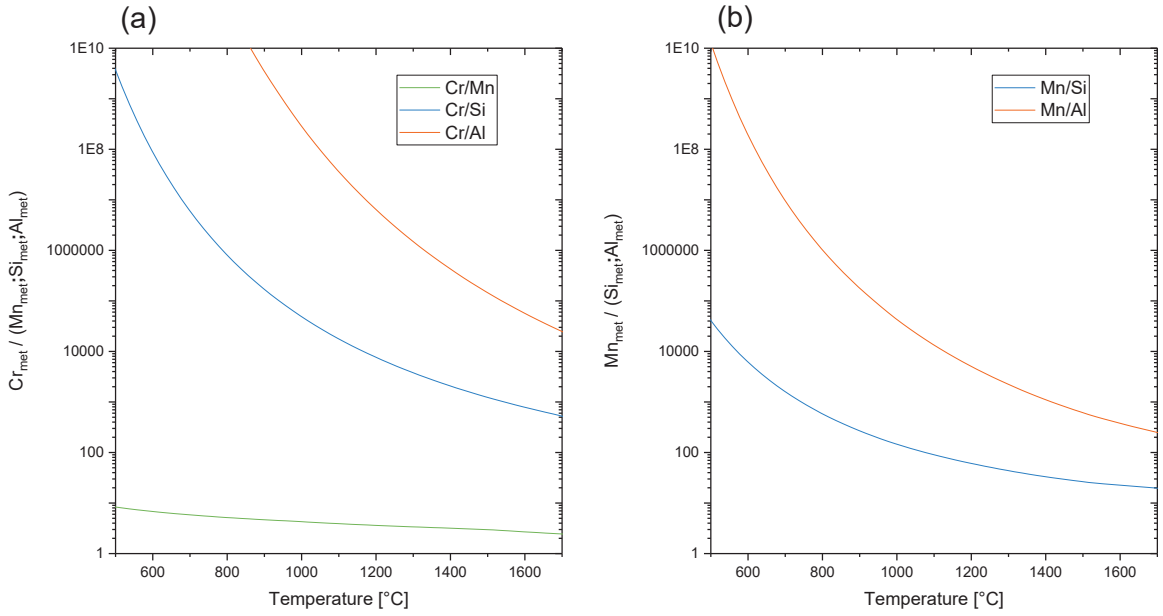

Figure 16: Calculated equilibrium between chromium, manganese, silicon and aluminum using HSC Chemistry 8 [21]

The visualization of thermodynamic data shows the relationship between the achievable recovery rates for chromium oxide in respect to the reduction agent and temperature. When

carbon is present, both carbon monoxide and hydrogen may be involved in the reduction reaction and will be regenerated by the Boudouard or water gas reaction. In order to achieve high recovery rates within this reaction mechanism, high temperatures are required. In contrast, using metals such as silicon or aluminum as a reduction agent may work independently from the temperature. However, this thermodynamic study does not include any kinetic aspects, which usually depend heavily on the temperature. More details about reaction kinetics can be found in Chapter 6.1.

4 Characterization of the Processibility

The estimation of the usability for waste materials requires a characterization of their processibility. The present work focuses on a slag and a dust fraction from the steel plant as well as a mill scale and a grinding residue fraction from the rolling mill. The characterization includes a chemical analysis for all materials. This was done by scanning electron microscopy in combination with an energy dispersive X-ray spectroscopy. A mapping was recorded for the slag, mill scale and grinding residue in order to get basic information on the chemical compounds. This information can be used to calculate the amount of reduction agent for the reduction of oxidic compounds to metals. Additionally, it visualizes if a mechanical recovery by physical separation can be considered.

After the chemical characterization, each residue was treated in a reductive melting using an induction furnace. The concentration course during the experiments was recorded with slag samples that were taken at defined time intervals. Each trial included six to eight. Furthermore, the samples were analyzed in the hot stage microscope in order to obtain information about the evolution of the melting behavior.

4.1 Experimental Setup

The experimental setup of the reductive melting was similar for all experiments, so it is only described once within this chapter. A tiltable induction furnace with a maximum power input of 80 kW was used. The energy input in an induction furnace is reached by the generation of eddy currents. For this reason, an electric conductive material must be present. Generally, oxidic materials like slag and dust exhibit insufficient conductivity, which is why they cannot be heated directly. However, a practical solution is the use of a conductive crucible. The focus of the present thesis lies on the investigation of the carbothermic reduction reactions. Therefore, the use of a graphite crucible represents an acceptable solution, because it does not excessively influence the running reactions. Figure 17 shows a picture of the furnace in the melting lab. The graphite crucible was placed in the opening for the induction field. The crucibles used have an outer diameter of 250 mm, an overall height of 300 mm and a wall thickness of 30 mm.

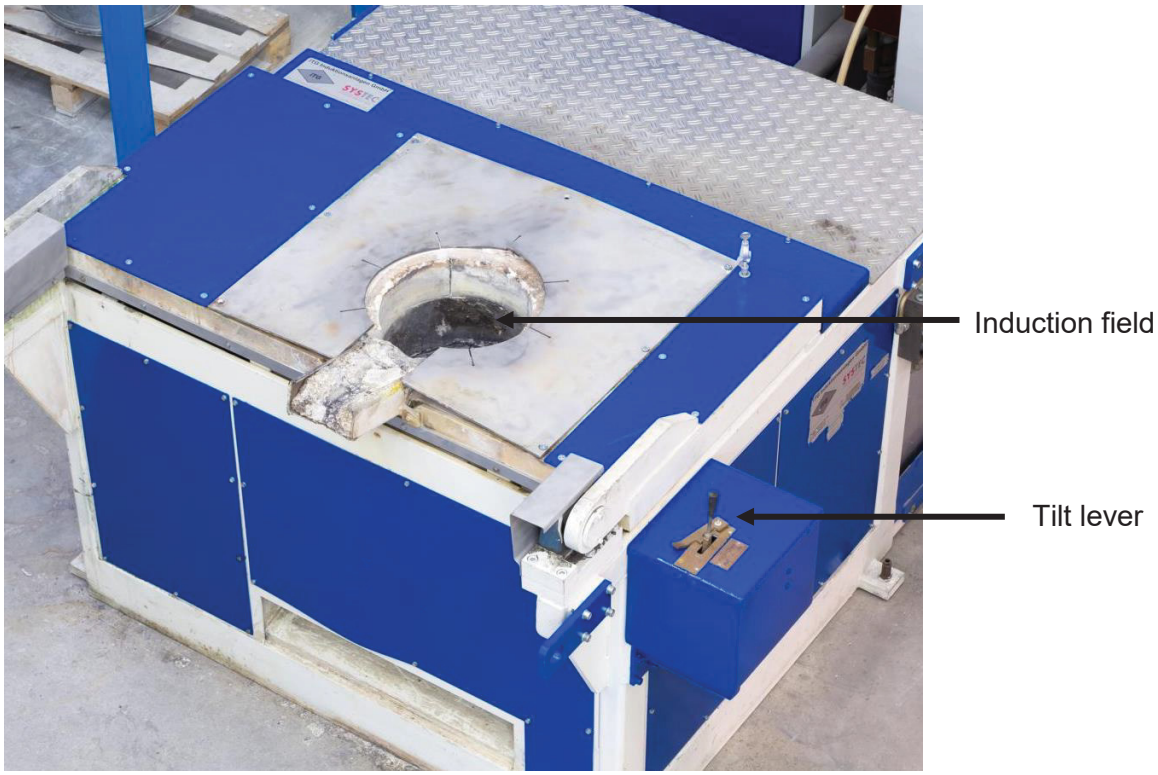

Figure 17: The induction that was used for the pyrometallurgical experiments

Each trial started with a preheating step in order to obtain a temperature of 1,700 °C in the graphite crucible. The energy input was set to a maximum of 40 kW, because higher values can damage the crucible. After the target temperature was reached, a holding period of 15 minutes was applied in order to compensate temperature variations within the crucible.
Then the material mixture was put into the furnace. The materials' melting took approximately 15 minutes for all experiments. After the majority of the furnace's content was liquid, the first sample was taken. The sampling was done with an iron rod that was dipped into the melt in order to allow the slag to freeze onto the rod. The first sampling was defined as the starting time of the process, although some prereduction cannot be excluded during the heating and melting. Since the furnace temperature and the amount of fed material were similar for all experiments, the influence of this prereduction is assumed to be small. After each trial, the samples taken were ground in a vibration mill and analyzed with a SEM-EDX.

4.2 Comparison of SEM-EDX and ICP-MS

In order to prove the accuracy of the EDX analysis, some samples were analyzed additionally by ICP-MS. Figure 18 summarizes the results for calcium, chromium and manganese. The comparison shows that both methods result in similar values. Since the Chair for Nonferrous

Metallurgy owns a scanning electron microscope equipped with an EDX detector, it was used to perform all further analyses.

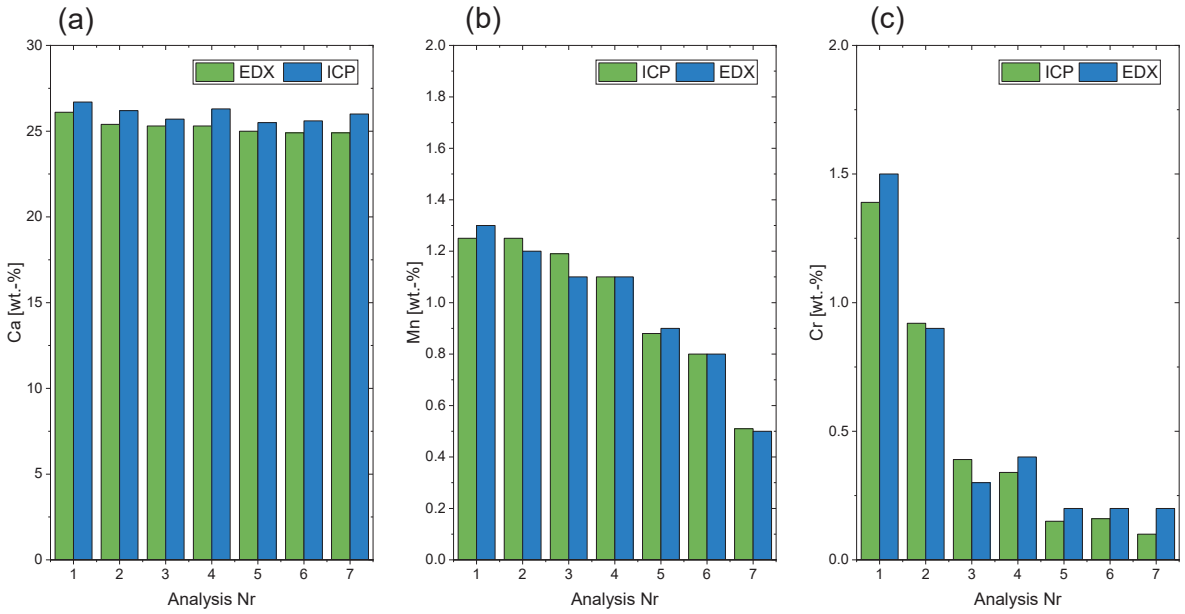

Figure 18: Comparison between ICP and EDX analyses for (a) calcium (b) manganese and (c) chromium

4.3 Slag

Figure 19 shows a picture of the EAF slag tested. It has a fine grain size and its visual appearance can be described as dust-like. The fine grain size originates from the disintegration which occurs during the cooling of slags that have a high basicity. The fraction of disintegrated material depends on the cooling rate. Figure 19 also shows the presence of some lumpy pieces. However, chemical analyses indicate no significant differences between the lumpy and fine-grain-sized fraction.

Figure 19: Disintegrated EAF slag that contains a minor number of lumpy pieces

Table 2 gives exemplary compositions for AOD and EAF slags from the stainless steel production. The slag builders' concentrations have some variations. This can be explained by the wide range of alloying concepts for stainless steel grades requiring different slag properties. AOD slags show a slightly higher lime concentration compared to EAF slags. Nevertheless, their overall composition is similar. The slag tested is – compared to the slags found in literature – higher in alumina and magnesia; the reducible compounds' concentrations are similar.

Figure 20 shows a mapping from the scanning electron microscope. The carbon measured originates from the sample preparation. It shows that quartz and calcium are finely distributed. In contrast, magnesia and iron are mainly present in larger particles. Alumina is present in both larger and finer particles. The same can be said for chromium and manganese. Calcium, silicon, aluminum and magnesium are present in oxidic form only. Chromium and manganese can be found as oxides and metals. In contrast, iron seems to only occur as a metal. Generally, the valuable elements iron, chromium and manganese are more likely to be found in larger particles.

Table 2: Compositions of EAF and AOD slags from stainless steel production

	CaO	SiO_2	Al_2O_3	MgO	FeO	MnO	Cr_2O_3
EAF 1 [38]	41.7%	34.7%	6.3%	9.1%	0.5%	2.1%	3.5%
EAF 2 [39]	46.9%	33.5%	2.3%	6.2%	2.0%	2.6%	3.2%
EAF 3 [40]	45.5%	32.2%	3.7%	5.2%	3.3%	2.0%	3.3%
EAF 4 [40]	38.8%	14.1%	6.7%	3.9%	5.6%	5.0%	2.7%
AOD 1 [41]	55.9%	31.7%	1.0%	3.0%	0.8%	1.9%	3.1%
AOD 2 [42]	47.2%	22.6%	6.6%	4.7%	4.6%	0.8%	2.3%
AOD 3 [39]	54.1%	26.5%	4.9%	6.3%	2.0%	1.0%	1.7%
Tested slag	38.1%	23.9%	13.2%	17.2%	1.2%	2.0%	4.1%

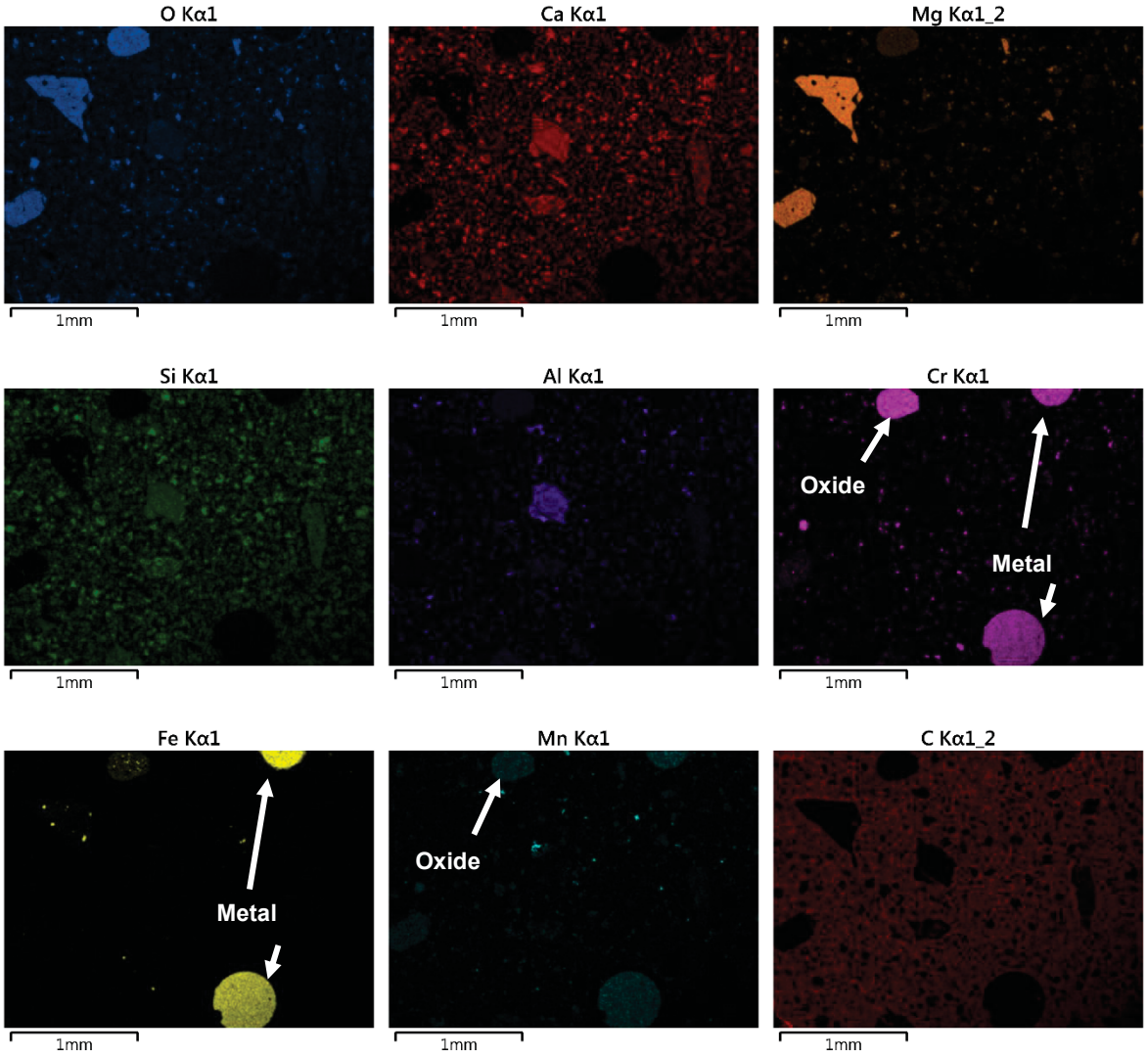

Figure 20: SEM-EDX mapping of a stainless steel EAF slag

The general experimental procedure is outlined in Chapter 4.1. After the preheating step, 3.5 kg of slag were inserted into the furnace. During the whole experiment, no dust was detectable. The melting took approximately 15 minutes, which was the time when the first sample was collected. This sampling procedure pointed out that some solids were still present. After 50 minutes, the furnace was tapped, which can be seen in Figure 21. During the tapping, the slag and an iron phase separated. The phases were then separated by hammer blows after cooling and the masses were determined. Finally, the slag samples were ground and analyzed. Figure 22a displays the concentration course for iron, chromium and manganese. The first sample has a chromium concentration of 2.8 % that decreases to 0.6 % after 46 minutes. A large percentage of the chromium is separated from the slag in a ferroalloy. The manganese concentration only decreases slightly. This is in good agreement with the thermodynamics that show that manganese is less noble compared to chromium and thus requires a higher temperature. The iron concentration is already low in the starting slag and close to the limit of determination for the first sample. It is not possible to describe its

concentration after the first sample. However, the iron concentration can be assumed as approaching zero.

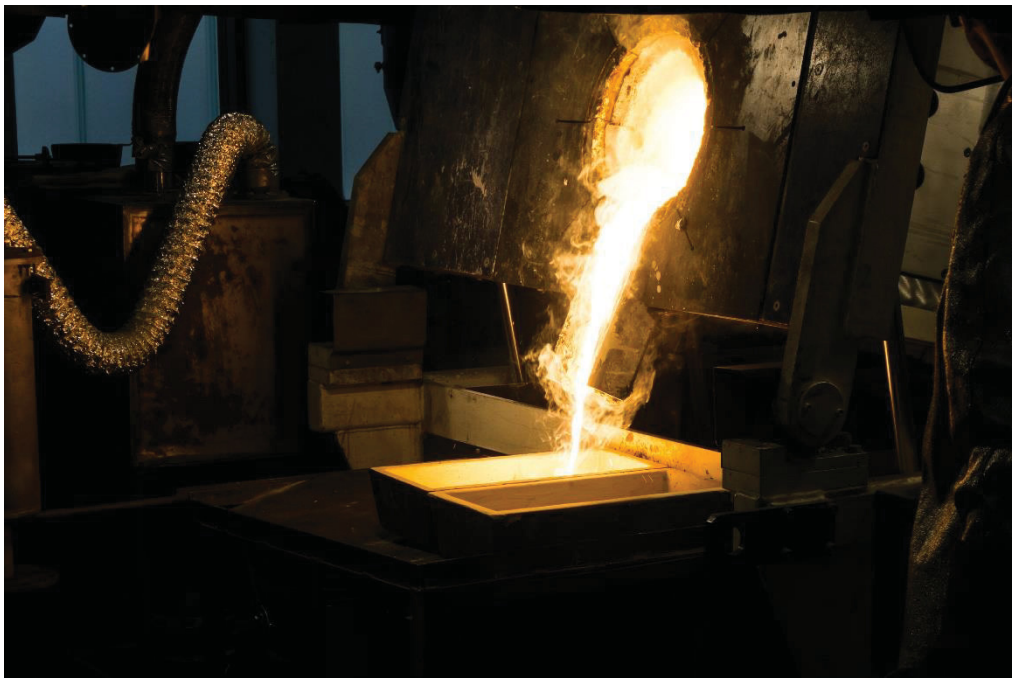

Figure 21: Tapping procedure after the pyrometallurgical treatment

The resulting mass flow is displayed in Figure 22b. It does not include the mass of carbon. Its measurement is not possible because it originates from the graphite crucible. Its amounts are small and can be calculated on a theoretical basis, which is why it does not influence the outcome of the mass balance. The processing of 3.5 kg slag results in 107 g of ferroalloy, 2978 g reduced slag and 104 g off-gas. In other words, the slag's carbothermic reduction treatment generates only 3.1 % of ferroalloy but 94.0 % of slag.

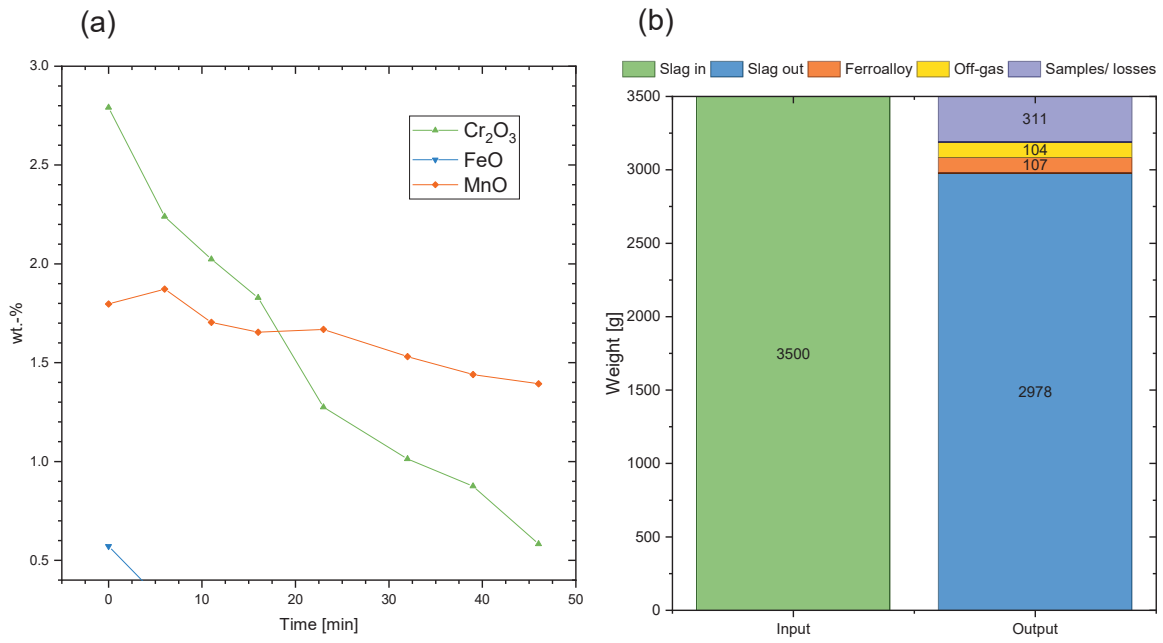

Figure 22: (a) Concentration course of iron, chromium and manganese and (b) visualization of the mass flow

In addition to the chemical analysis, all samples were investigated in the hot stage microscope. The results of these analyses are shown in Figure 23a and Figure 23b. Figure 23a displays the height of the sample and Figure 23b its form factor. The form factor describes if the shape of the sample has a circular form. It is defined as the ratio between the lengths of the circumference of the sample to the half-length of the circumference of the circle that has the same area as the sample (Equation 4.1).

$$Form\ factor = \frac{length\ of\ the\ circumference\ of\ the\ sample}{half - length\ of\ the\ circumference\ of\ the\ circle} \quad 4.1$$

The data from Figure 23 indicates a similar melting behavior for all slag samples. For that reason, it stays the same during the whole treatment. One possibility of defining the melting point is the temperature at which the specimen's height in the hot stage microscope drops below one third of the initial height. The melting points detected range from 1,426 C to 1,441 °C.

The form factors' evolution with increasing temperature shows a peak for all analyses. This peak indicates the so-called hemisphere temperature. It can be interpreted as the starting point of the melting process. If the information from Figure 23a and 16b is combined, it is observable that the heights of the specimens begin to decrease just after the hemisphere temperature is reached.

The analyses from the hot stage microscope demonstrate a consistent melting behavior during the whole treatment. The melting temperatures detected are significantly lower than the process temperature, which is why it can be assumed that the slag is fully liquefied.

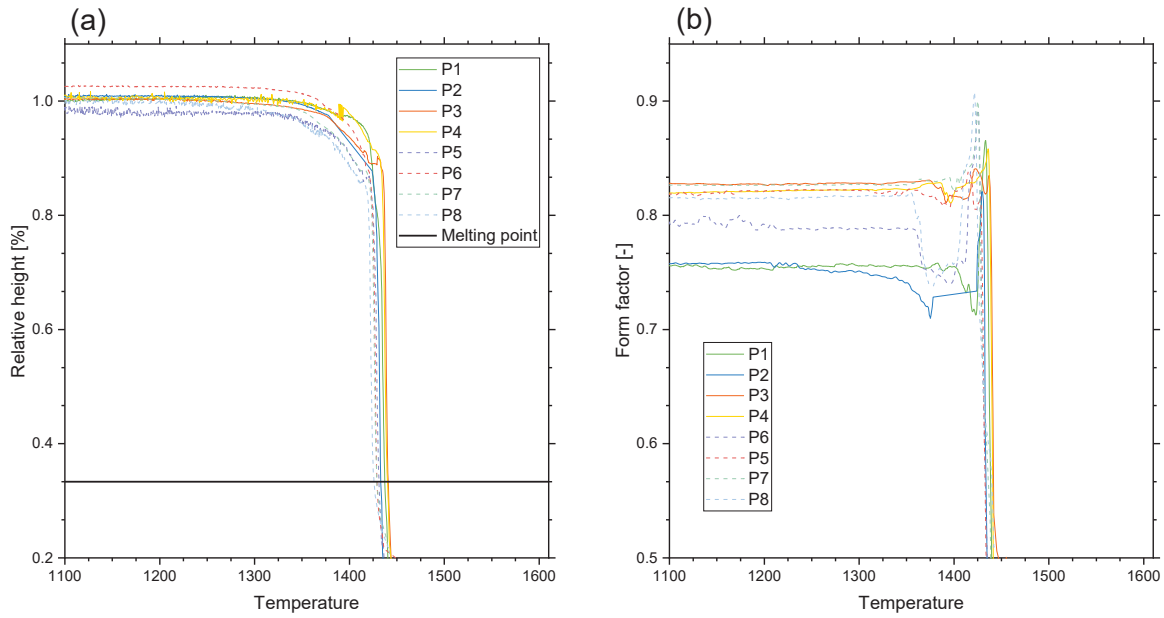

Figure 23: Results of the hot stage microscope analyses for the slag trial (a) relative sample height and (b) form factor of the specimen

4.4 Dust

The next residue that is characterized is an electric arc furnace dust fraction. A picture is visible in Figure 24. It can be described as a reddish, fine-grained material that has a tendency towards clogging. The color originates from the iron(III) oxide in the dust; the sticky behavior originates from the chlorides present in the dust.

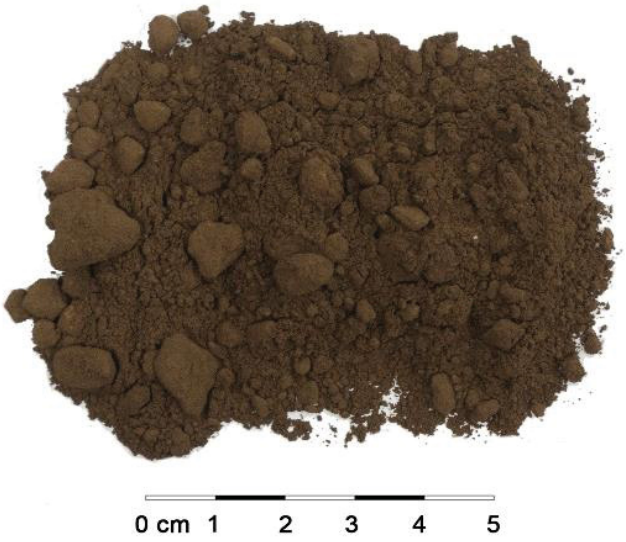

Figure 24: Electric arc furnace dust

Table 3 summarizes analyses of dusts from different stainless steel plants. Compared to the previously described slags, stainless steel dust mainly consists of reducible compounds. Considering iron oxide, manganese oxide, nickel oxide, zinc oxide, chromium oxide and lead oxide, the percentage ranges from 67 % up to 76.6 %. The slag tested contains significantly higher quantities of magnesia and zinc oxide. The magnesia's higher concentration can be explained by the higher magnesia concentration in the slag (compare with Table 2). The value for zinc oxide depends solely on the input material that is fed to the EAF. Especially scrap that originates from the automotive industry is known to contain coated zinc. The chromium oxide concentration of the tested dust is only one third compared to the level in the other dusts. All other substances have no important deviation.

Table 3: Exemplary compositions of stainless steel dusts

	CaO	**SiO_2**	**Al_2O_3**	**Fe_2O_3**	**MgO**	**MnO**	**Na_2O**	**NiO**	**ZnO**	**Cr_2O_3**	**PbO**
Dust 1 [3]	9.0	5.1	0.6	51.3	3.6	-	0.6	6.7	1.0	16.3	0.3
Dust 2 [43]	12.9	4.8	0.4	43.4	5.4	5.1	0.6	2.8	4.5	14.6	0.4
Dust 3 [44]	16.4	3.1	0.1	37.1	3.1	6.8	-	2.8	10.3	15.4	1.6
Dust 4 [45]	5.9	2.6	0.6	42.5	4.6	6.3	1.3	5.1	6.5	15.1	1.1
Dust 5 [46]	13.0	5.2	0.5	47.4	4.6	4.4	-	3.5	4.1	14.6	0.4
Dust 6 [47]	12.5	5.6	0.8	47.3	4.2	4.4	-	3.8	4.9	13.5	0.6
Tested dust	9.2	4.7	1.1	40.2	12.7	2.1	-	1.1	18.4	5.3	-

Figure 25 shows a mapping of the dust fraction's elemental distribution. Most of the elements are distributed in the form of extremely fine particles. However, some larger ones exist, with a

zinc ferrite particle on the bottom left. Generally, all elements are present as oxides. The fine grain size prevents a further evaluation.

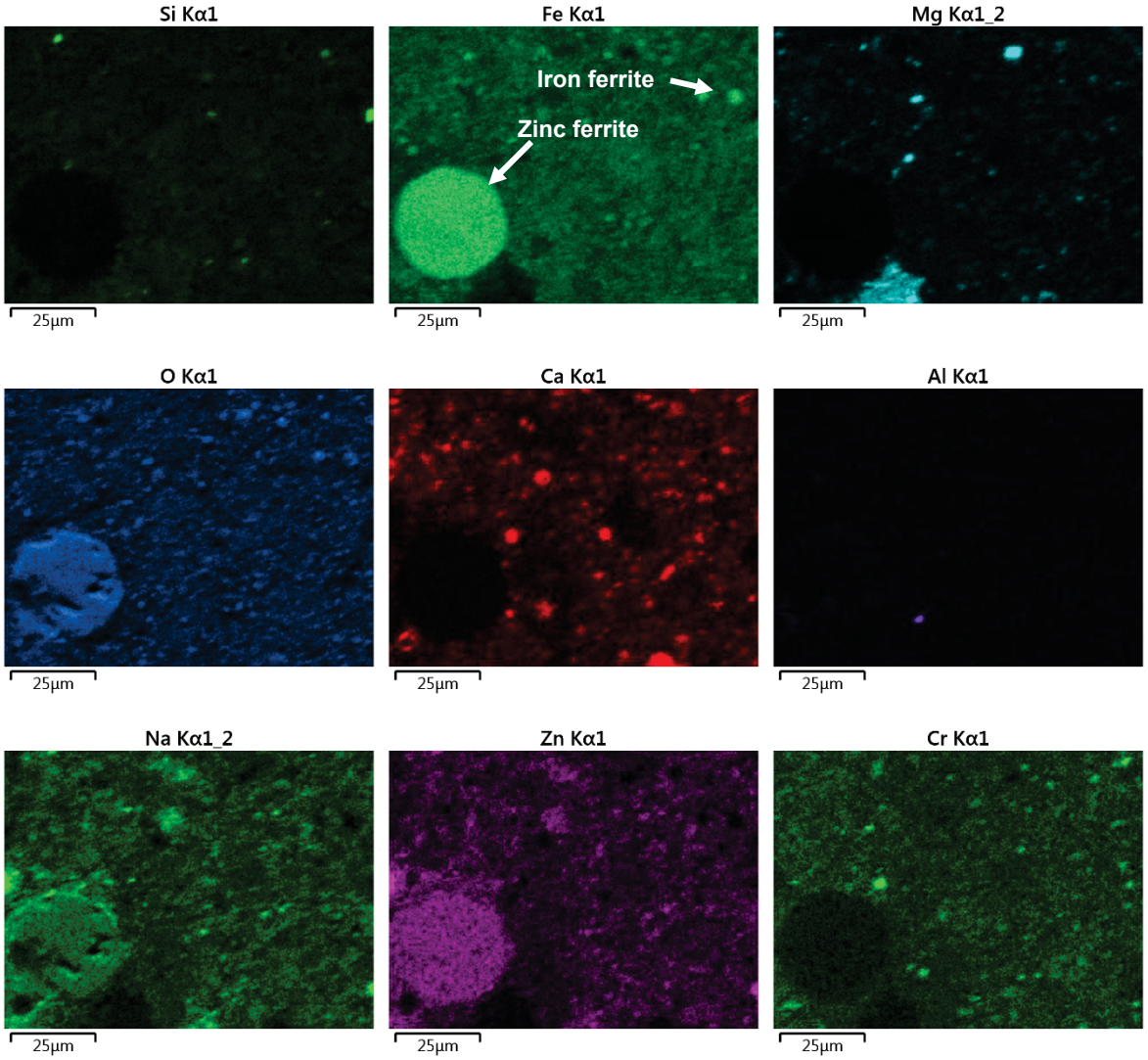

Figure 25: Elemental distribution mapping of the dust fraction

The reductive melting treatment was performed in the same manner as that with the slag. However, while the slag was fed solely, the dust was mixed with slag and quartz before charging it into the furnace. The reason lies in the relatively small concentration of slag building compounds that require a slag buffer. The input mixture consists of 3,000 g dust, 500 g slag and 250 g quartz. The ratio between the different materials was calculated to reach a basicity slightly higher than one.

After preheating, the material mixture was fed into the furnace. Just after it reached the hot crucible, the mixture began to react and the generation of white dust was observable. The dust tested contained 18.4 % of zinc in the form of zinc oxide and zinc ferrite. In the graphite crucible, the zinc compounds got reduced to their metal form, which evaporates at such temperatures. In the atmosphere, gaseous zinc metal is highly reactive and reoxidizes to zinc

oxide. This zinc oxide appears as the observable white dust. Furthermore, the re-oxidation can be seen as a bright white-colored flame in Figure 26.

Figure 26: Re-oxidation of gaseous zinc to zinc oxide

The described recovery of zinc includes two highly endothermic reactions – the reduction and evaporation. The volatilization of the zinc causes a temperature drop and can thus affect the kinetics of other compounds' reduction reaction.

The concentration course for iron, chromium and manganese can be seen in Figure 27a. While the iron concentration shows a steady decrease during the experiment, chromium and manganese have no clear trend, although the chromium concentration seems to decrease in the later stage of the process. Considering the Richardson-Ellingham diagram from Figure 14, iron is more stable than chromium and manganese. Consequently, it is the first compound that gets reduced from the slag. The slight increase in the chromium concentration during the first half of the trial can be explained by the decreasing slag amount. The same can be applied for the steady increase in the manganese's concentration. The decrease in the chromium concentration for the second sample may be caused by inhomogeneities in the slag. This matches with the detection of solid phases during the sampling of the first and second samples. In fact, chromium(III) oxide melts at 2,435 °C while manganese oxide melts – depending on the oxidation state – at a maximum of 1,945 °C. Additionally, the dissolution speed of the oxides in the liquid slag is different for manganese and chromium, which is why the shape of the course can differ. Finally, the concentration course suggests that elevated iron oxide concentrations inhibit the reduction of chromium oxide and manganese oxide.

Figure 27 shows the mass flow for the experiment. The first row of the legend describes the input materials; the second row the output materials. Some components are marked with an asterisk (*) that indicates a calculated value. These values are difficult to measure within

reasonable efforts. This relates to the coke, the produced dust fraction and the off-gas. Firstly, the coke originates from the graphite crucible used that also loses mass due to the reaction with oxygen from the surrounding atmosphere. Secondly, a precise measuring of the dust fraction requires a closed furnace and a special bag house filter. In any case, a closed furnace rules out sampling during the experiment. However, the amount of coke that is necessary for the reduction can be calculated, which leads to a value of 494 g. Considering the analyses of the fed dust and the resulting slag, the reductive treatment generates a calculated value of 580 g for the zinc-enriched dust. The value for the off-gas can be easily calculated with the amount of coke. Compared to the slag's investigation, this experiment generates much more ferroalloy and additionally, produces a zinc-enriched dust fraction. Consequently, the economic value of the generated materials is higher when processing dust compared to slag. For this reason, the use of dust in the feed material can increase the economic efficiency of the recovery process.

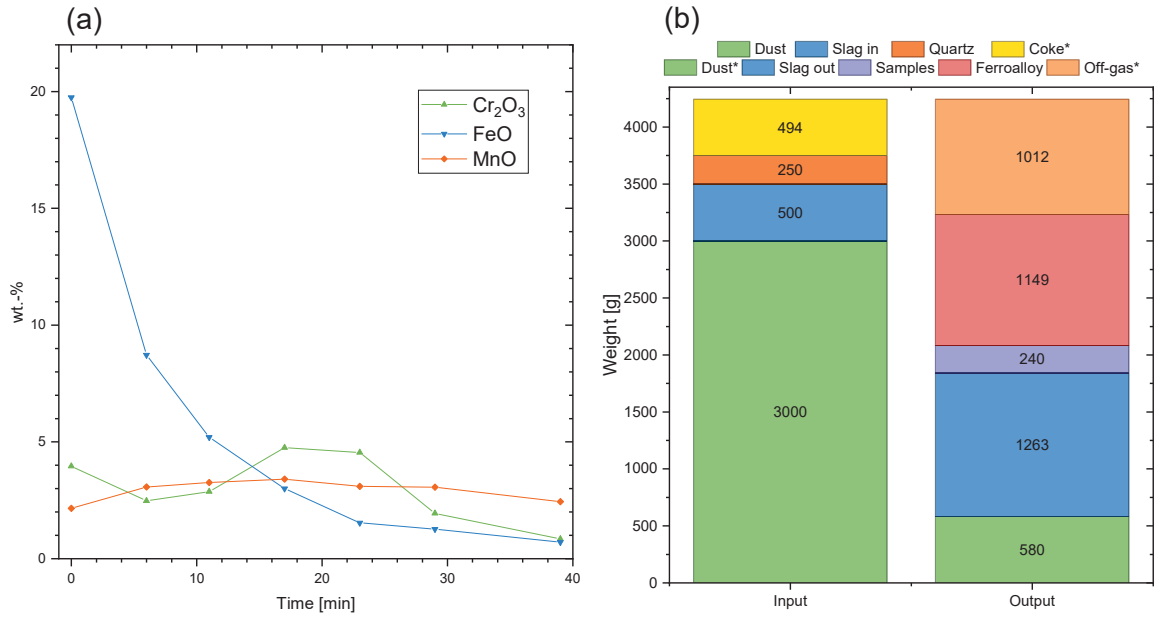

Figure 27: (a) Concentration course of iron, chromium and manganese and (b) visualization of the mass flow

The samples used for the chemical analysis were used once again for hot stage microscope analyses. The results can be seen in Figure 28. Compared to the first trial, the melting behavior of the slag changes during the experiment. The height of the first specimen never falls below the line that defines the melting point. However, steady shrinkage begins at approximately 1300 °C. A possible explanation lies in the occurrence of high melting phases which were not dissolved in the slag at the time when the sample was taken. Another explanation is metal inclusions or oxidized metal inclusions that form during the sampling. Therefore, the first trial was repeated in an inert atmosphere, but it resulted in a similar course. This is why the melting

behavior is assumed to be influenced negatively by high-melting mineral phases. An example of such a phase can be seen in zinc oxide. Interestingly, the melting point for the second and third samples is significantly lower than the following ones. This can be explained by the higher iron oxide concentration at this stage of the process. The melting point increases as the reactions progress and the iron concentration decreases. The last three samples result in almost similar values for the melting point. Compared to the first trial, the melting point of the resulting slag is lower. Figure 28b displays the progression of the specimens' form factors. All samples except the first one have a significant peak that indicates the detection of a hemisphere temperature. All hemisphere temperatures are the starting point where the specimens' heights begin to drop. Generally, the results from the hot stage microscope show that the input material mixture led to a slag system with a relatively good melting behavior, but relatively low melting temperature. Therefore, a lower amount of added quartz can be considered without negatively influencing the process's reactions.

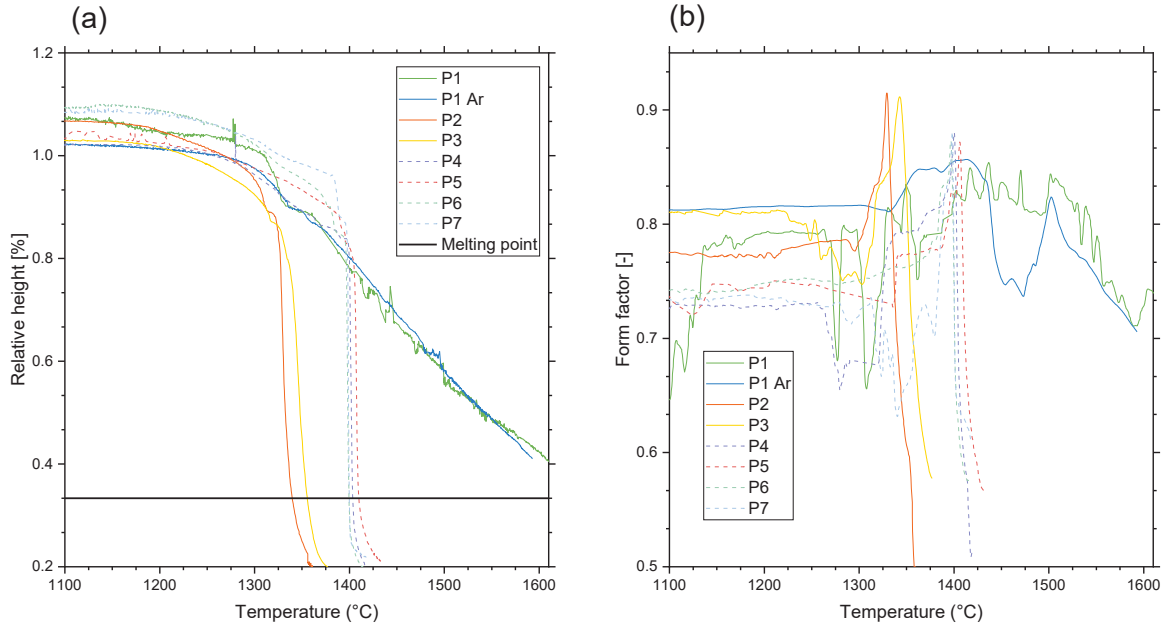

Figure 28: Results of the hot stage microscope analyses for the dust trial (a) relative sample height and (b) form factor of the specimen

4.5 Mill Scale

Mill scale represents the third residue characterized in detail in this chapter. It originates from the rolling mill. Iron ingots are heated up and due to the atmosphere's oxygen, an oxidation reaction takes place on the surface of the materials. Before and during the rolling process, the oxide layer is removed and separated from the steel. The mill scale of the more expensive steel grades gets separated individually and is recycled back to the EAF. However, the major part is collected together. This material stream has a varying and inhomogeneous composition,

which in combination with the narrow alloying concepts of the stainless steel industry prevents a direct recycling back into the EAF. A possible solution lies in the generation of a homogeneous ferroalloy that can be analyzed before it is fed into the EAF. A picture of the investigated mill scale can be seen in Figure 29.

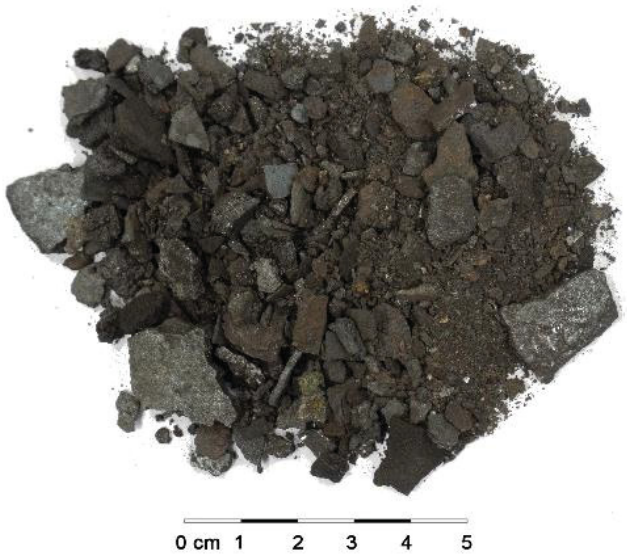

Figure 29: Mill scale

As described, the composition of mill scale follows the composition of the rolled steel grade. Additionally, it depends on whether a scale is collected individually for each steel grade or collectively. Finally, there is only little data on mill scale compositions available in literature. Accordingly, Table 4 contains the analyses of tested mill scale and only one example from literature. For both, the main components are iron oxide followed by chromium oxide and nickel oxide.

Table 4: Compositions of mill scale

	FeO	Cr_2O_3	NiO
Literature	76.0	16.4	4.5
Tested mill scale	81.5	8.2	1.6

Figure 30 shows a mapping that was obtained with the EDX of the SEM. Iron is found as sole iron in metal form as well as in oxidic form. Additionally, some ferrochromium particles exist. Chromium is only present as ferrochromium and chromium oxide. Interestingly, a particle just in the image's center has a sole chromium oxide layer and a ferrochromium core. Finally, the mapping shows that nickel is mainly present in metal form.

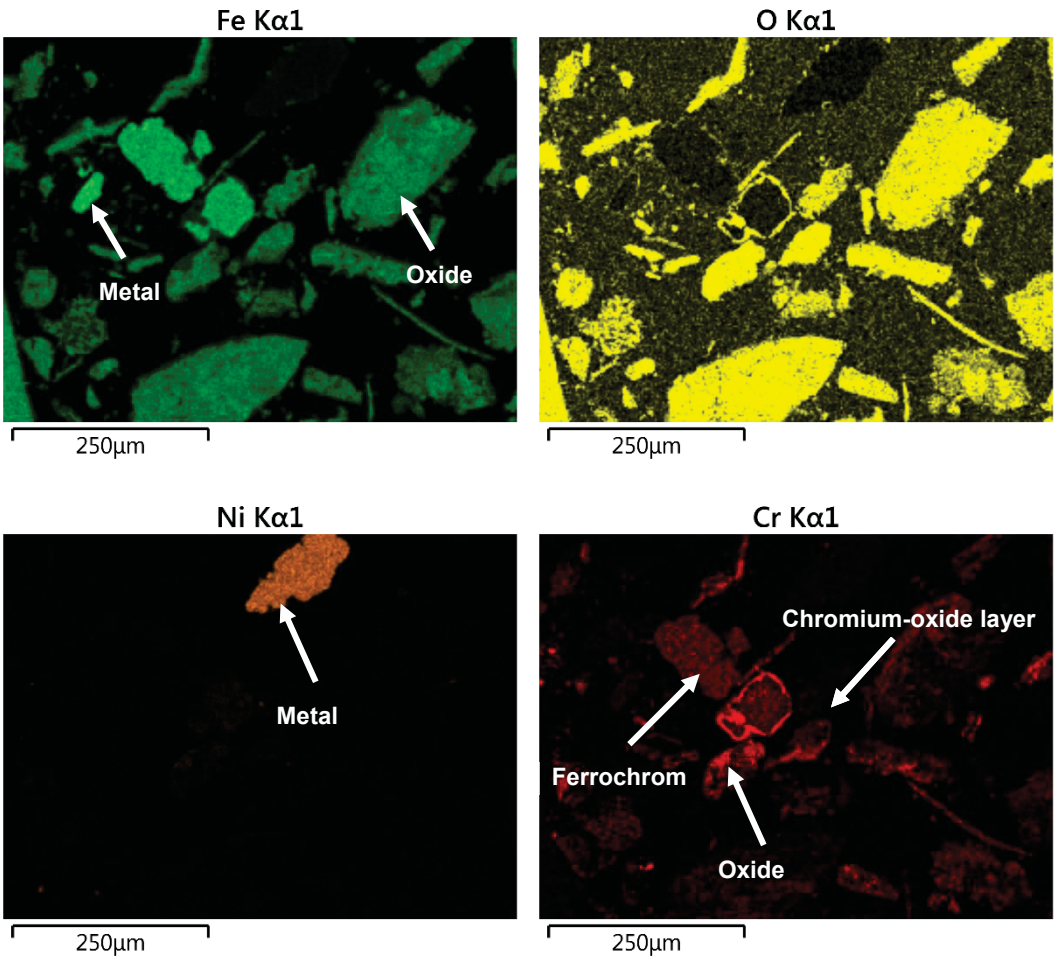

Figure 30: Scanning electron microscope mapping of a mill scale

Mill scale contains nearly no slag builders, because it consists predominantly of reducible compounds. The main component is iron oxide; the remaining composition depends on the rolled steel grade's alloying concept. Processing mill scale alone generates a slag that is high in iron oxide. Such a slag can dissolve other oxides rapidly and may therefore damage a furnace's refractory lining. Furthermore, the composition is not stable, which is why the resulting slag system is unpredictable, especially when most of the iron oxide is reduced. Therefore, a slag buffer has to be used when processing this material.

The reductive melting was performed in the same way as for the dust trial. The input mixture included 3,000 g mill scale and 500 g slag. Compared to the investigation of the stainless steel dust, no quartz was added, because no basic compounds were analyzed for the mill scale.

The first sample was taken 15 minutes after the material was fed into the furnace. As soon as the slag was fully liquefied, heavy slag foaming occurred. It required the removal of the fiber mat at the furnace's top, in order to prevent an overflow of the melt. The high reactivity of the slag can be explained by the high temperature in combination with the high iron oxide concentration. This leads to a high reaction rate and hence, causes an intense CO generation, which is the reason for the slag foaming.

Figure 31b shows the mass balance for the trial. As in Chapter 4.4, the materials marked with an asterisk refer to calculated values. The 606 g of coke were calculated considering the carbon that dissolves in the ferroalloy as well as the necessary carbon for the reduction of the oxides. The off-gas amount was calculated in consideration of the formation of carbon monoxide from the reduction agent. The weighed output materials were only 711 g slag and a majority of 2,215 g ferroalloy. Therefore, most of the mill scale was reduced to a ferroalloy. Mill scale can help to increase the amount of the ferroalloy in a recovery process.

Figure 31a displays the concentration course for iron, chromium and manganese. The iron concentration starts at 27 wt.-% and decreases during the treatment until it reaches 1.6 %. The chromium concentration increases steadily from the second to the seventh sample. This can be explained by the decrease in the slag amount due to the reduction of iron oxide that runs favored compared to the reduction of chromium oxide. However, the exact determination of the ongoing reactions is difficult because multiple reactions overlap:

- Reduction of iron oxide
- Reduction of chromium oxide
- Re-oxidation of chromium when it comes into contact with iron oxide
- Dissolution of chromium oxide into the slag

In contrast to the concentration course of chromium, the course for manganese looks steadier. It includes a small concentration increase from the first to the second sample, which may be caused by an inhomogeneous slag at the beginning. The later samples show a constant value.

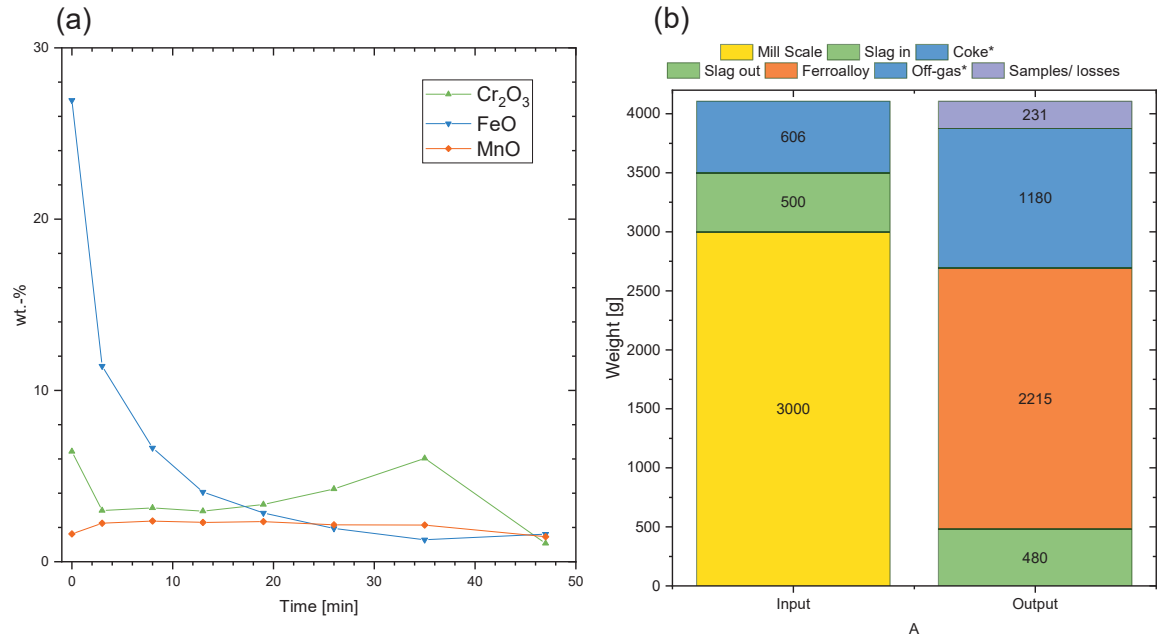

Figure 31: (a) Concentration course of iron, chromium and manganese and (b) visualization of the mass flow

The hot stage microscope analyses can be seen in Figure 32. Similar to the samples of the dust trial, the first sample's height decreases, but doesn't fall below one third of its initial value. The specimen may be stabilized by high-melting compounds such as chromium oxide. The second sample shows the lowest melting point, followed by a slight increase for the other samples. This behavior can be explained by the iron oxide concentration. Increasing values decrease the slag's melting point; hence, it behaves as a fluxing agent for the slag. The eighth sample melts at a significantly higher temperature. The reason may be found in the significant decrease in the chromium oxide concentration between the seventh and eighth samples. Since the freezing-point depression represents a colligative property, decreasing the chromium oxide concentration at low concentrations may increase the melting point, although it behaves differently at higher values. The second, fourth and eighth samples have a significant peak in their form factor. This characterizes a typical melting behavior of slags. The absence of such a peak for the sixth sample can be traced back to problems within the image analysis of the specimen. As a result, all samples except the first follow a typical melting behavior for slags. The melting characteristics of the first sample are comparable to the first sample of the dust trial. Its relative height doesn't fall below 33 % of its initial height and in addition, the form factor doesn't show a peak at all. After the analysis, a porous specimen that shrank but retained the same shape could be observed, stabilized by high-melting phases. This confirms the theory that some components of the input material mixture were not dissolved in the first part of the treatment. In order to examine the composition of the high melting phases, an SEM analysis was performed. However, the acquired data showed no significant difference compared to the analysis of the slag sample that was used to create the specimen prior to the hot stage analysis. The reason for this may lie in the surface tension of the liquid phase in connection with its cohesive and adhesive forces. They avoid the separation of the liquid from the solid phase as long as the specimen is stabilized due to a skeleton structure that only has small capillaries. Therefore, only a minority of the liquid phase infiltrates the alumina sample holder while the majority remains in the specimen; hence, the chemical analysis of the specimen does not change appreciably.

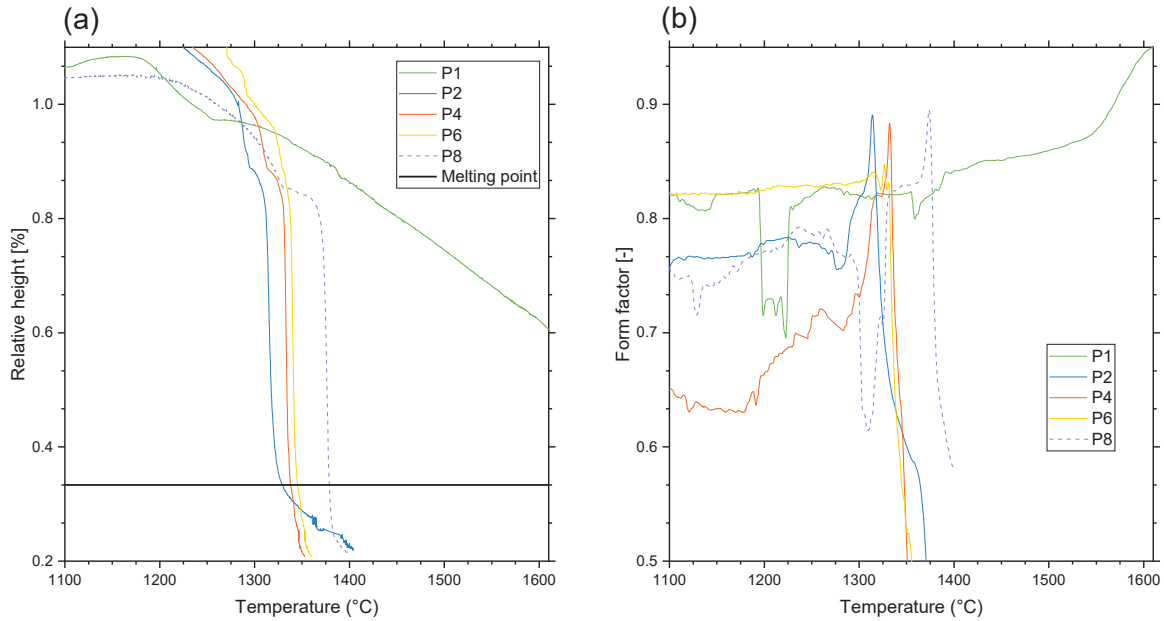

Figure 32: Results of the hot stage microscope analyses for the mill scale trial (a) relative sample height and (b) form factor of the specimen

4.6 Grinding residue

Finally, a grinding residue undergoes a detailed characterization. It originates from the grinding of billets and bars but occurs in smaller quantities compared to the previously described materials. Figure 33a shows a picture of the investigated residue. It contains a mixture of swarf and dust. Some bigger particles stick together and can hardly be broken apart.

Figure 33: Grinding residue

The preparation of a representative sample is difficult for the grinding residue. While the other materials were ground in the vibration mill, the metal needles in this material prevent this homogenization step. Therefore, the quantitative analysis in Table 5 cannot be seen as representative for the waste stream. Generally, the material's composition follows the processed steel grade's alloying concept.

Table 5: Analysis of the grinding residue

	FeO	Cr_2O_3	Ni
Tested grinding residue	54.7	17.0	21.6

A mapping of the elemental distribution is displayed in Figure 33. The concentration of the slag building compounds calcium, aluminum and silicon is very low. While calcium and silicon are distributed as fine particles, aluminum is found in larger ones. The list of valuable elements in the grinding residue is long. The mapping indicates the presence of iron, nickel, chromium, molybdenum, copper, manganese and vanadium. Additionally, traces of chlorine can be seen. Iron is present in metal and oxidic form. Nickel is mostly present in metal form; however, some small oxide particles are visible. Chromium is found as ferrochromium, in connection with nickel and as an oxide. The clearly visible molybdenum particle is a metal and it seems to be pure. The same can be said for copper. Generally, the mapping of the elemental distribution shows that the grinding residue contains many different elements in both metal and oxidic form. It is not possible to determine the exact ratio between metal and oxides. The mapping shows that the grinding residue includes many different valuable elements, some in the form of reducible oxides and some already as metal. For that reason, a direct recycling to the EAF is possible when the composition of the grinding residue is known. This requires individual separation for all alloying concepts. However, this represents a tremendous logistical effort, which is why it is usually collected together. Only expensive steel grades are separated individually. Consequently, the material usually has an inhomogeneous composition, which prevents its direct reuse in the EAF – similar to the description of the mill scale. This is why it is included in the present characterization.

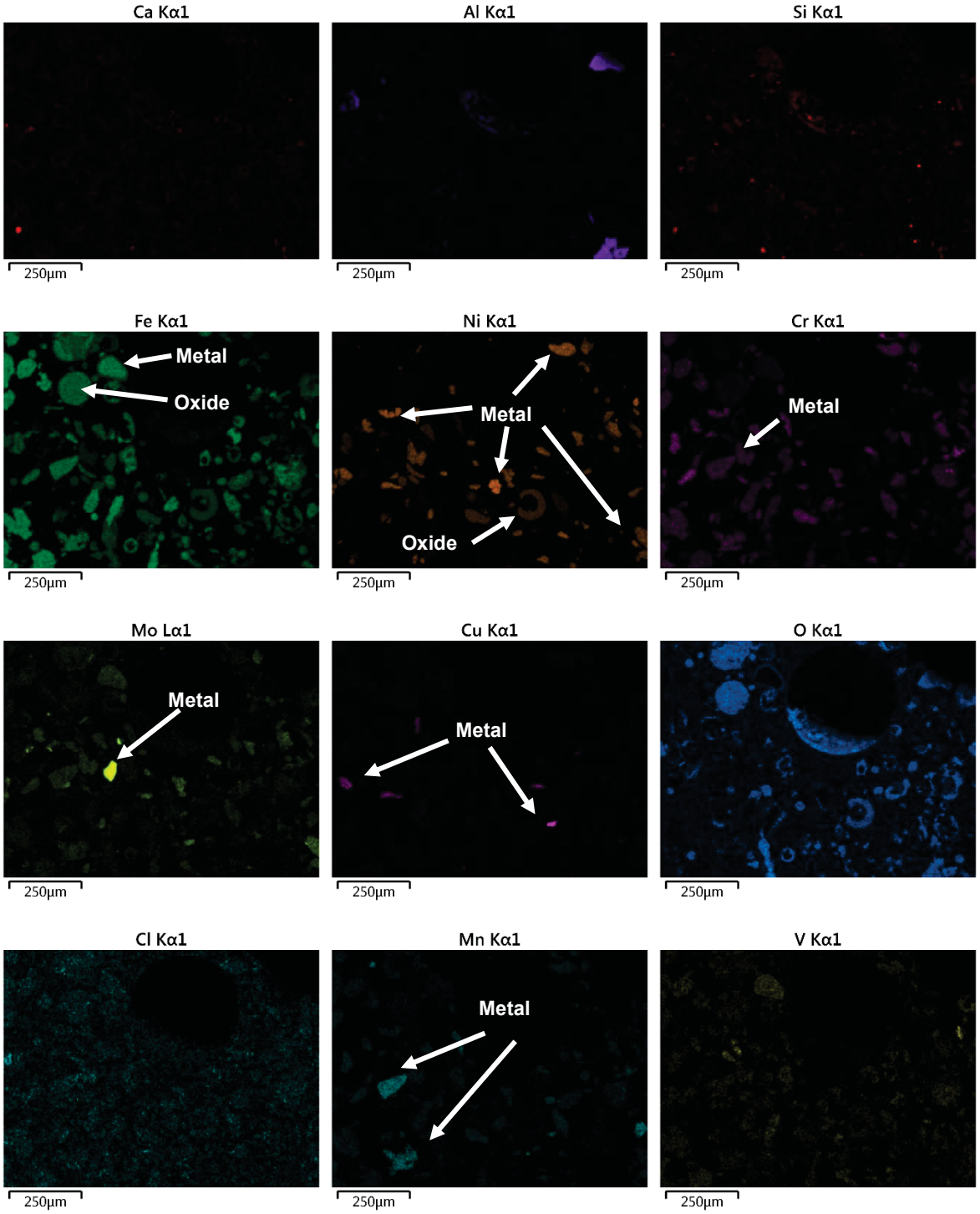

Figure 34: Mapping of the grinding residue

The reductive smelting trial was performed in a similar manner to the previous experiments. Figure 35 displays the input material mixture. It consists of 3,000 g grinding residue and 500 g slag. The experimental procedure was the same as described for the mill scale. The first sample was taken 17 minutes after the material was fed into the furnace. From the first to the fourth sample, solid phases as well as metal inclusions could be observed during the sampling. The metal inclusions can be identified visually, because re-oxidation caused by atmospheric

oxygen looks like a sparkler. Starting with the fifth sample, neither solid nor metal phases were detected. Figure 35 shows the concentration courses for iron, chromium and manganese. The first slag sample contained 17 % iron and 13 % chromium. While the iron concentration decreases from the beginning, the reduction of chromium starts with the fourth sample. The constant chromium concentration before can be explained by the preferred reduction of iron oxide. Additionally, a further dissolution of chromium-enriched phases may take place continuously. Comparing the chromium's time course with the mill scale investigation, it looks more comprehensive because it follows a consistent course. The manganese's concentration course shows a slight increase in the first half, followed by a noticeable decrease in the second half of the treatment. The manganese reduction does not start as long as increased iron and chromium concentrations are present. Therefore, its reduction is delayed to a later process stage.

Figure 35b summarizes the mass flow of the experiment. In addition to the mass of grinding residue and slag, coke has to be assigned to the input material. Its calculation is difficult because there is no information available about the exact carbon requirement. The output material stream includes 592 g slag and 2,349 g ferroalloy in the solid. Furthermore, the process generates a calculated amount of 1,196 g off-gas. Out of this, the grinding residue can be mixed with other residues in order to increase the outcome ratio of ferroalloy produced.

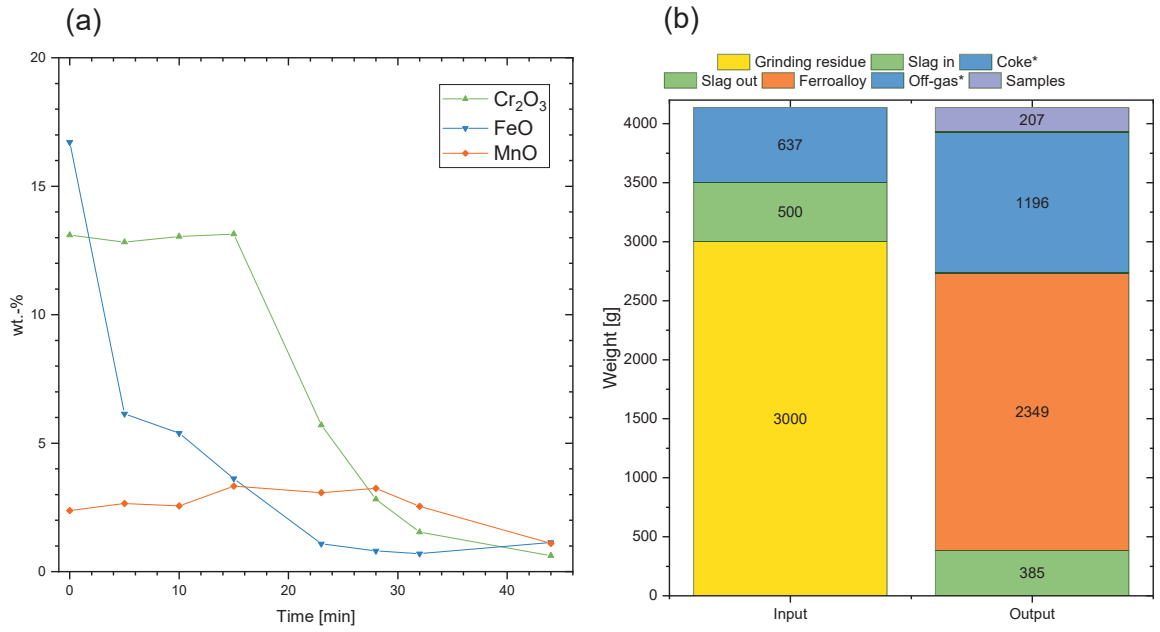

Figure 35: (a) Concentration course of iron, chromium and manganese and (b) visualization of the mass flow

Figure 36 shows the slag samples' results from the hot stage microscope analyses. The full melting of the input material seems to take longer for the grinding residue, because the curve for neither the first nor for the second or fourth sample falls below one third of their initial height

in Figure 36a. This is in good agreement with the observations during the experiment where solid phases were observed for the first four samples. Two possible explanations exist to describe the bad melting behavior of these slag samples. It could be caused by either undissolved high-melting oxides or the presence of high-melting metals. The grinding residue contains almost no slag-building compounds and a relatively high percentage of metal. Considering the smelting behavior of the mill scale, the grinding residue is assumed to follow a similar course if high-melting oxides are responsible. However, it takes much longer to achieve a typical melting behavior for the grinding residue. Therefore, metal phases may cause the slag's decreased fusibility. Nevertheless, high melting oxides cannot be completely rejected for the explanation. Figure 36b displays the form factor's course for the investigations. The first four slag samples contain no peaks, which is why a hemisphere temperature can not be specified for them. Starting with the fifth sample, hemisphere temperatures can be determined, which means that the melting behavior can be described as slag-typical. The hot stage microscope analyses show that the slag system of this trial can be improved in order to obtain a fully liquefied slag earlier. The addition of quartz is one possibility.

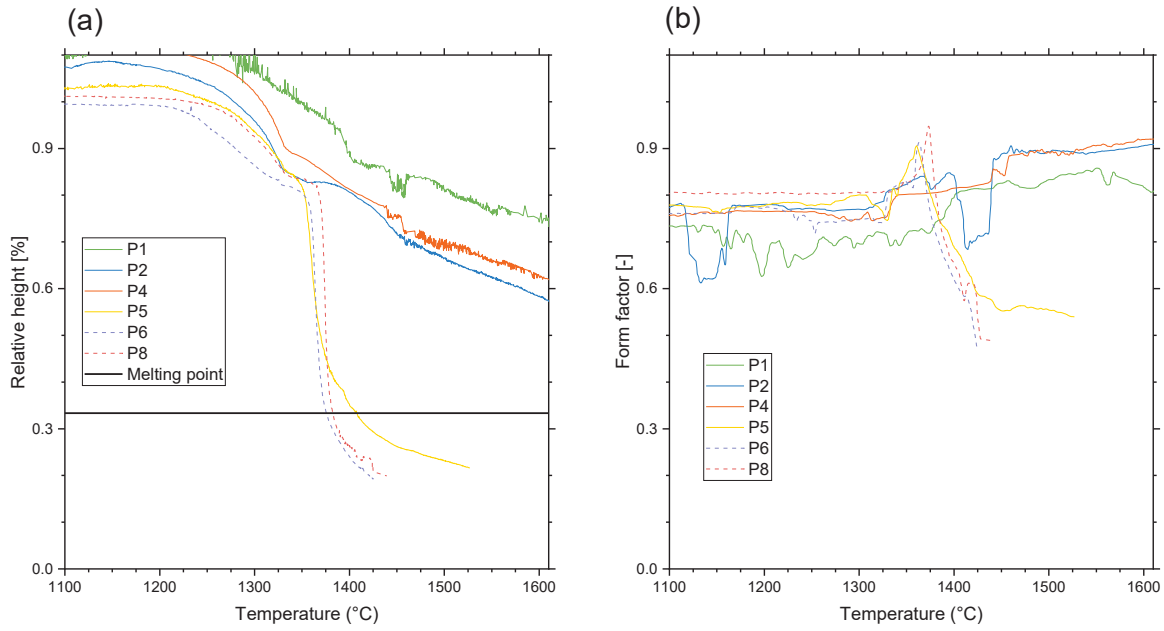

Figure 36: Results of the hot stage microscope analyses for the grinding residue trial (a) relative sample height and (b) form factor of the specimen

4.7 Summary

The characterization points out that slag, dust, mill scale and the grinding residue have different characteristics. Figure 37a displays the relative amount of produced ferroalloy for the different materials. The slag's melting treatment generated 107 g ferroalloy from 3,500 g starting material. Consequently, the specific amount of ferroalloy produced by slag can be calculated

through the division of 107 by 3,500, resulting in 3.1 %. Since the experiments that were performed with dust, mill scale and grinding residue included 500 g of slag, its contribution to the ferroalloy must be considered. Equation 4.2 describes the corresponding calculation.

$$\%ferroalloy = \frac{m_{ferroalloy,i} - \frac{107}{3500}500}{3000} \quad 4.2$$

Figure 37a shows that the relative amount of ferroalloy produced for the slag is very low when comparing it to the other materials. Processing dust transforms 37.8 % of the feed material into a ferroalloy. Furthermore, the recovery of dust generates a zinc-enriched dust. The ratio of produced ferroalloy is even higher for mill scale and the highest for the grinding, with values of 73.3 and 77.8 %, respectively. An important note relates to the fact that the amount of carbon is not considered in the feed material, but it is present in the ferroalloy. In addition, its high concentration prevented its quantification. Therefore, Figure 37a includes a minor error; however, the main outcome stays the same. Figure 37b displays the amount of slag produced in relation to the amount of input material.

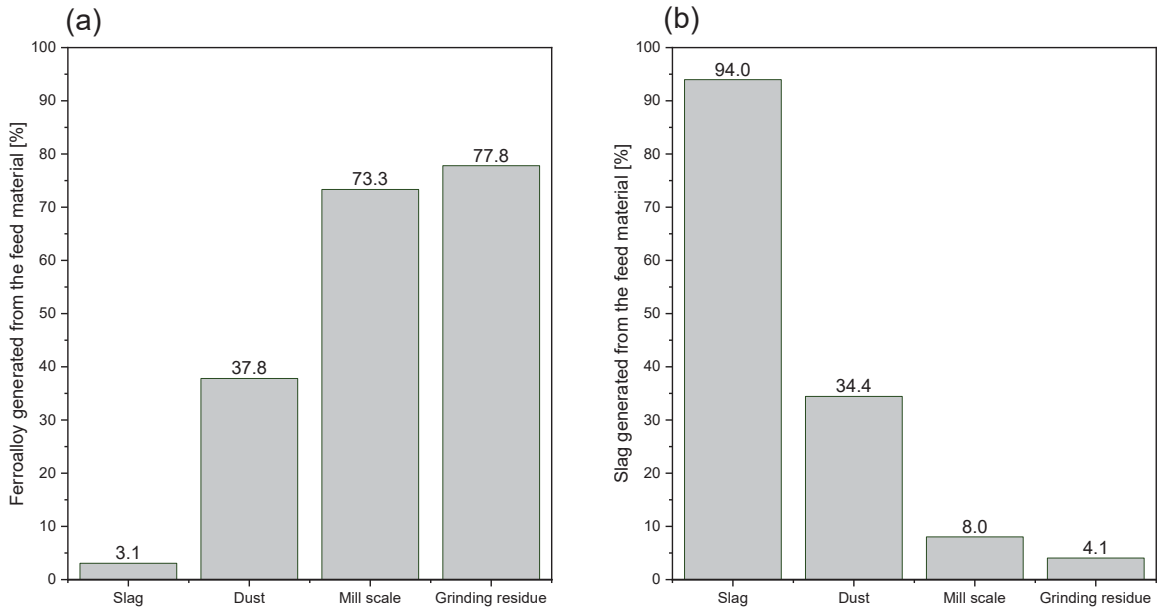

Figure 37: (a) Relative amount of generated ferroalloy and (b) relative amount of produced slag

Figure 38 summarizes the chemical analysis of the generated slags. The main slag building compounds are lime, magnesia, alumina and quartz. Figure 38a shows that all final slags consist mainly of these oxides. The slag trial resulted in the highest concentration for these compounds, because of the slag's low concentration of reducible compounds. In other words, the slag consists primarily of the slag builders. The other melting treatments led to more or less the same concentration of lime, quartz, magnesia and alumina in the final slag. Other compounds that were analyzed in the final slags are chromium, iron and manganese oxide.

The precise values can be found in the concentration courses above. Figure 38b displays the major compounds' ratios to have a better comparability between the final slags' properties. However, the difference between using the concentration and normalized concentration is small, as the dust, mill scale and grinding residue contain similar amounts. Finally, Figure 38c displays the calculated basicities B_4. The mill scale and grinding residue generate a more acidic slag compared to the dust. Figure 38c gives an overview of the basicity B_4 in the final slag phase for the different materials. It indicates that mill scale and the grinding residue can be used to decrease the basicity. Therefore, the basicity of the final slag can be adjusted by changing the mixing ratios of the input material to optimize its properties.

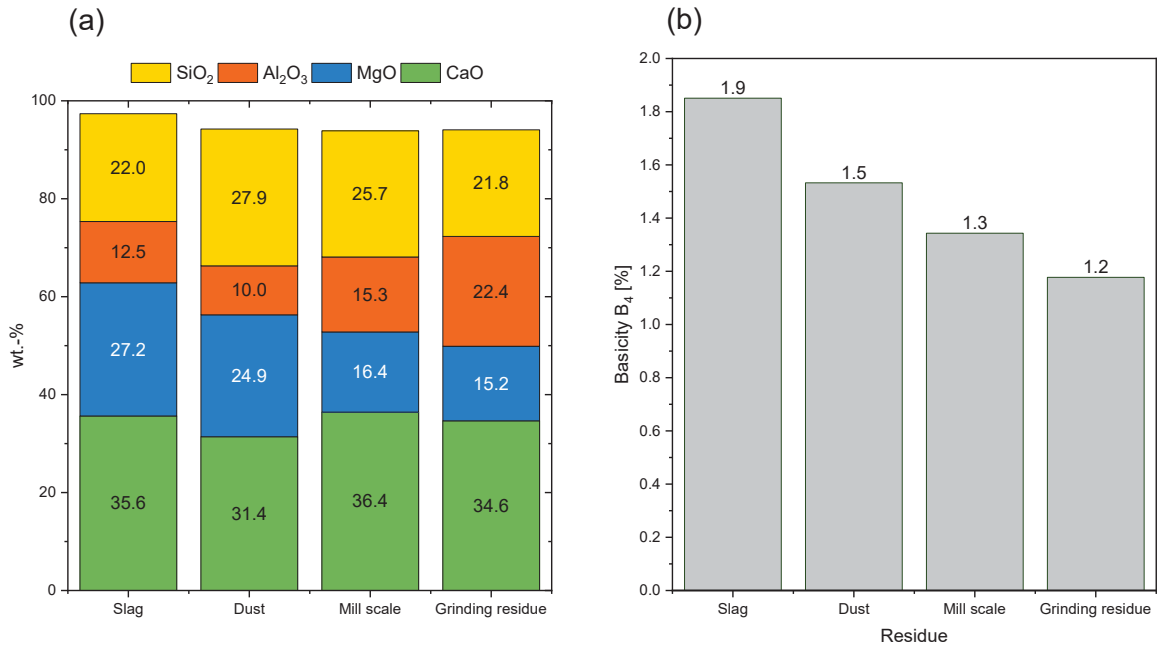

Figure 38: (a) Concentration of major slag compounds and (b) basicity B_4 of the final slag phase

The characterization showed that all investigated materials can be processed in a carbothermic smelting reduction treatment. The hot stage microscope analyses performed showed that the input mixtures used resulted in a slag phase with good melting properties during the whole treatment. However, when feeding grinding residue, an increase in the ratio of slag in the feed material can be considered. Generally, the method of hot stage microscope analysis can be described as a tool to optimize the slag system of a process in order to prevent high melting phases during the treatment.

5 Mass Balance Determination

After the characterization of the wastes, a smelting reduction test was performed in order to check if the expected theoretical mass balance matches the experimental data. The treatment requires a high temperature with a highly corrosive molten slag. In order to eliminate the refractory's and reduction agent's influence, the trial was performed in a graphite crucible that was heated by an induction furnace. The experimental setup was the same as that used in Chapter 4.1.

5.1 Experimental Setup

The first step of this chapter includes theoretical mass balance calculations. From these calculations, an input mixture was defined to produce a liquid slag without high melting phases. The experimental procedure was similar to the procedures in Chapter 4 with the addition of a bag house filter to capture the zinc-enriched dust fraction produced. Figure 39 illustrates the corresponding experimental setup. A fiber mat on top of the graphite crucible helped to reduce heat losses. In order to enable the post-combustion of zinc to zinc oxide, the condenser was placed with a spacing of 10 cm to the top of the crucible. This led to a certain suction of false air that supported the cooling of the condenser.

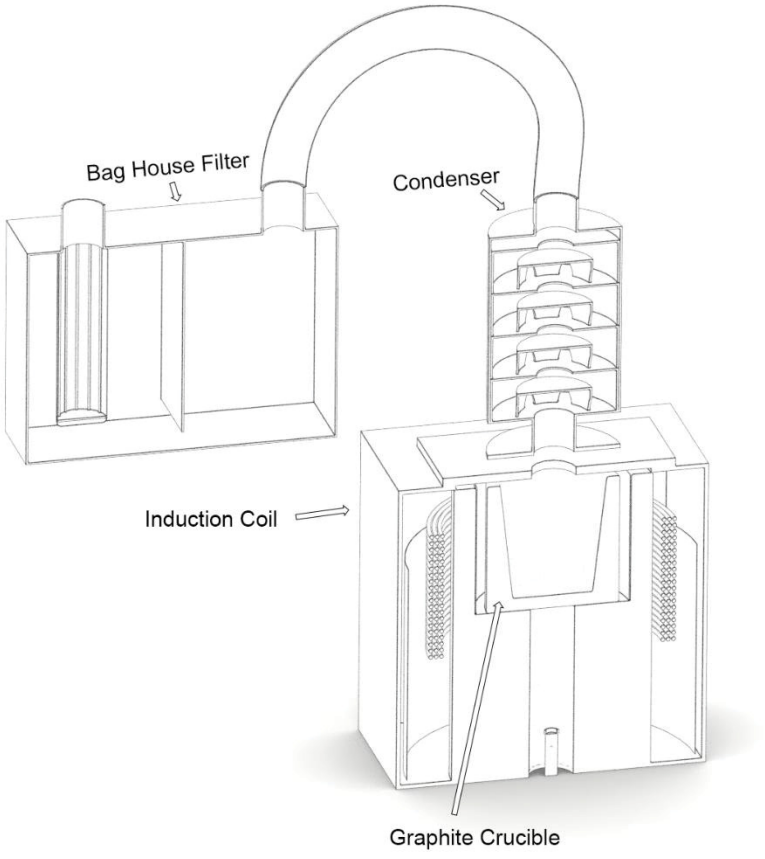

Figure 39: Experimental setup for smelting reduction trials to capture the zinc-enriched dust fraction

The first step of each trial was the preheating of the crucible. After the temperature reached 1,700 °C, the material's feeding into the furnace followed. The vaporization of zinc started instantly. The melting of the residues took approximately 15 minutes. The generation of zinc oxide was observed for the first 20 minutes. After 60 minutes, the power input was switched off. In order to achieve an exact mass balance, no tapping was performed. Instead, the cooling was done in the crucible. The slag and metal were separated by a hammer that crushed the slag into small pieces.

5.2 Test Description

Figure 40a shows the quantities of the input and output material streams. The generated carbon monoxide produced during the carbothermic reduction was not measured, which is why the input and output masses do not correlate. The fed wastes produce roughly 50 % slag, 32 % ferroalloy and 1.7 % zinc-enriched dust. The ferroalloy's chemical composition can be seen in Figure 40b. The major elements are iron, nickel and chromium. Additionally, carbon, molybdenum and minor concentrations of manganese, vanadium, tungsten, and copper were analyzed. Figure 40c shows the slag's composition. Its major compounds are lime, quartz, magnesia and alumina with minor quantities of chromite and manganese oxide. Considering the literature study from Chapter 2, the slag should be well-suited for the reduction of chromium oxide due to its high lime and magnesia content. Nevertheless, the final slag contains 2 % chromium oxide. This can be traced back to either a too short treatment time or a too low treatment temperature. A detailed study regarding the kinetics of the chromium reduction can be found in Chapter 7. The dust fraction was not analyzed, but the next chapter covers the characterization of the zinc-enriched dust fraction in detail.

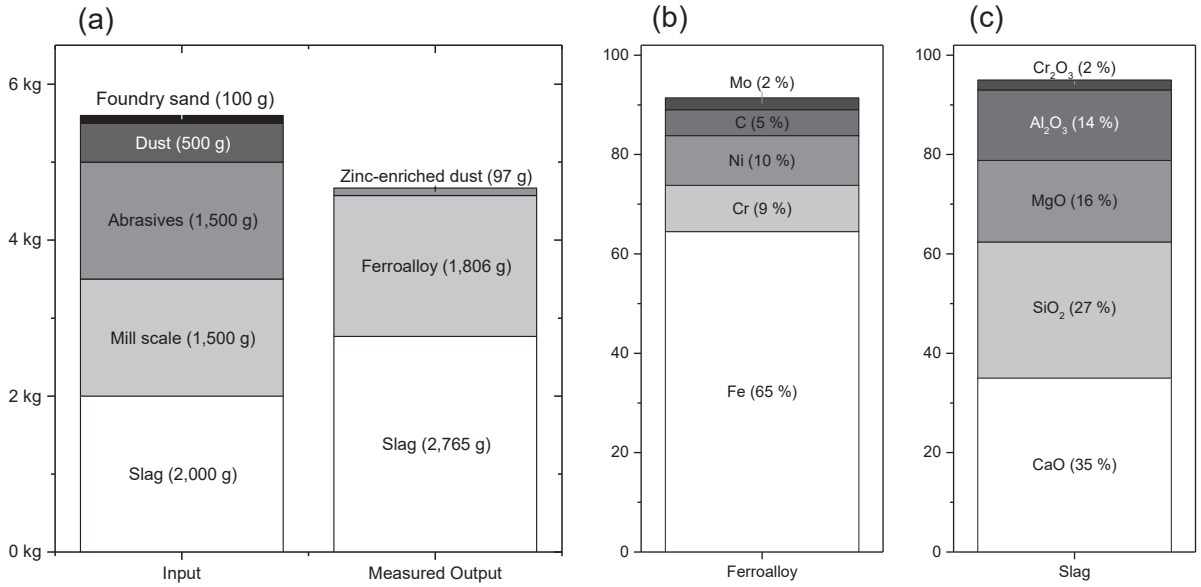

Figure 40: (a) Mass flow, (b) chemical analysis of the ferroalloy, (c) chemical analysis of the slag

5.3 Characterization of the Zinc-Enriched Dust Fraction

The characterization of the zinc-enriched dust includes three trials. The experimental setup was the same as that described in Chapter 4, but the input material mixture was adjusted. After the preheating step, 1 kg slag “A903” was fed into the furnace. The dust’s characterization showed improvable melting behavior, which led to the decision to use a slag that dissolves the high melting compounds. Afterwards, 3 kg of the dust fraction were brought into the molten slag. Additionally, 500 g quartz were used in order to adjust the basicity. Slag foaming occurred as soon as the dust began to melt. The intensity decreased over time and although it stopped after 45 to 50 minutes, the overall treatment time was 90 minutes per trial. The control of the temperature was difficult, because the process includes various reactions such as:

- Endothermic reduction of oxidic compounds like zinc oxide and chromium oxide
- Endothermic vaporization of volatile substances such as zinc
- Exothermic post-combustion of zinc to zinc oxide

All those reactions in the relatively small furnace led to an inhomogeneous temperature distribution. The high reaction rate of the zinc reduction and evaporation under the present conditions and the highly endothermic character caused noticeable freezing of the slag. Some measurements taken using a “Type S” thermal probe resulted in values between 1,525 °C and 1,650 °C, although they were performed in a short period of time. In order to get a qualitative statement regarding the reaction rate’s influence on the zinc-enriched dust fraction, the trials were performed with different power inputs. The chosen values were 30 kW, 40 kW and 45 kW, respectively. In order to get comparable results, all trials were performed on the same day; the second and third experiments started just after tapping the previous one.

5.4 Evaluation of the Different Material Streams

The analysis of the dust fraction was done by EDX. The sample homogenization was – compared to previous tests – more difficult, because grinding could not be performed in the vibration mill due to the dust’s sticky behavior. Figure 41 outlines the chemical composition of the dust fractions captured. The amount of zinc oxide generated increases with higher power input. A possible explanation is the slag foaming. It occurs due to the formation of gases within the slag, which is normally caused by the generation of carbon monoxide. The foam consists of little bubbles which burst as the carbon monoxide leaks. This bursting entrains small particles from the slag; in other words, it leads to a pollution of the zinc-enriched dust fraction. Higher power input results in an elevated slag temperature; hence, it increases the reaction rates. Consequently, more slag foaming occurs. This goes hand in hand with a more intense bubble bursting. Finally, the zinc-enriched dust fraction contains more impurities. However, the major dust fraction’s dominant impurity is the iron oxide, the concentration of which rises from

2 % to 10 %. A possible explanation is that the cracking step of zinc ferrite, its reduction and the volatilization of the zinc take place closely together. Nonetheless, this theory assumes that the major slag builders – lime and quartz – should also contaminate the dust fraction, but their concentrations are less than 1 %. Therefore, another theory relates to the condenser that is made out of steel. The hot, dust-loaded off-gas may cause corrosion. As a result of the higher power input, the off-gas temperature is also increased. This can result in more corrosion. Other impurities such as potassium, chlorine and sulfur remained at a constant level. Chromium, nickel, molybdenum, tungsten and vanadium were qualitatively detected in the EDX, but the concentrations were too low (< 0.5 %) for a quantitative analysis.

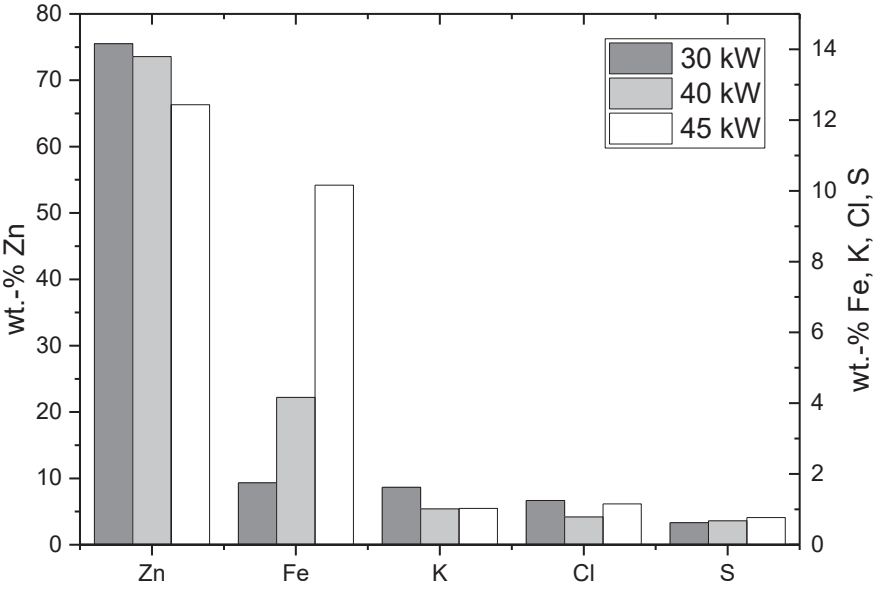

Figure 41: Analysis of the captured dust fraction

The analysis of the final slags can be seen in Figure 42. The major slag formers have similar concentrations within all slags. The ratio between lime and quartz is just below 1. The slags seem to be more compact when comparing them to the previous tests. The chromium oxide concentration depends on the power input. The final slag in the 30 kW trial reaches a value of 8.7 %. It falls to 1.3 % for the 40 kW and 0.7 % for the 45 kW experiment.

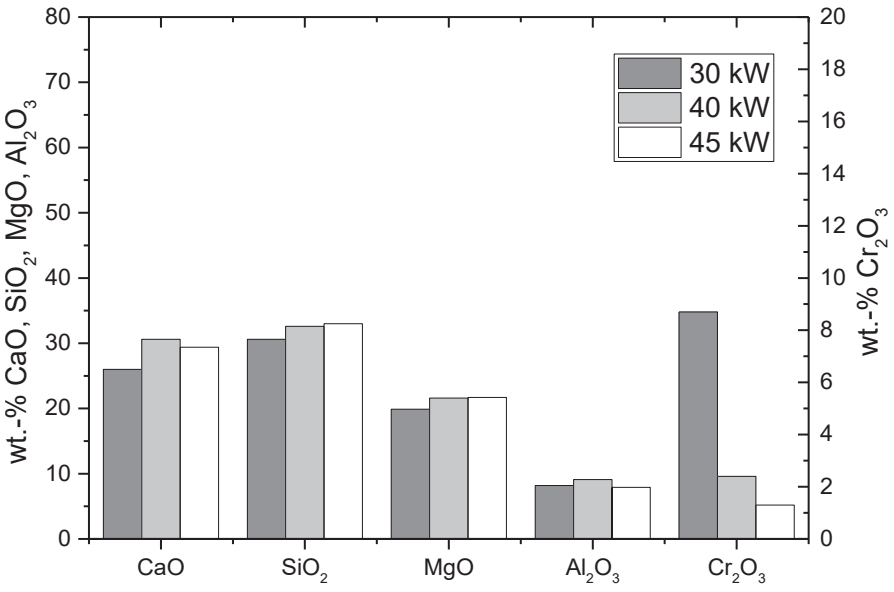

Figure 42: Analysis of the generated slags

Figure 43 shows the analysis of the produced ferroalloys with iron concentrations ranging from 80 to 85 %. The chromium concentration starts at 4.3 % for the 30 kW trial and reaches 11.8 % for the 45 kW trial, where almost all chromium was reduced out of the slag. Additionally, the ferroalloy contains notable amounts of molybdenum, nickel, tungsten, copper, manganese and vanadium. This large variation of different alloying elements is caused by the complex composition of the dust (details can be found in Chapter 4.4). Their concentrations are similar for all trials with the exception of manganese, because it is harder to reduce. This is why it shows the same tendency as chromium.

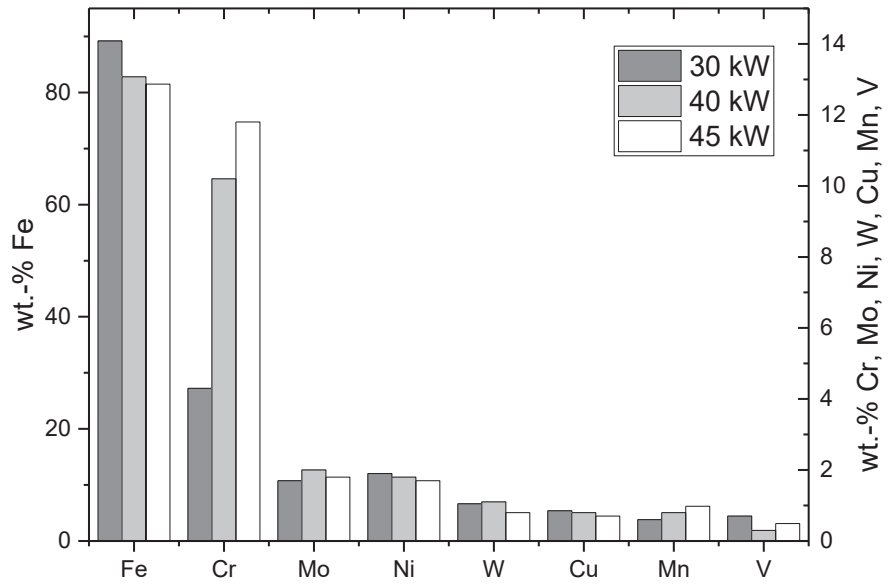

Figure 43: Analysis of the produced ferroalloys

Figure 44 displays the determined mass flows without the off-gas amount. The given input material mixture produces 393 to 458 g of zinc-enriched dust fraction, 1950 to 2148 g of slag and 393 to 458 g of ferroalloy. The differences between the different mass flows of the trials can be explained by

- different recovery rates for reducible compounds like chromium and manganese
- increased corrosion of the condenser or higher carry-over content due to more intense bubble bursting
- inhomogeneous composition of the fed dust material

Overall, an elevated temperature improves the reduction reactions, resulting in the production of less slag and more ferroalloy.

Figure 44: Mass flow for the trials at constant power input

6 Kinetic Studies

The previous chapters covered the thermodynamic basis, gave an overview of the different materials' properties and investigated their processibility. Finally, mass balances were calculated and compared to experimental data. The tests showed that the chromium reduction was the limiting factor. Consequently, the necessary treatment time in order to get satisfying recovery rates was investigated.

While the thermodynamic calculations of chemical equilibriums only explain a state of a reaction with no further tendency toward progress, kinetics can explain the way to reach this state. In other words, the chemical equilibrium defines – considering the recycling of residues – the maximum achievable recovery rate, but gives no information about the necessary reaction time. For this reason, kinetic models have to be developed.

6.1 Fundamentals of Kinetics

Outside the chemical equilibrium, a reaction rate can be defined as the concentration change of a substance per unit time. Generally, the reaction rate depends on the reactant and product concentrations. A reaction state that is far away from its equilibrium usually enhances the reaction rate. However, the reaction rate has more major influencing factors:

- temperature,
- pressure and
- presence of a catalyst.

In order to take place, a reaction between two substances has two requirements. On the one hand, reactants must collide; on the other, these collisions must overcome a specific energy barrier, the so-called activation energy of the reaction. The first aspect – the collision rate – is proportional to the concentration and can be described as the mathematical product between the reactants' concentrations and a specific collision constant "C" (Eq. 6.1). Considering that only a fraction "F" overcomes the reaction's activation energy, Equation 6.2 depicts the reaction rate as the number of successful collisions. The constants "C" and "F" can finally be summarized as the theoretical kinetic constant "$k_{theoretical.}$" This leads to Equation 6.3. [48]

$$Collision\ Rate \propto C \cdot [A] \cdot [B] \tag{6.1}$$

$$Reaction\ Rate = F \cdot C \cdot [A] \cdot [B] \tag{6.2}$$

$$Reaction\ Rate = v = k_{theoretical} \cdot [A] \cdot [B] \tag{6.3}$$

These constants are temperature-dependent. The constant “F” shows a higher dependency on temperature compared to “C,” but it can be decreased by the presence of catalysts. Literature reports that values close to zero are possible [48], which sets the fraction of successful collision close to 1 and leads to a reaction with little temperature dependence. However, kinetics usually change heavily with the temperature, which is why kinetic investigations require isothermal conditions. Complex reactions include various reaction steps, which makes the determination of an exact model difficult. Nevertheless, many reactions have a rate-limiting step that runs significantly slower. In this case, the concept of the rate-controlled step can help to reduce the complexity. [48–50]

Many reactions are found to follow a so-called reaction order model. A wide range of reactions are for the most part only influenced by the reactants’ concentration. Equation 6.5 outlines a generalized form of an order model for the reaction in Equation 6.4. [20]

$$[A] + [B] + [\dots] \rightarrow [C] \tag{6.4}$$

$$v = k_{(T)} \cdot [A]^a \cdot [B]^b \cdots \tag{6.5}$$

Coming back to stainless steel wastes, the studies in Chapters 4 and 5 pointed out that the reduction of chromium oxide can be seen as the determining factor of a carbothermic reduction treatment. Equation 6.6 shows the simplified – not considering the formation of carbides – carbothermic reduction reaction.

$$Cr_2O_3 + 3\ C \rightarrow 2\ Cr + 3\ CO \tag{6.6}$$

The experiments in Chapters 4 and 5 were performed in a graphite crucible and therefore, with an excess of carbon. For this reason, their activity can be assumed as a constant, so it can be ignored in the mathematic expression of the model. Applying the order model from Equation 6.5 to the reaction displayed in equation 6.6 results in Equation 6.7, where the reaction rate is proportional to the nth power of the chromium oxide concentration.

$$v = k_{(T)} \cdot [Cr_2O_3]^n \tag{6.7}$$

The reaction rate can also be described as the concentration change over time (Equation 6.8). Looking at 6.7 and 6.8 results in the differential Equation 6.9.

$$v = \frac{dCr_2O_3}{dt} \tag{6.8}$$

$$\frac{dCr_2O_3}{[Cr_2O_3]^n} = k_{(T)}\ dt \tag{6.9}$$

The integration of Equation 6.9 considers the special case of the first order, which leads to Equation 6.10. Finally, Equation 6.11 depicts the solution for reaction orders higher than one. These equations can be used to determine the kinetic constant, which requires the chromium course during an isothermal experiment. The concentrations can be used to calculate the values for each equation's left side and plot the result versus the time. The calculated points can then be used for a linear fit, where the slope represents the kinetic constant for a given temperature, as long as the reaction follows an order model.

$$\ln \frac{Cr_2O_{3_t}}{Cr_2O_{3_0}} = k_{(T)} \cdot t \qquad 6.10$$

$$\frac{1}{1-n} \cdot \left(\frac{1}{[Cr_2O_3]_t^{\,n-1}} - \frac{1}{[Cr_2O_3]_0^{\,n-1}} \right) = k_{(T)} \cdot t \qquad 6.11$$

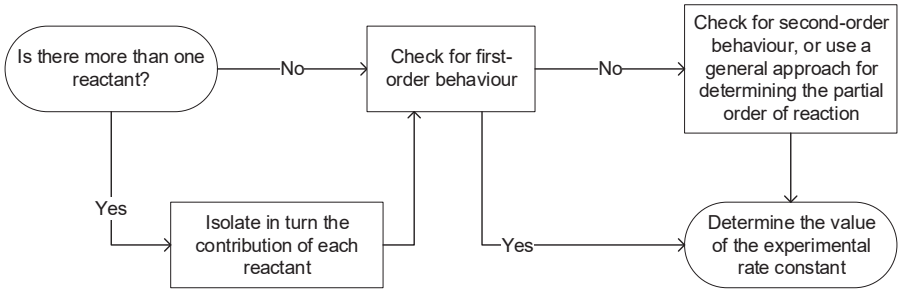

Figure 45: Strategy for the determination of an experimental rate equation [48]

Assuming that the reaction can be explained by an order model, the determination of n has to be done empirically. Mortimer et al. [48] suggest a strategy for this; the corresponding flow chart is shown in Figure 45. They suggest starting with first order behavior and increasing the order step-by-step.

The present method can be used to examine the kinetics when the concentration course of a substance versus the time is available. Since the kinetic constant is a function of temperature, such an investigation requires isothermal conditions during the experiment.

6.2 Fundamentals of Thermogravimetric Analysis

The carbothermic reduction of oxides produces carbon monoxide or carbon dioxide and consequently leads to a decrease in mass. Therefore, measurement of the mass over time can be used to describe the reaction's extent of conversion (α). However, this technique requires an isolated reaction, which is why it can only be applied to pure substances. These investigations are usually done in so-called thermogravimetric analyzers. Equation 6.10 shows the extent of conversion mathematically. The sample mass at the beginning is defined as m_0,

the mass after the full reaction as m_1 and the mass at a given time as m_t. Consequently, this method requires information about the mass change when all reactants have transformed into their products.

$$\alpha = \frac{m_0 - m_t}{m_0 - m_1} \tag{6.12}$$

If the reaction can be isolated and the sample mass can be used to calculate the extent of the conversion, the reaction rate can be described as its time derivative. This leads to Equation 6.13, which is similar to Equation 6.5, but a general approach for the kinetic model (described as $f_{(\alpha)}$) [51]. Referring to literature, the reaction mechanism can change during its progress. The rate constant $k_{(T)}$ is assumed to only be influenced by temperature and to be independent from pressure, since thermogravimetric analyses are normally performed with gas flushing at atmospheric pressure. [52]

$$v = \frac{d\alpha}{dt} = k_{(T)} \cdot f_{(\alpha)} \tag{6.13}$$

The temperature-dependent rate constant usually follows the so-called Arrhenius equation, as outlined in Equation 6.14. In this formula, A represents the so-called pre-exponential factor, E_a the activation energy and R the gas constant. If the reaction mechanism changes during its progress, the activation energy can change with the extent of conversion. [53]

$$k(T) = A \cdot e^{\frac{E_a}{RT}} \tag{6.14}$$

Equations 6.13 and 6.14 can be combined to form Equation 6.15. This differential equation has no analytical solution if the temperature changes over time, which is why various approximations were developed. Table 6 gives an overview of some reaction models. [52]

$$\frac{d\alpha}{f(\alpha)} = A \cdot e^{\frac{E_a}{RT}}\, dt \tag{6.15}$$

Table 6: Sample of ideal kinetic models

Nr	Reaction model	Code	$f(\alpha)$
1	Power law	P4	$4\alpha^{\frac{3}{4}}$
2	Power law	P3	$3\alpha^{\frac{2}{3}}$
3	Power law	P2	$2\alpha^{\frac{1}{2}}$
4	Power law	P2/3	$\frac{2}{3}\alpha^{-\frac{1}{2}}$
5	One-dimensional diffusion	D1	$\frac{1}{2}\alpha^{-1}$
6	Mampel (first order)	F1	$1-\alpha$
7	Avrami-Erofeev	A4	$4(1-\alpha)[-\ln(1-\alpha)]^{\frac{3}{4}}$
8	Avrami-Erofeev	A3	$3(1-\alpha)[-\ln(1-\alpha)]^{\frac{2}{3}}$
9	Avrami-Erofeev	A2	$2(1-\alpha)[-\ln(1-\alpha)]^{\frac{1}{2}}$
10	Three-dimensional diffusion	D3	$\frac{3}{2}(1-\alpha)^{\frac{2}{3}}[1-(1-\alpha)^{\frac{1}{3}}]^{-1}$
11	Contracting sphere	R3	$3(1-\alpha)^{\frac{2}{3}}$
12	Contracting cylinder	R2	$2(1-\alpha)^{\frac{1}{2}}$
13	Two-dimensional diffusion	D2	$[-\ln(1-\alpha)]^{-1}$

6.2.1 Kissinger's Method

The Kissinger method was published in 1956 and has been cited more than 3,000 times. It is known as an easy to use method that only needs the temperature at which the reaction rate reaches its maximum for a given heating rate. Mathematically, the basis originates from Equation 6.15. The maximum reaction rate can be described as an inflection point. This leads to Equation 6.16, which can be transformed into Equation 6.17, where β describes the heating rate and T_m the associated temperature at which the reaction rate reaches its maximum. The Kissinger method requires experiments that are performed by using different heating rates. A detailed derivation can be found in the referring literature. [52,54]

$$\frac{d^2\alpha}{dt^2} = 0 = A\left[-\frac{E_a}{RT_m^2}e^{-\frac{E_a}{RT}}f(\alpha) + e^{-\frac{E_a}{RT}}f'(\alpha)\right] \quad 6.16$$

$$\ln\frac{\beta}{T_m^2} = -\frac{E_a}{RT_m} \quad 6.17$$

An advantage is that Equation 6.17 is not limited to thermogravimetric data. In fact, all data that allows the identification of the maximum reaction rate is applicable, such as differential scanning calorimetry. However, some limitations exist [55]:

- It requires a constant heating rate
- $f'(\alpha)$ must be independent from the heating rate
- Derivation assumes a first order model; other kinetic models result in errors
- It is only valid for single-step reactions

6.2.2 Extented Kissinger Method

Farjas et al. present an alternative to the Kissinger method. A detailed derivation can be found in the referred primary literature [56]. The determination of the activation energy requires plots of the reaction rate over time at different heating rates. From these plots, the width at half the height of the reaction rate's maximum is defined as Δt_{FWHM}. This is shown in Figure 46. Finally, the activation energy can be determined by Equation 6.18. In order to check if the method provides a valid result, a plot of the normalized time against the reaction rate can be drawn. The normalized time can be calculated using Equation 6.21. If the curves from different heating rates are similar, the reaction can be assumed as limited by a single step. [56]

$$\ln(\Delta t_{FWHM}) = \frac{E_a}{RT_m} + \ln\frac{\Delta t_{FWHM}}{A} \qquad 6.18$$

$$t' = \frac{t}{\Delta t_{FWHM}} \qquad 6.19$$

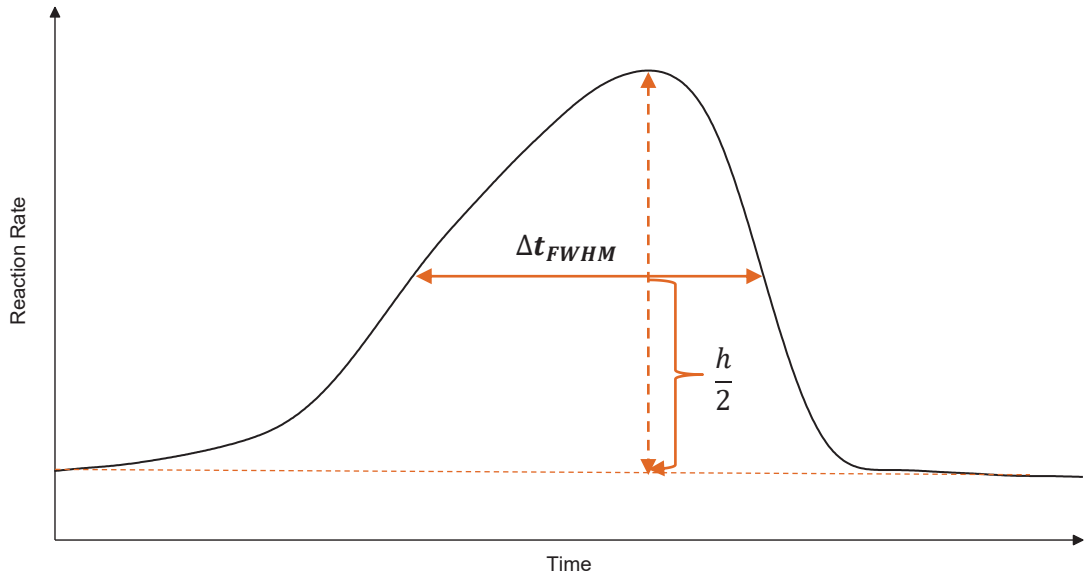

Figure 46: Determination of Δt_{FWHM}

6.3 Isoconversional Methods

The Kissinger method gives a single value for the activation energy. However, during the progress of a reaction, the rate-limiting step can change. Such reactions cannot be investigated by applying the Kissinger method. [52] Therefore, isoconversional methods have been developed. The mathematical derivation is explained in Equations 6.20 to 6.22. Equation 6.20 results from taking the natural logarithm of Equation 6.13. The partial derivation with respect to T^{-1} can be applied, assuming that a constant α leads to Equation 6.22. This formula describes a possibility of determining the activation energy at a given extent of conversion. It does not require any knowledge about the reaction model. For that reason, isoconversional methods are also called “model-free” methods. However, the methods assume that the reaction obeys some $f(\alpha)$, although the identification of the reaction model itself is not required. [57]

$$\ln\frac{d\alpha}{dt} = \ln k(T) + \ln f(\alpha) \tag{6.20}$$

$$\left[\frac{\partial \ln\frac{d\alpha}{dt}}{\partial\frac{1}{T}}\right]_\alpha = \left[\frac{\partial \ln A\cdot e^{\frac{E_a}{RT}}}{\partial\frac{1}{T}}\right]_\alpha + \left[\frac{\partial \ln f(\alpha)}{\partial\frac{1}{T}}\right]_\alpha \tag{6.21}$$

$$\left[\frac{\partial \ln\frac{d\alpha}{dt}}{\partial\frac{1}{T}}\right]_\alpha = -\frac{E_\alpha}{R} \tag{6.22}$$

Depending on the mathematical approach, Vyazovkin et al. split isoconversional methods into:

- Differential methods
- Integral methods [57]

On the one hand, differential methods use the differential form from Equation 6.15. They require differential data such as the reaction rate. On the other hand, integral methods integrate Equation 6.15, which is why data that corresponds to the extent of conversion can be used. However, no time integral exists for the Arrhenius equation as long as the temperature depends on the time – which is usually the case in thermogravimetric analysis. Integral methods include mathematical approximations, which are a potential source of errors.

6.3.1 Method of Friedman

Friedman’s method represents a differential isoconversional approach. Equation 6.23 shows the method. It can be derived by applying the isoconversional principle to Equation 6.15 [58]. The model includes no mathematical approximations, but requires differential data, which is difficult to obtain accurately. Usually, the first derivation of the extent of conversion is used.

Differential experimental data usually generates noise, which normally requires smoothing. Chapter 6.5 gives a more detailed illustration of the problem.

$$\ln\left(\frac{d\alpha}{dt}\right)_{\alpha,i} = \ln[f(\alpha) \cdot A_\alpha] - \frac{E_\alpha}{RT_{\alpha,i}} \quad 6.23$$

A more practical notation of Equation 6.23 can be obtained by assuming a constant heating rate β (Equation 6.24). Only then is it possible to eliminate the time in Equation 6.25. Finally, a reaction's activation energy can be determined by plotting $\ln\left(\beta\frac{d\alpha}{dT}\right)$ versus $\frac{1}{T}$. The slope of the line generated by linear regression represents $\frac{E_\alpha}{R}$.

$$\beta = \frac{dT}{dt} \quad 6.24$$

$$\ln\left(\beta\frac{d\alpha}{dT}\right)_{\alpha,i} = \ln[f(\alpha) \cdot A_\alpha] - \frac{E_\alpha}{RT_{\alpha,i}} \quad 6.25$$

6.3.2 Integral Methods

The Arrhenius equation – the right side of Equation 6.15 – has no analytical solution for the temperature integral. Therefore, approximations are necessary. Starink et al. demonstrated that many approximations lead to a similar equation. This generalized form can be seen in Equation 6.26 [59]. The constants a and b represent numerical values and depend on the applied approximation method. The activation energy can be determined by plotting $\ln\frac{\beta}{T_\alpha^a}$ versus $\frac{1}{T_\alpha}$ for a specific extent of conversion at a given heating rate. Such a study requires data from experiments performed at different heating rates.

$$\ln\frac{\beta}{T_\alpha^a} = Constant - b\frac{E_a}{R \cdot T_\alpha} \quad 6.26$$

6.3.2.1 The Flynn-Wall-Ozawa Method

Equation 6.27 shows an approach that is often referred to as the Flynn-Wall-Ozawa method. Details regarding the derivation can be found in the referred literature [60]. Comparing it with Equation 6.26, the rough approximation used leads to a value of 0 for the constant a and 1.052 for b. The activation energy can be determined by plotting the logarithm of the heating rate against the reciprocal of the isoconversional temperatures obtained for different heating rates. The isoconversional temperature corresponds to the temperature at which a specific extent of conversion is reached.

$$\ln\beta = \ln\frac{A \cdot E_a}{R \cdot g(\alpha)} - 5.331 - 1.052\frac{E_a}{RT_\alpha} \quad 6.27$$

6.3.2.2 The Kissinger-Akahira-Sunose Method

Kissinger's method, described in Chapter 6.2.1, assumes a first order reaction. Kissinger, Akahira and Sunose proposed a more generalized form that uses an approximation worked out by Doyle (Equation 6.28) [61]. The approximation behind it presumes a constant heating rate [55]. Some rearranging of Doyle's approximation leads to Equation 6.29. The final formula looks similar to the Kissinger method from Equation 6.17, but it requires a different set of data. Furthermore, the backgrounds are different. In order to determine the activation energy, the isoconversional temperatures for different heating rates have to be found.

$$g(\alpha) \equiv \int_0^\alpha \frac{d\alpha}{f(\alpha)} = \frac{A}{\beta}\int_{T_0}^{T} e^{-\frac{E}{RT}}dT \approx \frac{ART^2}{\beta E_a} \cdot e^{-\frac{E}{RT}} \quad 6.28$$

$$\ln\frac{\beta_i}{T_{\alpha,i}^2} = \ln\left(\frac{RA}{E_\alpha \cdot g(\alpha)}\right) - \frac{E}{RT_{\alpha,i}} \quad 6.29$$

6.3.2.3 Determining Reaction Models by the Use of y(α) Master Plots

The isoconversional methods are capable of estimating the activation energy without any knowledge of the reaction model. The activation energy can be used to identify the underlying model if the reaction is limited by a single step. Therefore, the activation energy should be constant during the reaction's progress. The mathematical background in Equation 6.30 comes from a simple rearrangement of Equation 6.15. The left side of the equation can be calculated with experimental data obtained at different heating rates. As activation energy E0, the average of Eα can be used. This data can be used to draw the y(α) plots for the experimental data. Additionally, the formulas from Table 6 can be used to draw the y(α) master plots, after which all curves have to be normalized. Finally, the corresponding reaction model can be identified. [52]

$$y(\alpha) = \left(\frac{d\alpha}{dT}\right)_\alpha \beta \cdot e^{\left(\frac{E_0}{RT_\alpha}\right)} = A \cdot f(\alpha) \quad 6.30$$

6.4 Model Fitting

The isoconversional methods explained are valid for single-step kinetics only. More complicated reactions require other approaches like the model fitting method. Theoretically, data from a single trial can be used in order to determine all kinetic parameters, but in order to get reliable results, data from experiments performed at different heating rates are recommended [52]. The necessary data basis is similar to the isoconversional models. Vyazovkin et al. suggest the following questions before starting with the model fitting method [52]:

- Is there evidence for multi-step kinetics?
- Does the activation energy change with the extent of conversion when applying isoconversional methods?
- Is the reaction type acceleratory, decelerated or sigmoidal?
- Is it possible to compare the reaction profile's shape with normalized plots from literature?

An example of a model fitting method is the combined kinetic analysis. It uses a generalized kinetic model in the form of Equation 6.31. By adjusting the parameters c, m and n, various ideal kinetic models can be fitted extremely accurately. The combination of Equations 6.31 and 6.15 results in Equation 6.32:

$$f(\alpha) = c \cdot \alpha^m (1-\alpha)^n \tag{6.31}$$

$$\ln\left(\frac{d\alpha}{dT}\beta\frac{1}{\alpha^m(1-\alpha)^n}\right) = \ln(c \cdot A) - \frac{E_a}{RT} \tag{6.32}$$

Equation 6.32 allows the calculation of a pair of values that have a linear correlation if an appropriate kinetic model is applied. Numerical optimization for the parameters can be used in order to maximize the correlation coefficient. Thermogravimetric data has high relative errors for the extent of conversion close to zero and one; so, limitation to data between 0.1 and 0.9 should be considered. The pre-exponential factor can be calculated if an ideal kinetic model fits the data. Otherwise, the determination of the pre-exponential coefficient is not possible. Generally, the linearization often magnifies small-value points' sensitivity. The main advantage of this method is the determination of the kinetic model simultaneously to the activation energy.

6.5 Thermogravimetric Study on the Chromium Reduction

This chapter describes the investigation of the carbothermic reduction of chromium oxide. The thermogravimetric analyses were performed in a Netzsch STA 409. Its maximum heating rate is 50 °C/min and it can reach a maximum temperature of 1,450 °C. The conversion of the

measured mass-loss to a corresponding value for the extent of conversion requires exact knowledge of the underlying reaction. The steps for the chromium oxide's carbothermic reduction can be found in Table 7. The carbon content of the carbides decreases with increasing temperature, which is why the production of metallic chromium requires a high temperature.

Table 7: Steps of the carbothermic reduction of chromium oxide [62]

Reaction	**Equilibrium temperature**
$3Cr_2O_3 + 9C \rightarrow 2Cr_3C_2 + 9CO$	1,150 °C
$5Cr_2O_3 + 27Cr_3C_2 \rightarrow 13Cr_7C_3 + 15CO$	1,190 °C
$Cr_2O_3 + 3Cr_7C_3 \rightarrow Cr_{23}C_6 + 3CO$	1,530 °C
$2Cr_2O_3 + Cr_{23}C_6 \rightarrow 27Cr + 6CO$	1,810 °C

The given information can be used to create a stoichiometric mixture between chromium oxide and carbon. The assumed reaction's temperature range indicates the formation of Cr_7C_3. The mixture must contain a ratio of chromium oxide to carbon that completely reacts to Cr_7C_3 and carbon monoxide without any leftover of reactants. For the described thermogravimetric study, 30.48 g carbon were mixed with 100 g chromium oxide. In order to achieve a homogeneous distribution, the mixing procedure was done in a vibration mill. A test was performed to prove the validity. Figure 47a displays the sample's relative mass and the temperature in respect to the time. The heating rate was 50 °C/min at the beginning, and 10 °C/min at higher temperatures where the reaction was assumed to run. The temperature range in which the reaction takes places is approximately 1,100 °C to 1,200 °C. At a higher temperature, only a negligible mass loss can be observed. Figure 47b shows the corresponding extent of conversion that was calculated using Equation 6.33:

$$\alpha = \frac{100 - m_t}{100 - 57.6} \cdot 100 \qquad 6.33$$

The trial demonstrates that the thermogravimetric analyzer's reachable temperature is sufficient for a study of the chromium oxide reduction because the reaction's major part takes place between 1,100 °C and 1,200 °C.

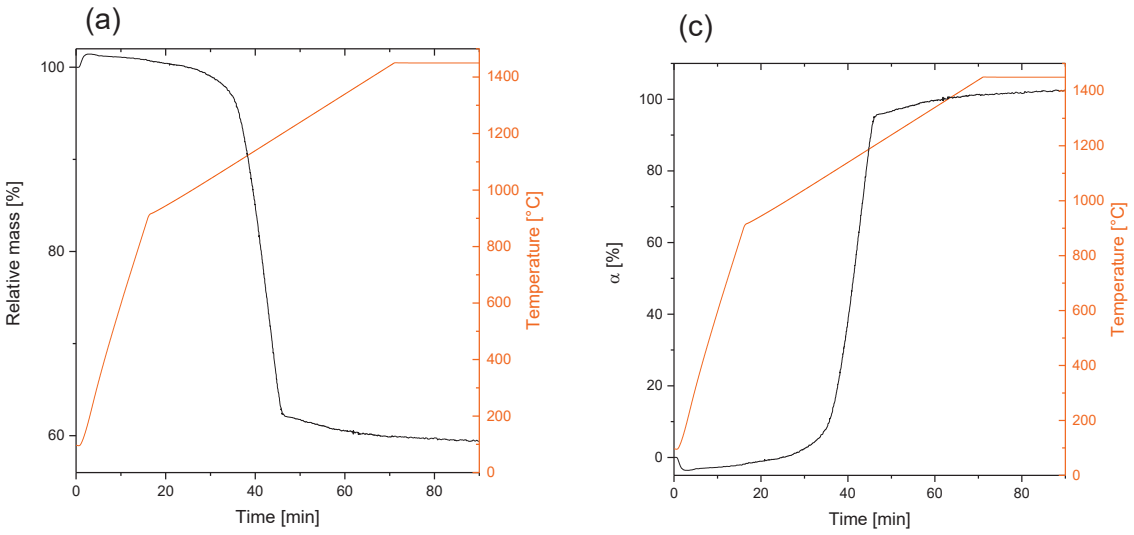

Figure 47: (a) thermogravimetric analysis and (b) calculated extent of conversion for a heating rate of 10 °C/min

Some kinetic evaluation methods require differential data. If the raw data points are not steady, smoothing is mandatory because numerical differentiation results in an amplification of the noise. Figure 48 compares data from numerical differentiation. Figure 48a can be obtained by applying the noise-containing raw data to the differentiation algorithm. The plot is hardly usable for any evaluation. If a smoothing algorithm is applied before the derivation is calculated, the algorithm output results in usable data (Figure 48b). Finally, a second smoothing of the derivation can be applied in order to get a smooth curve. However, it is important to bear in mind that such processing results in errors that may influence further findings.

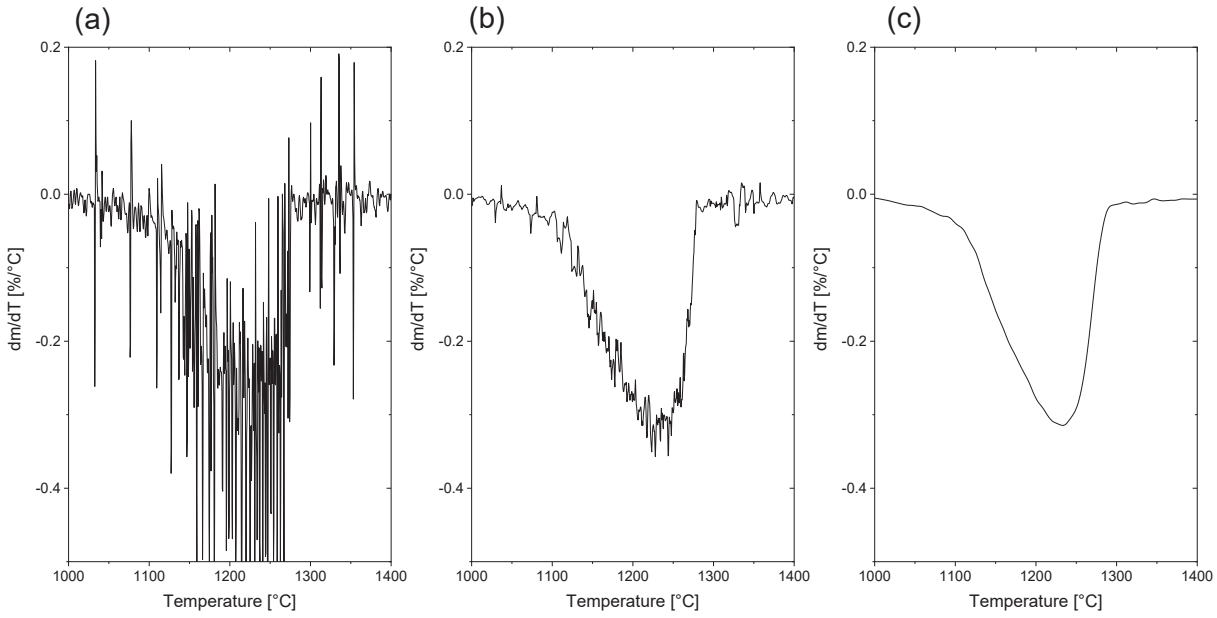

Figure 48: Visualization of the necessity of smoothing. Showing numerical differentiation (a) without smoothing (b) smoothing of the mass course (b) smoothing of the mass course and the first derivation

Kinetic Evaluation of the Carbothermic Reduction

The previous chapters highlighted the necessity for varying heating rates for a thermogravimetric study of a reaction's kinetics. Therefore, the experiments performed included the heating rates 10 °C/min, 15 °C/min, 20 °C/min, 30 °C/min, 40 °C/min and 50 °C/min. The weight of the sample material was between 100 g and 110 g. Figure 49a shows the noise-containing raw data of the experiments. Some methods require the time derivate of the extent of conversion, which can be calculated by means of numerical differentiation. Therefore, a smoothing function has to be applied in order to minimize this issue. Figure 49b shows the curves after a smoothing. This procedure was performed with the included smoothing function of OriginPro 2017. The method used was "Adjacent Averaging". Finally, Figure 49c shows the corresponding extent of conversion for the test.

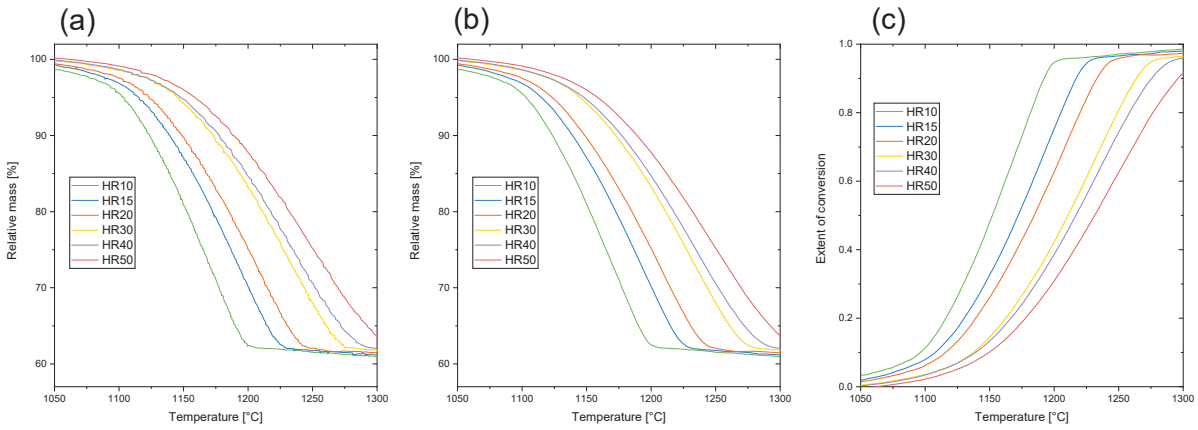

Figure 49: Visualization of the experimental data for the TGA of the chromium oxide reduction

The Kissinger method is the approach most often used to determine the activation energy, which is why it represents the first method for the evaluation. Equation 6.17 requires the temperature at which the maximum reaction rate occurs for a given heating rate. Figure 50a shows the derived reaction rates over the temperature. For the derivation, the smoothened mass courses were derived by numerical differentiation using OriginPro 2017. The heating rate influences the form of the curves. This indicates that the mechanism of the chromium oxide reduction differs from a first-order reaction model or it doesn't have a single limiting step. However, the Kissinger method still gives a good approximation of the activation energy. The effective activation energy results from the slope of the line in Figure 50b. Its value is found to be 371.2 kJ/mol.

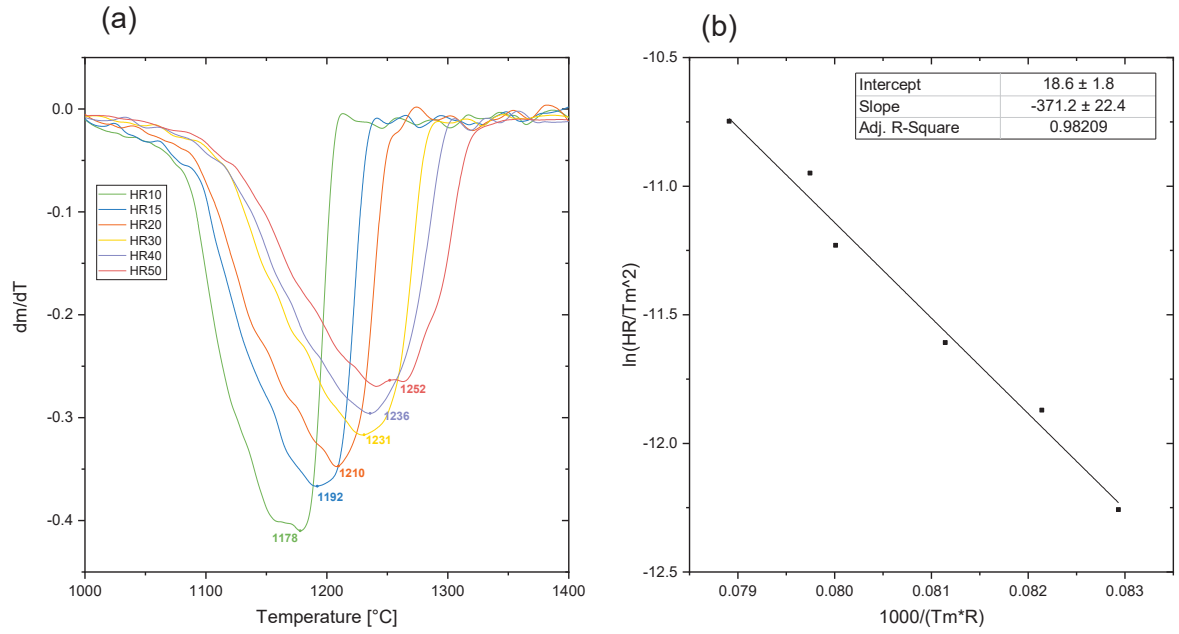

Figure 50: Kissinger-like analysis: (a) detection of the temperature at which the maximum reaction rate occurs and (b) determination of the activation energy

In order to validate the Kissinger approach, the alternative method described in Chapter 6.2.2 can be used. The according plots are shown in Figure 51. The activation energy is found to be 321.9 kJ/mol, which is similar to the 371.2 kJ/mol that are found using the Kissinger method. Additionally, the normalized time plots' shape is similar for all heating rates. This indicates that the reaction is limited by a single step.

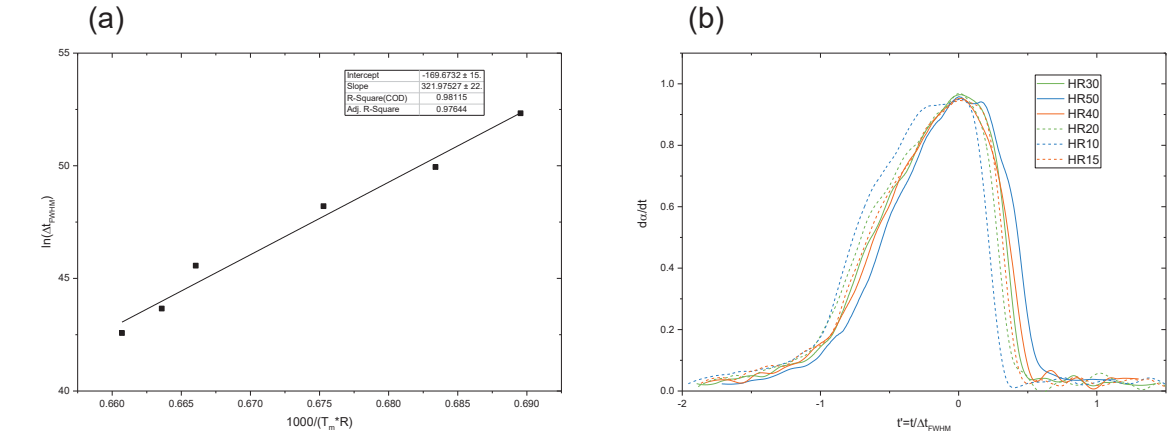

Figure 51: Method according to Farjas et al. (a) plot to determine the activation energy (b) normalized time plots that prove the methods validity

Integral methods require the knowledge of the correlation between temperature and extent of conversion for a given heating rate. Moreover, differential methods require the information about the correlation between reaction rate and the extent of conversion. This data can be derived by means of the numerical differentiation of the extent of conversion. As explained above, smoothing operations are required in order to obtain solid data. Figure 52a illustrates the connection between temperature and extent of conversion for different heating rates. Figure 52b shows the same information for the reaction rate. The thermogravimetric data is inaccurate for α lower than 0.2 and higher than 0.9.

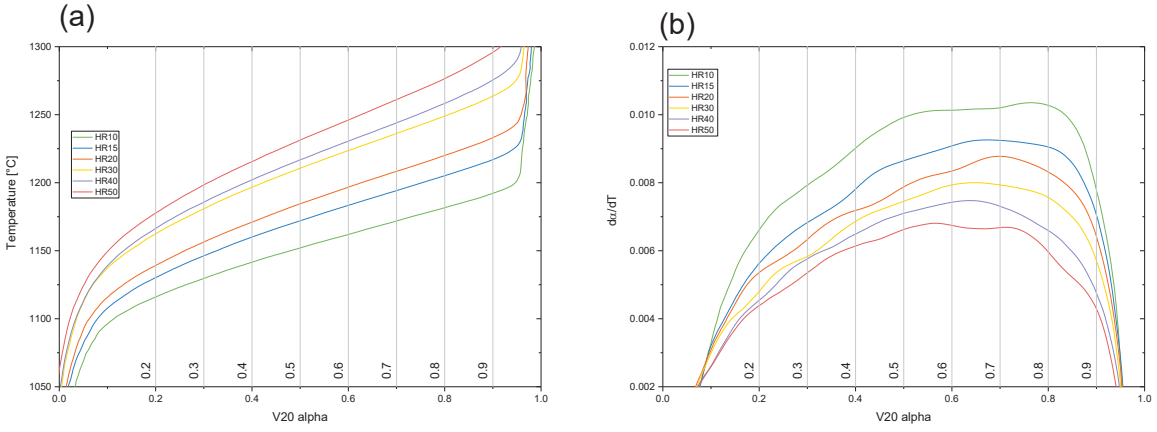

Figure 52: (a) connection between the temperature, extent of conversion and heating rate and (b) connection between the reaction rate, extent of conversion and heating rate.

The data from Figure 52a and Figure 52b can be applied to the isoconversional methods as detailed in the previous chapter. The equations used are the Kissinger-Akahira-Sunose, Flynn-Wall-Ozawa and Friedman method. Figure 53 displays the plots that result from the isoconversional equations. Each data point originates from a specific heating rate. More trials with varying heating rate led to more data points. The linear fitting was performed using OriginPro 2017. The resulting lines show good correlation for all data points. The slope of the straight lines decreases with increasing extent of conversion for all applied methods. In other words, the activation energy decreases during the reaction's progress. Consequently, a change of the reaction mechanism cannot be rejected.

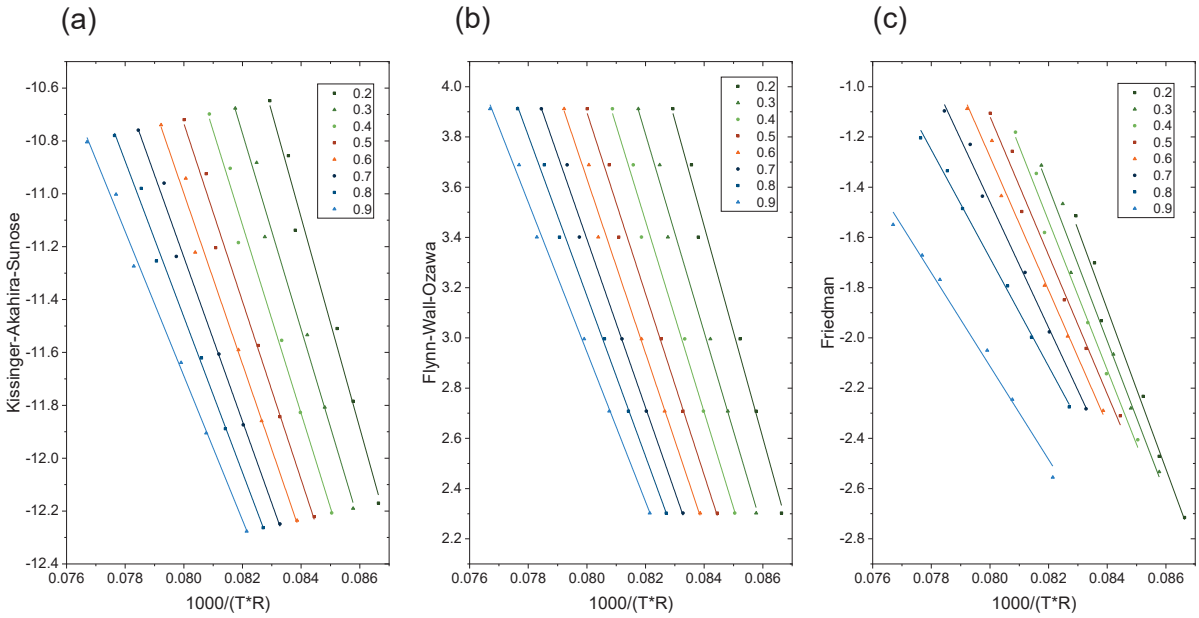

Figure 53: Isoconversional plots (a) Kissinger-Akahira-Sunose (b) Flynn-Wall-Ozawa and (c) Friedman

Figure 54 summarizes the trend of the activation energy for the applied methods; the standard deviation from the linear regression is displayed as bars. Each method results in different values for the activation energy. Generally, the evaluation contains greater errors at smaller α. This means that the experimental data's accuracy is lower at the beginning compared to the later stage of the reductions. Nevertheless, Figure 54 demonstrates decreasing activation energy while the reaction progresses. The value of the activation energy ranges from 200 kJ/mol to 320 kJ/mol for Friedman and from 421 kJ/mol to 272 kJ/mol for the integral methods. The gap may be caused by the smoothing operation. Especially the integral methods results are similar to the outcome of the standard Kissinger method (371.2 kJ/mol).

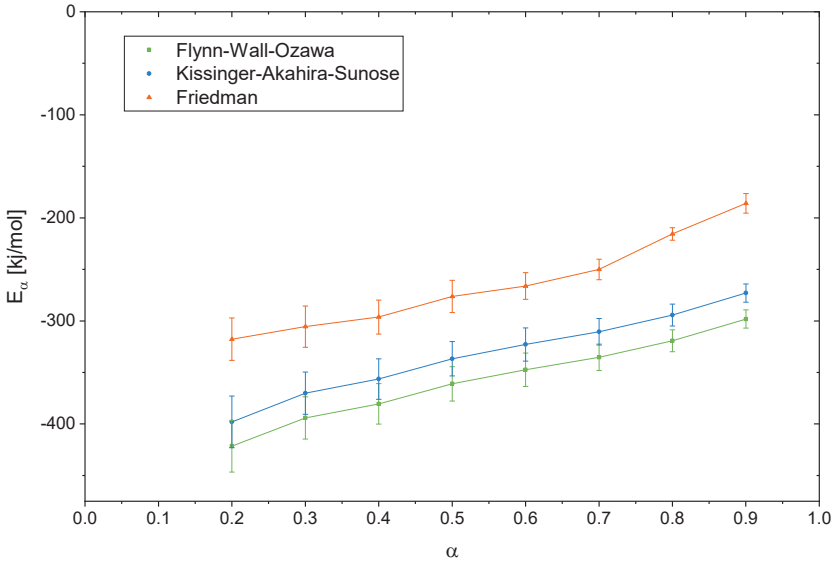

Figure 54: Determined activation energies depending on the method used and the extent of conversion

After the estimation of the activation energy, the evaluation of the reaction model is possible with the application of the y(α) master plot technique. Figure 55a displays the master plots for the reaction models from Table 6. A description of the method itself can be found in Chapter 6.2. The plots in Figure 55b illustrate the experimental data. The major requirement – curve shape's independence from the heating rate – is fulfilled. This indicates that the reaction model is limited by a single step throughout the reaction's progress. Possible matching models are the diffusion models D1, D2 and D3. An exact identification is not possible with the y(α) master plot method.

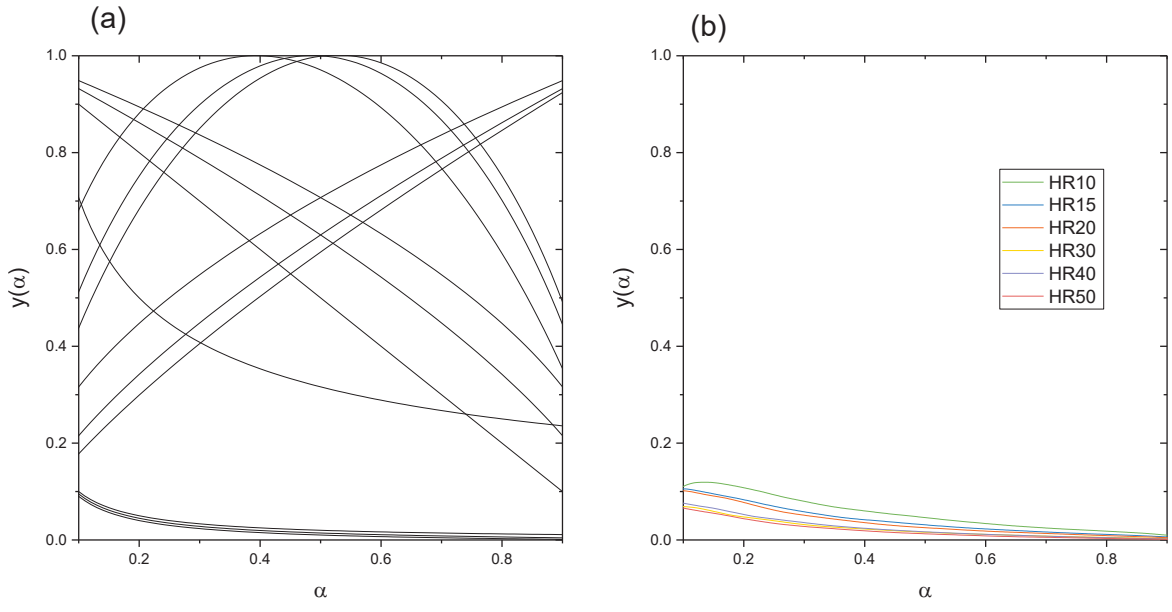

Figure 55: y(α) master plots for models from literature and a comparison with the experimental data

The combined kinetic analysis plots all data in one diagram. If the applied model portrays the kinetic mechanism accurately, the resulting data points lie on a straight line. Figure 56a shows the outcome of the application of the one-dimensional diffusion model, where the data points deviate significantly from a straight line. The result is better for Figure 56b, which applies a two-dimensional diffusion model. However, the three-dimensional diffusion model gives the best description of the reaction. Considering the underlying principles from Equation 6.32, the slope correlates to the reaction's activation energy. Nevertheless, an exact determination with this approach is difficult due to the shift within the different experiments' data.

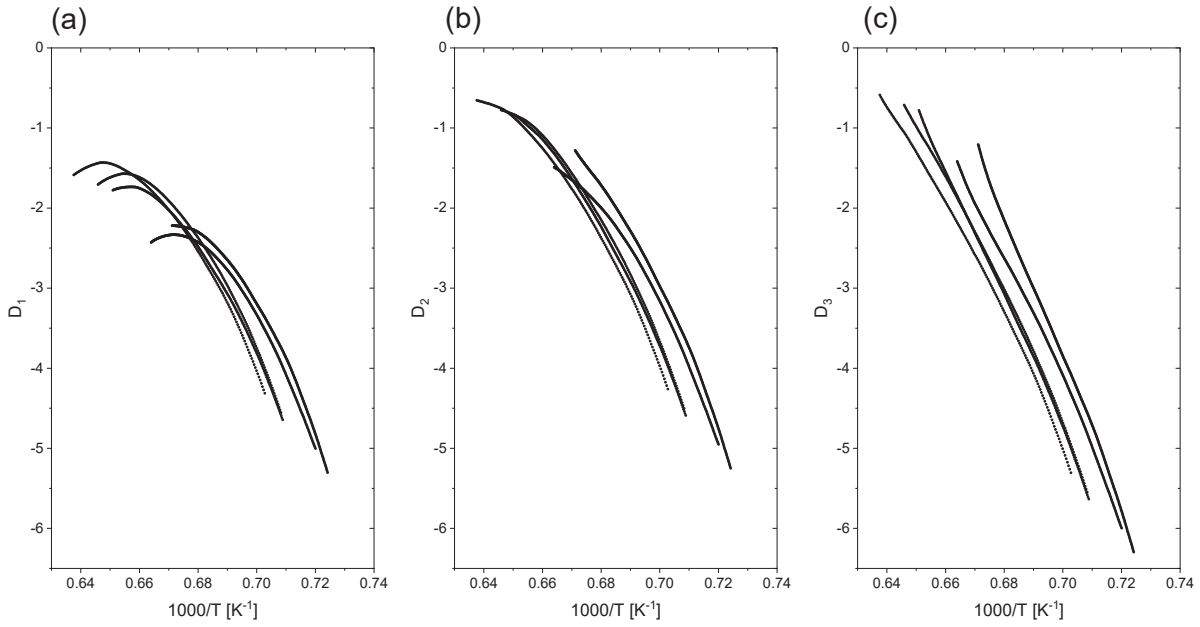

Figure 56: Model fitting for different kinetic models: (a) one-dimensional diffusion (b) two-dimensional diffusion and (c) three-dimensional diffusion

The thermogravimetric analysis conducted gives basic details of the reduction reaction. The experiments in the laboratory scale include pure substances and a controlled atmosphere, which is why a direct conversion of the results is not possible. However, the study can be used to validate the melting lab's results. The main outcomes of the thermogravimetric analysis are:

- The reduction reaction starts at approximately 1,100 °C, which is the same as calculated using thermodynamic data from HSC 7
- The reaction mechanism seems to be diffusion-controlled
- The value of the activation energy depends on the method applied and decreases while the reaction progresses. The values found range from roughly 200 kJ/mol to 400 kJ/mol. It seems legitimate to presume a single step limitation of the reaction.

The final slags from the experiments outlined in Chapters 4 and 5 still have considerable chromium concentrations. In order to allow for a zero waste approach, the final chromium concentration has to be lower than 0.25 %. The thermogravimetric study indicates a diffusion-

controlled reaction model highly influenced by the reactants' concentrations. The reaction rate slows down rapidly as the concentration of chromium oxide decreases. This is why reaching low chromium concentrations seems to require long treatment times. However, the high value of the activation energy implies that the reaction kinetics are highly influenced by the temperature, so the next chapter investigates the temperature influence on the reaction kinetics for the melting lab scale.

7 Kinetical Investigations in an Induction Furnace

The kinetic investigation of the chromium oxide reduction included a carbothermic reduction melting of residues from the stainless steel industry. The literature study in Chapter 2 declares 0.25 % to be the maximum chromium concentration in the final slag. Therefore, the objective is to study the chromium oxide behavior at already low concentrations in the liquid slag. The first experimental campaign only included EAF slag.

7.1 Implementation of a Temperature Measurement System

The process temperature represents an important parameter when investigating a material's reduction behavior. However, the characterization trials in Chapter 4 and the mass balance trials in Chapter 5 were performed to study the pyrometallurgical processibility and the distribution of different elements in the melting lab. In those cases, precise information about the process temperature was not necessary. In contrast, kinetical investigations require accurate knowledge about the temperature at which the chemical reactions run. This is why research regarding possibilities for measuring the melt temperature for the given treatment process was conducted.

In fact, such a measurement has to deal with three major challenges:

- Process temperature up to 1,700 °C, where type B thermocouples are typically used
- Aggressive slag system that dissolves the protective cover normally used for type B thermocouples
- Induction field that can distort the measurement without adequate shielding

These conditions are the reason why direct measurement by the use of a thermocouple was dismissed. Instead, the application of an indirect measurement by using a pyrometer was considered. During the initial tests, the slag's surface temperature was measured. However, several reasons make this method inaccurate:

- The emission coefficient of the melt depends on the slag's composition. Since the treatment changes the slag's composition, the emission coefficient may also change during the treatment.
- The generation of dust can affect the measurement in both directions. Usually, the dust fraction will cool as it leaves the furnace. This causes an underestimation of the temperature. Nevertheless, when considering the exothermal re-oxidation reaction of gaseous zinc to zinc oxide, it can also lead to an overestimation.
- Finally, the reduction reaction produces carbon monoxide that leads to slag foaming. The slag foam has low thermal conductivity and acts as insulation. Under such circumstances, the surface temperature will drop due to thermal radiation. Like the

slag's composition, the slag foam changes during the treatment, so it is not possible to offset the resulting error.

In order to overcome these issues, an indirect measurement of the crucible's bottom temperature is considered to be more accurate. This, however, poses two major challenges:

- The use of a solid crucible with preferably high thermal conductivity is necessary
- A temperature offset exists between the crucible's and the melt's temperature.

For the given investigations, a graphite crucible that exhibits high thermal conductivity is used. The occurring temperature shift of the measurement can be corrected by calibration measurements using a thermal probe. Figure 57 shows the experimental setup that was used for the experiments. It is similar to the one used in Chapter 1.1.2. The only difference is the added pyrometer.

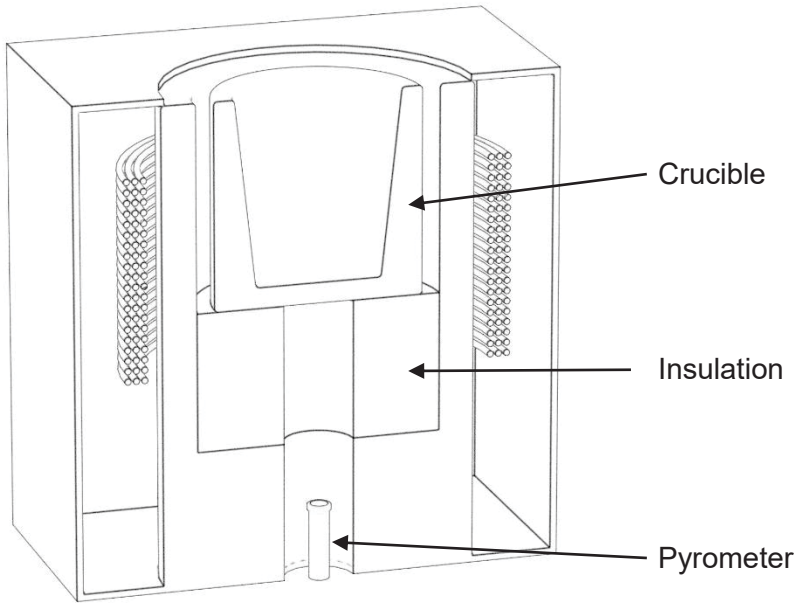

Figure 57: Concept of the experimental setup

7.2 Experimental Procedure in the Induction Furnace

The process temperature influences the reduction kinetics significantly. For that reason, some tests had to be performed in order to evaluate the validity of the experimental setup.

For each experiment in the campaign, a preheating or more precisely a temperature-homogenization phase was performed prior to feeding the residual materials. The crucible's preheating to 1,700 °C was followed by a 30-minute holding period. After that, the material was fed into the furnace. For the investigation of the chromium oxide concentration over time, each trial included the sampling of eight slag samples at different stages of the treatment. The time between sampling ranged from 5 to 10 minutes. Afterwards, the slag samples were ground,

homogenized and analyzed by using a scanning electron microscope via energy-dispersive X-ray spectroscopy. The comparison of ICP-MS and EDX in Chapter 4.2 proved sufficient accuracy of the EDX analysis for chromium.

7.2.1 Pyrometer Tests

In order to validate the temperature measurement method, three trials were performed. In addition to the experimental procedure with a continuous temperature measurement via a pyrometer, the slag temperature was determined by the use of a thermal probe. Figure 58a-c summarizes the acquired temperature data from the pyrometer (orange line) and the thermal probe (blue line). Furthermore, the difference between these values is shown in green. According to the thermal probe, the investigation in Figure 58a was performed within a temperature range of 1,682 °C to 1,705 °C. The data shows a slight increase in the temperature gap with increasing slag temperature. However, the temperature difference (ΔT) between both measurement methods is negligible. The same can be said for the other trials. Since the heat losses go down with falling temperatures, ΔT declines with decreasing temperatures.

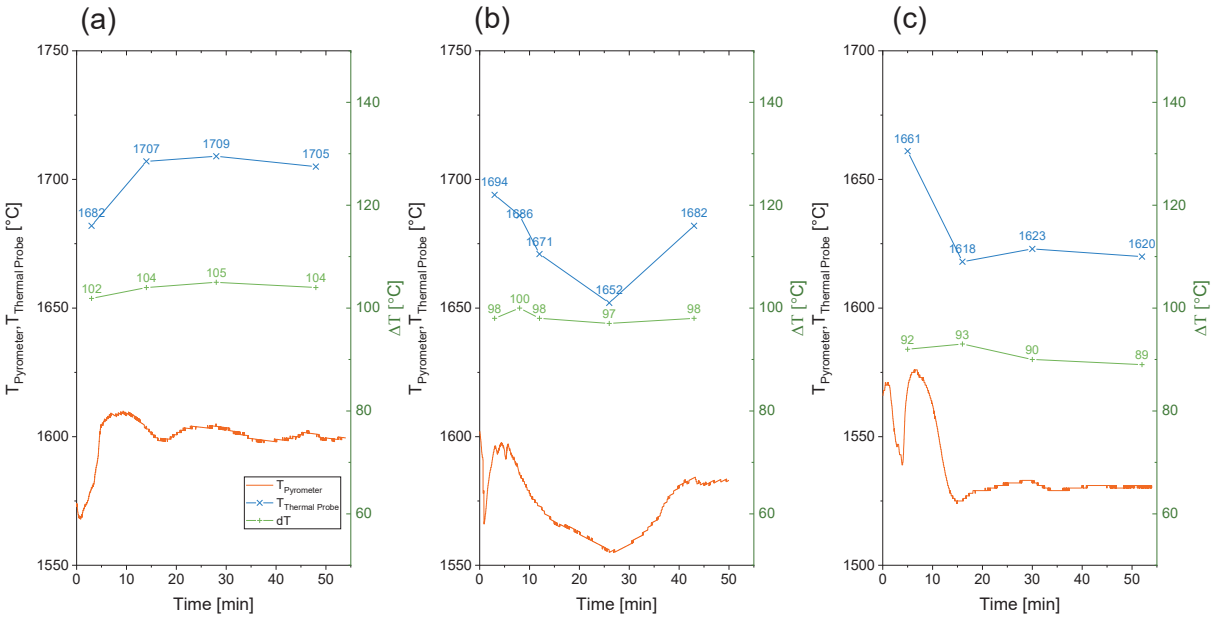

Figure 58: Temperature calibration for the pyrometer in the induction furnace

The calibration trials confirm the validity of the experimental setup. Nevertheless, the temperature fluctuation during the experiment is high. The reason can be found in the manual control of the power input, although it was done as accurately as possible. Consequently, an automated control had to be implemented.

7.2.2 Implementation of a PID Controller

The idea of automation includes reading the measured temperature, calculating the necessary furnace power by applying a PID algorithm and finally, providing this information to the furnace. The first step included the evaluation of possible ways to regulate the power input of the furnace. In the past, the control of the power input was done manually using a rotary potentiometer. Most machines that include a programmable logic controller (PLC) are controllable by the use of an analog input channel. This analog signal can be either a voltage or a current, normally in the range between 0 and 10 V or 0 and 20 mA and maps, for example, the power input from 0 to 100 %. Since the induction furnace used has such a PLC, it was assumed to include such an analog input. However, after contacting the support of the manufacturer, it turned out that the PLC of the induction furnace is implemented differently. The idea was to simulate the rotary potentiometer by using digital potentiometers. Although this sounds easy, digital potentiometers include different restrictions:

- Digital potentiometers can handle small currents only.
- While traditional potentiometers are passive compounds, they have no limitations regarding the applied voltage to ground as long as they are operated within their power rating. In other words, a mechanical potentiometer only considers the voltage difference between its wired connections and not the absolute voltage to ground. Digital potentiometers work differently. In this case, voltage to ground must not exceed the positive supply voltage of the digital potentiometer – usually 5 V. Therefore, it can only be used in circuits that do not exceed their supply voltage.
- Finally, the minimum value for the resistance of a digital potentiometer is significantly higher than zero.

The next step was the examination of the furnace control loop to stay within these restrictions. In order to do so, the control cabinet was opened. Then, for different potentiometer resistance settings, the current and voltage drop were measured. The determination of the power input depending on the potentiometer setting can be seen as the final step. Figure 59 summarizes the electrical characteristics of the control loop. Figure 59a shows that the electrical current does not follow Ohm's law. Instead, the current and resistance have a negative linear relationship. Considering Figure 59a, the maximum voltage drop is 1.15 V. Finally, the furnace power input is proportional to the resistance of the potentiometer. It reaches its maximum at 800 Ω. In addition, a further measurement showed that the voltage drop in this position of the circuit is equal to the voltage to ground value.

The survey of the control loop led to the following requirements for the digital potentiometer:

- Resistance range from close to zero up to 1000 Ω
- An applicable current of at least 3 mA

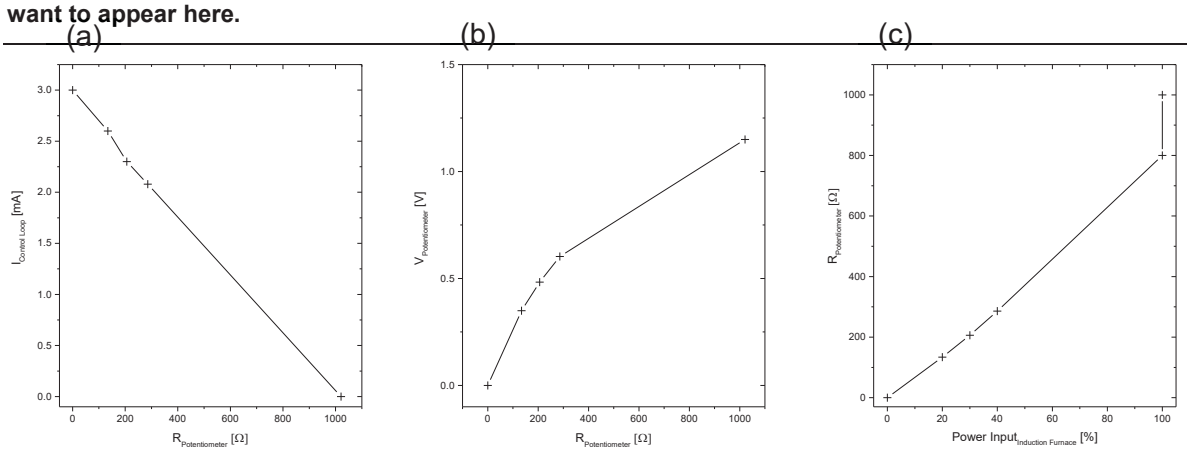

Figure 59: (a) current over the potentiometer resistance (b) voltage drop on the potentiometer and (c) the furnace power input depending on the potentiometer resistance

After the compilation of the necessary specifications for a digital potentiometer, the next step was to select an appropriate microprocessor that could read the temperature measured with the pyrometer, apply it to a PID algorithm and communicate the regulating value to the digital potentiometer.

7.2.2.1 Selection of Components

The parameters for the selection of a proper microcontroller are good documentary, flexibility and reliability. Since similar projects are often realized with an Arduino board, it was also chosen for this project. The requirements set for the digital potentiometer led to the selection of the AD8400 from “Analog.” Its datasheet lists a resistance of 1 kΩ and a maximum current of 5 mA. Additionally, it can be controlled via the Serial Peripheral Interface (SPI) that is supported by the Arduino. Generally, digital potentiometers have a minimal wiper resistance. The real resistance of the potentiometer ranges from 40 to 1200 kΩ.

7.2.2.2 PID Algorithm

The proportional, integral and derivative (PID) algorithm was developed in the 1930s and still represents the fundamentals of basic control application. It consists of a proportional, integral and derivative part. The principle of the proportion control is to keep the controller output proportional to the error. The integral control eliminates the offset of the error. Finally, the derivate control considers the actual development of the error; hence, it will work against quick changes in the system. A detailed explanation of the background of a PID algorithm can be found in literature [63]. The mathematical form of the implemented algorithm can be described as follows:

$$output(t) = K_p \cdot error(t) + \int_0^t K_i \cdot error(t)\, dT + K_d \frac{derror(t)}{dt} \qquad 7.1$$

In the present case, the error is the difference between the desired and measured temperatures. The coefficients K_p, K_i and K_d define the behavior of the controller.

7.2.2.3 Schematic Representation of the PID Controller

Figure 60 displays a schematic representation of the implemented automatic temperature control unit. The central interface is an Arduino. It receives the desired temperature from the processing interface and the measured temperature from the pyrometer. This data is applied to a PID algorithm that calculates an output value that sets the resistance of the digital potentiometer “AD8400.” Additionally, all data is transferred back to processing where it is saved. The data between “Processing” and Arduino is transferred via serial communication. The data from the pyrometer is read as a linearized voltage signal that represents the temperature. The communication with the digital potentiometer takes place through Serial Peripheral Interface.

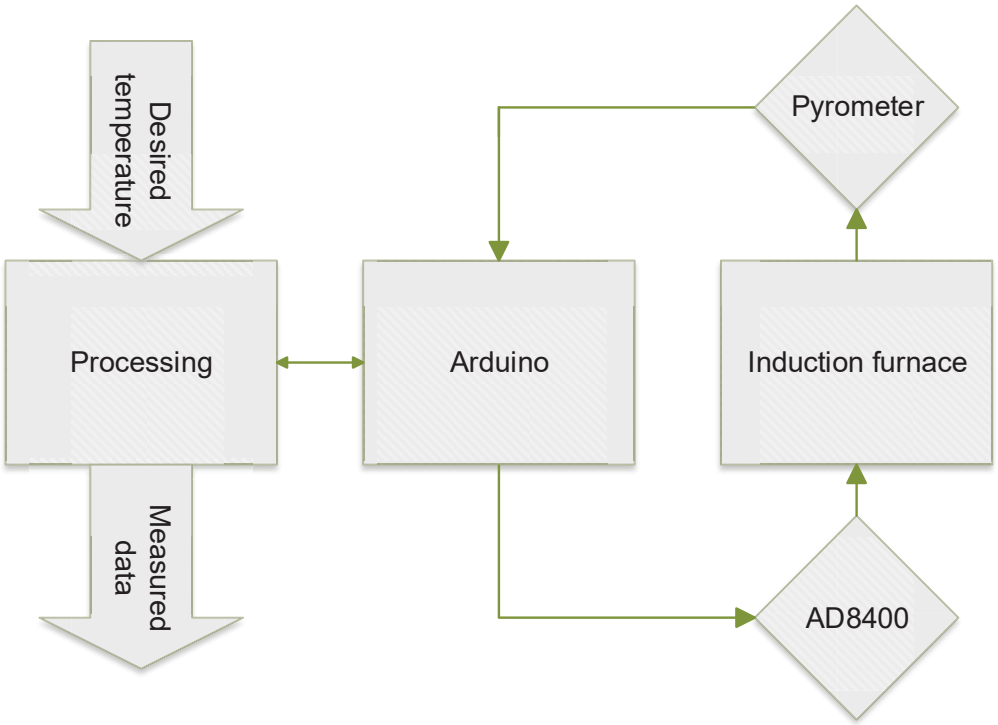

Figure 60: Schematic representation of the furnace control circuit

7.2.2.4 Test and Optimization of the Controller

After finding reasonable values for the coefficients, first tests were performed. In order to do this, an empty graphite crucible was used. The system reacts slowly to changes, which is why a proper derivative control is essential. After some trial and error testing, K_p was set to 3, K_i to 0.1 and K_d to 140. Figure 61 summarizes the data obtained from the test performed. The values for the proportional, integral and derivative controller are displayed in Figure 61a. The maximum output of the PID controller was set to be 60. The microprocessor translates this

value to a resistance of 600 Ω, which correlates to a power input of approximately 40 kW. However, the power input depends on which crucible is used and may change when the size and form of the crucible is changed. The present thesis always works with a similar experimental setup for the induction furnace. Additionally, the maximum integral output was set to 42. This intervention prevents the controller from overshooting. The controller output was limited to 60 for the first 3 minutes. Since the measured temperature gets closer to the desired temperature, the proportional part decreases. After 3 minutes, the derivative part influences the controller to lower its output. Finally, the slope of the measured temperature decreases (Figure 61b), which causes the derivative part to decrease. Since the temperature gap is already eliminated, the integral part is predominant after reaching the desired temperature. The maximum overshoot is 3 °C, which can be seen as a good result. Nonetheless, the controller output varies widely. When looking back at Figure 61a, this jumping is caused by the derivative control. Consequently, bigger changes in the measured slope of the temperature should be avoided in order to get a more stable output value. This was accomplished by introducing a low pass filter to the signal for the measured temperature. Additionally, the derivative value of the controller output was smoothed using a moving average calculation.

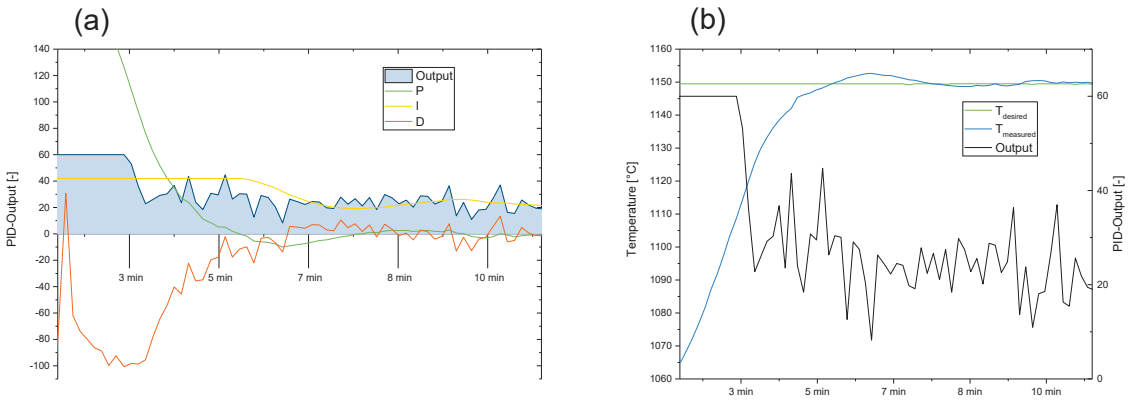

Figure 61: Evaluation of a test run using the PID algorithm: (a) detailed visualization of the algorithm's calculation results; (b) time course for the desired and measured temperatures

The first test run showed almost perfect behavior of the PID controller, so after adapting the algorithm, another test that already included the melting of a slag was performed. Figure 62 displays the results of this test. The added filter and smoothing functions led to a more consistent derivative part (Figure 62a). Furthermore, the furnace power out shows fewer fluctuations. Figure 62b displays the desired and measured temperatures. It shows a fast reaction to changes in the desired temperature. Furthermore, when feeding cold material into the furnace, the temperature drop is compensated in the best possible way. That is, it only took about 5 minutes to reach the desired temperature. A little overshooting was detected, so there

may be room for improvement; however, the controller meets all requirements to ensure a constant process temperature.

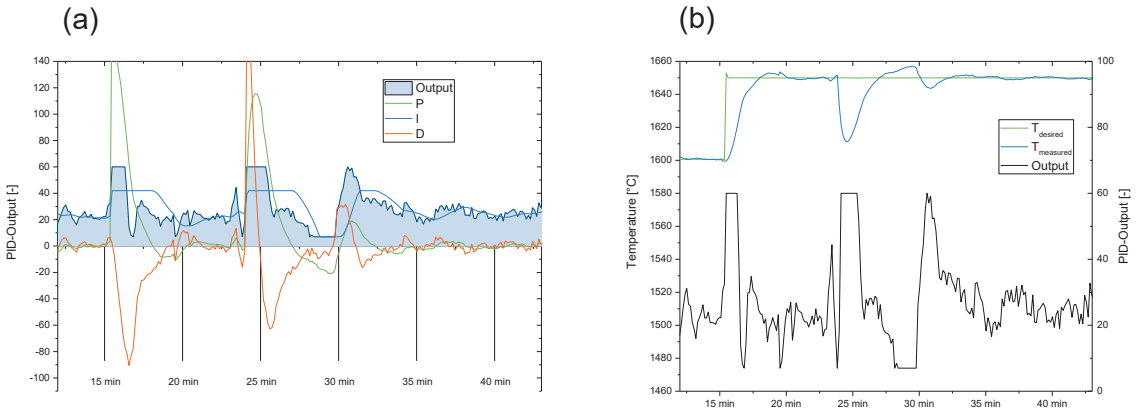

Figure 62: Evaluation of the PID controller and its usability when melting a slag at a high temperature: (a) detailed visualization of the results of the calculations from the algorithm; (b) time course for the desired and measured temperatures

The last step was to test the controller behavior during a steady state situation as it occurs during an experiment. Figure 63 displays the acquired data. When comparing the result to previous test runs, the integral part can be seen as the major influencing factor when comparing it to the proportional and derivative parts. Generally, the measured temperature fluctuations are negligible. The peak after 73 minutes was caused by removing the top cover of the furnace.

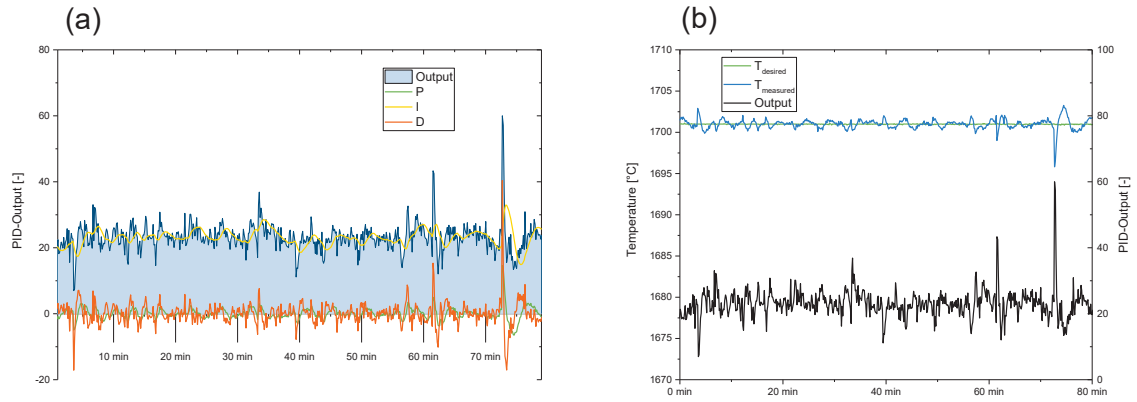

Figure 63: Evaluation of the PID controller and its usability during a steady-state situation: (a) detailed visualization of the results of the calculations from the algorithm and (b) time course for the desired and measured temperature

Further improvement of the PID controller was stopped at this point, because the results presented can be seen as a satisfying solution to operate the induction furnace at a given, constant temperature.

7.3 Reduction Kinetics of Chromium Oxide in Slags

A description of the test procedure applied during this study can be found in Chapter 4. The amount of feed materials for this campaign was 3.5 kg of stainless steel slag and 0.5 kg of pig iron. This investigation includes 9 experiments in a temperature range between 1,617 °C and 1,705 °C. However, most trials were performed in the range between 1,650 °C and 1,670 °C because higher temperatures cause fast oxidation of the graphite crucible. Nonetheless, one test was executed at 1,705 °C. The graphite crucible had to be replaced after each trial and consequently, the system had to be calibrated again via a thermal probe. Prior to each experiment, the desired temperature had to be estimated roughly, but its value had to be adjusted mathematically after the calibration measurement. In order to prevent slag losses, the temperature was only measured after taking all samples. Table 8 shows the measured temperatures before the tapping for all performed trials.

Table 8: Nomenclature of the performed tests

Identifier	Temperature	Identifier	Temperature
TrA	1,617 °C	TrF	1,666 °C
TrB	1,620 °C	TrG	1,667 °C
TrC	1,625 °C	TrH	1,674 °C
TrD	1,659 °C	TrI	1,705 °C
TrE	1,665 °C		

Figure 64a-c displays the concentration course for these trials. Correlating to the kinetic literature study, the decline of the concentration is steeper at elevated temperatures. Generally, the treatment time was decreased for trials that were performed at elevated temperatures because of the increased reaction kinetics.

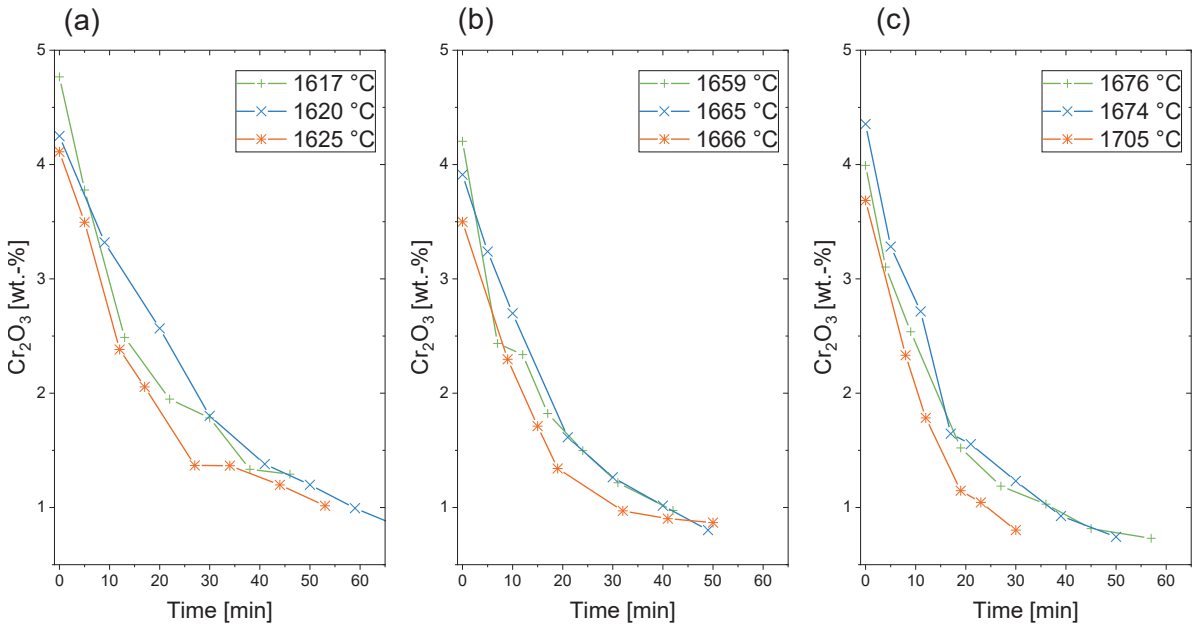

Figure 64: Chromium oxide's concentration course for (a) 1,617 °C to 1,625 °C, (b) 1,659 °C to 1,666 °C and (c) 1,667 °C to 1,705 °C

In addition to chromium oxide, the investigated slag also contains a notable manganese concentration. However, in contrast to chromium, the reduction speed of manganese is lower. Figure 65 shows that for the trials that were performed at the lower end of the temperature range, no verifiable manganese reduction occurred. With increasing temperature, some reduction of the manganese is observable. Nonetheless, compared to chromium oxide, the kinetics are slow. When comparing the concentration courses in Figure 64 and Figure 65, it seems that there is a critical concentration for chromium oxide that prevents the reduction of manganese oxide.

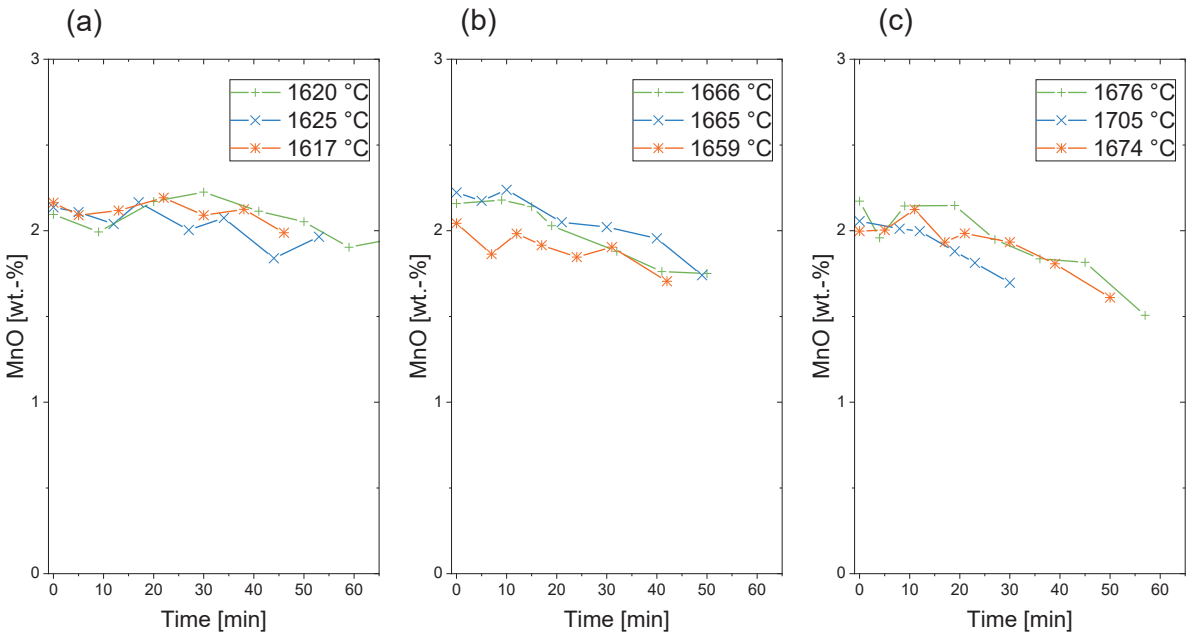

Figure 65: Manganese oxide's concentration course

The concentration courses of the slag compounds for the trials that were performed at 1,620 °C and 1,705 °C are displayed in Figure 66. Plots for the rest of the experiments in this experimental campaign can be found in the appendix. The relative amount of the major slag builders (CaO, SiO_2, Al_2O_3, MgO) increases during the treatment, majorly due to the chromium reduction. The slag basicity B_2 ranges from 1.6 to 1.8. Fluctuations within the same experiment may be caused by inhomogeneities that occur during the sampling or by errors from the analysis. However, the variation is small and does not negatively influence the validity of the experimental data.

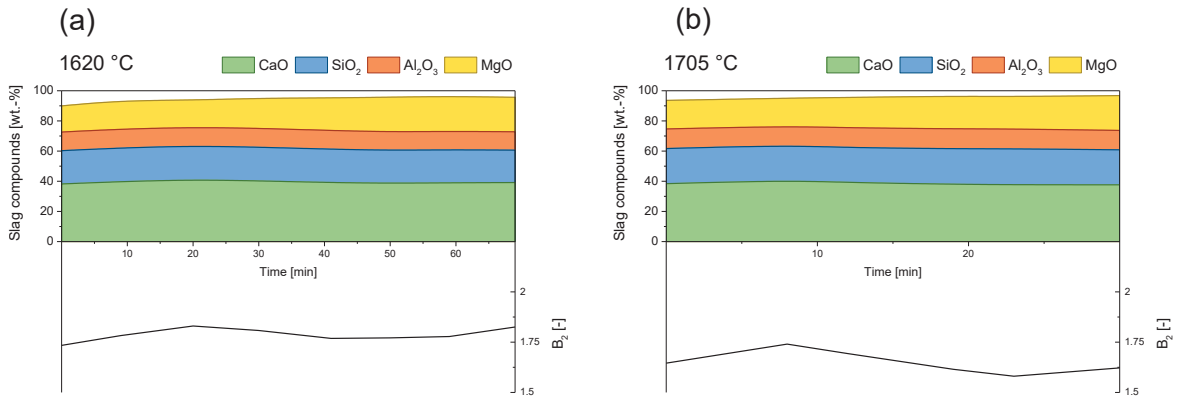

Figure 66: Development of slag compounds and basicity B_2 over time for (a) 1,620 °C and (b) 1,705 °C

7.3.1 Evaluation of a Kinetic Model

The theoretical background for the evaluation of the chromium oxide reduction kinetics was described in Chapter 6.1. The first step is the detection of an appropriate kinetic model. This is usually done by applying the data to different kinetic models via a trial and error procedure. The chromium oxide concentration courses for different temperatures in Figure 64 show that the reaction rate decreases during the treatment. The concentration in the slag is assumed to have a major influence on the kinetics. This is why this evaluation applies an order-model that only includes the chromium concentration in the slag. Its exact influence on the kinetics is described by the parameter n. Table 9 gives an overview of the parameters selected to be described in the present thesis. Other models were also investigated but rejected, as they did not fit the given data.

Table 9: Selected models to be tested against the experimental data

Identifier	**n**
Model A	1.0
Model B	1.5
Model C	2.0
Model D	3.0

Equations 6.10 and 6.11 can be applied to the experimental data in order to draw a linear plot – an appropriate fitting model is presumed. Equations 7.2 and 7.5 describe the mathematical background. If a kinetic model generates – for a given temperature – data points that lie on a straight line, it is capable of expressing the kinetics of the reaction.

$$y(t)_{n=1} = \ln\frac{Cr_2O_{3_t}}{Cr_2O_{3_0}} = k_{(T)} \cdot t \qquad 7.2$$

$$y(t)_{n>1} = \frac{1}{1-n} \cdot \left(\frac{1}{[Cr_2O_3]_t{}^{n-1}} - \frac{1}{[Cr_2O_3]_0{}^{n-1}}\right) = k_{(T)} \cdot t \qquad 7.3$$

The calculation of the y-value includes the chromium oxide concentration at the beginning (subscript 0). The value of the first sample has an influence on the result. Although it does not influence the estimation of the kinetic constant, it is more difficult to draw the fitted function. For this reason, the equations have to be transformed.

$$y(t)_{n=1} = \ln Cr_2O_{3_t} = k_{(T)} \cdot t + \ln(Cr_2O_{3_0}) \quad 7.4$$

$$y(t)_{n>1} = \frac{1}{1-n} \cdot \left(\frac{1}{[Cr_2O_3]_t^{n-1}} \right) = k_{(T)} \cdot t + \frac{1}{1-n} \frac{1}{[Cr_2O_3]_0^{n-1}} \quad 7.5$$

This method requires the calculation of data points from the experiments for different model orders to find the best fitting approach. The plots can be seen in Figure 67. The more accurately a model fits, the less deviation occurs between the linear regression and the data points. The plots in Figure 67 do not allow for a simple determination of the best fitting model because the variation between the different model orders is too low. Model A only shows a good fit for trials at 1,620 °C, 1,659 °C and 1,705 °C. Compared to that, Model B gives a good description of all experiments performed, although some minor deviations exist for the trial at 1,666 °C. The result for model C is similar to that of model B; however, slight deviations can be noticed for the trials at 1,625 °C, 1,666 °C and 1,667 °C. Finally, model D seems to give a meaningful fit for most trials. However, the linearization and visualization in Figure 67 distorts the true error between the experimental data and the applied models, because a higher order n results in smaller values for y(t) in Equation 7.5. This is why fitting reports of the linear regressions cannot be compared for different models, as the coefficient of determination will be higher for higher order models even though they may have a higher deviation in the non-linearized form.

For this reason, Figure 68 gives a non-linear visualization of the experimental data and the kinetic models by applying the parameters that were found with the linear regression. It demonstrates that model D shows a large variation from the experimental values, although the linear regressions in Figure 67 seem to fit well.

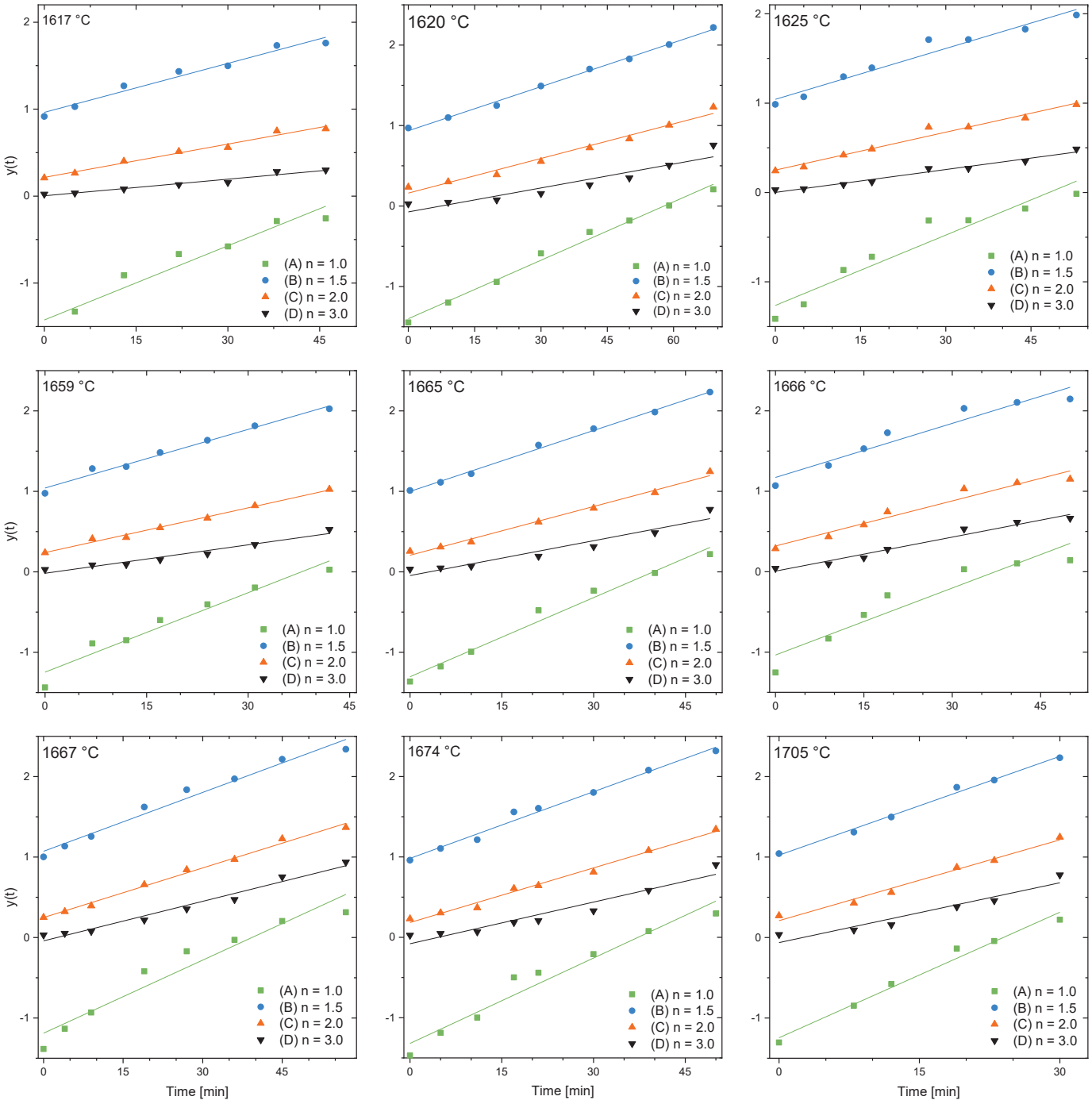

Figure 67: Applying different kinetic models to the experimental data via Equations 7.4 and 7.5

Model A provides an accurate description of the concentration course for the trial that was performed at 1,620 °C. In all other experiments, it underestimates the reaction rate at the beginning and overestimates the reaction rate at the end of the process. In contrast, models B and C give – with few exceptions – a good description of all trials.

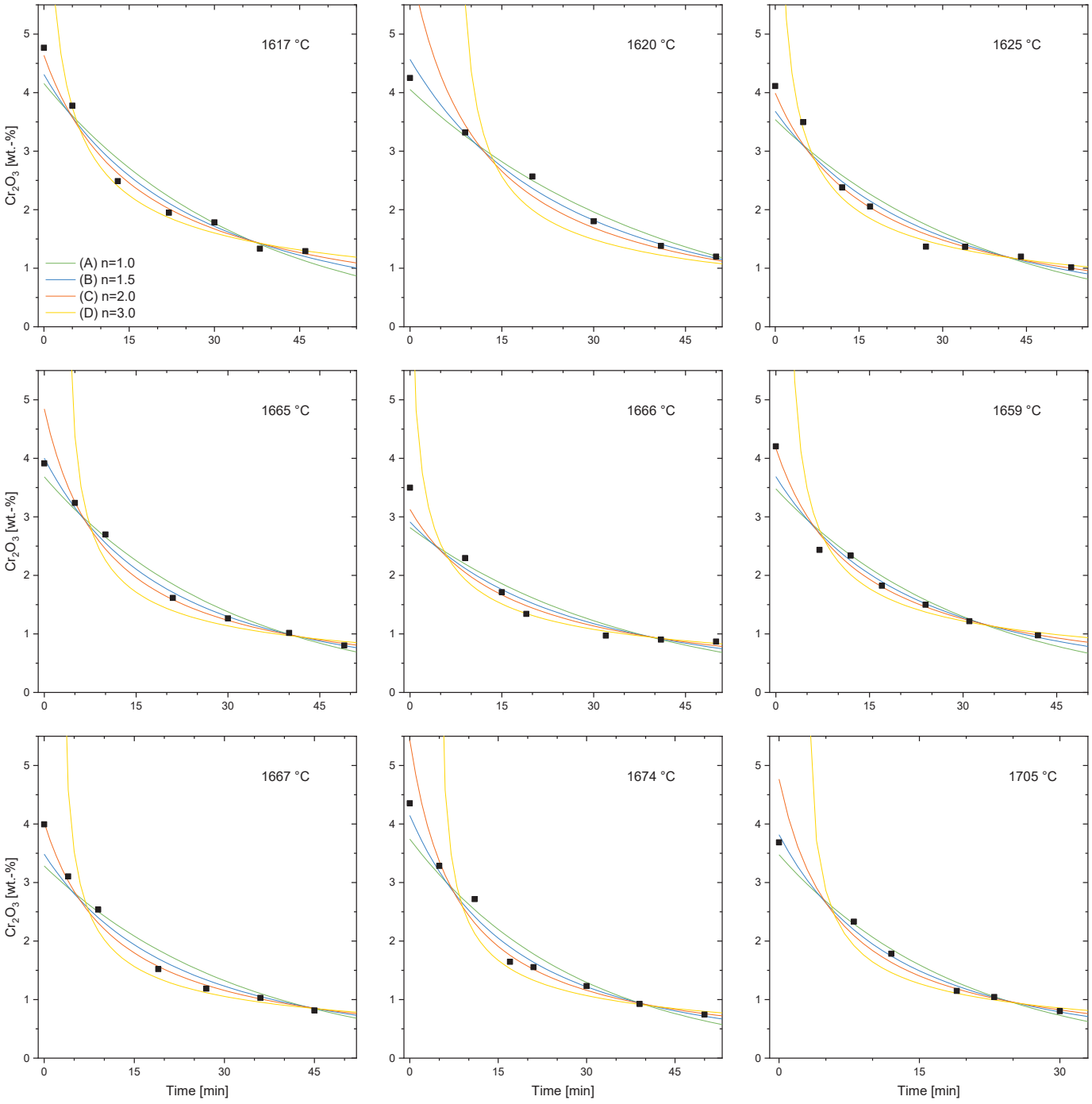

Figure 68: Comparison of the experimental data with the kinetic models in a non-linearized form

Since the visual evaluations do not allow for a sufficient rating of the model, the relative errors between the experimental and predicted data were calculated using Equation 7.6 for each experiment. Since model D fits significantly worse, it is not included.

$$rel\ Error = \frac{\sqrt{\left(Concentration_{measured} - Concentration_{predicted}\right)^2}}{Concentration_{measured}} \cdot 100 \qquad 7.6$$

Then, the mean relative error was calculated for each experiment and model. The corresponding values are listed in Table 10. The average error between prediction and analyzed concentration is 9.3 % for model A, 6.1 % for model B and 6.5 % for model C. The accuracy of models B and C are nearly the same, which is why a further study of the error has to be performed.

Table 10: Mean relative deviation between the predictions and the experimental data

	(A) n=1.0	**(B) n=1.5**	**(C) n=2.0**
1,617	9.5 %	7.3 %	4.8 %
1,625	12.2 %	8.2 %	4.5 %
1,659	8.4 %	5.5 %	3.5 %
1,674	10.7 %	5.8 %	7.6 %
1,705	5.7 %	3.6 %	9.3 %
1,665	6.4 %	3.1 %	6.4 %
1,676	12.4 %	8.0 %	3.8 %
1,666	13.5 %	10.4 %	8.1 %
1,620	4.5 %	3.0 %	10.6 %
Average	**9.3 %**	**6.1 %**	**6.5 %**

Table 10 lists the relative errors. Considering the fact that the relative EDX analysis error increases with decreasing concentration, it is useful to compare it with the mean absolute error. Table 11 compares the absolute error values. Applying model A results in a mean error of 0.19, model B in 0.13 and model C in 0.17. Together with the values of Table 10, model C, compared to model B, gives a significantly worse prediction at higher concentrations. As a result, model B is determined as the best fitting model for this type of evaluation that includes the linear regression according to Equations 7.4 and 7.5.

Table 11: Mean absolute deviation in wt.-% between the predictions and the experimental data

	(A) n=1.0	**(B) n=1.5**	**(C) n=2.0**
1,620	0.09	0.08	0.34
1,666	0.23	0.19	0.14
1,676	0.22	0.16	0.07
1,665	0.12	0.07	0.19
1,705	0.09	0.07	0.26
1,674	0.22	0.12	0.23
1,659	0.21	0.15	0.08
1,625	0.26	0.18	0.10
1,617	0.24	0.19	0.11
Average	**0.19**	**0.13**	**0.17**

Instead of calculating linearized data points from the experimental values, it is also possible to apply a non-linear fitting algorithm to the concentration course directly. Figure 69 shows the according plot with the measured values in the form of points and the fitted models in:

- green for model A,
- blue for model B,
- red for model C
- and yellow for model D

The absolute deviation in Figure 69 is visibly lower compared to Figure 68, especially for model D.

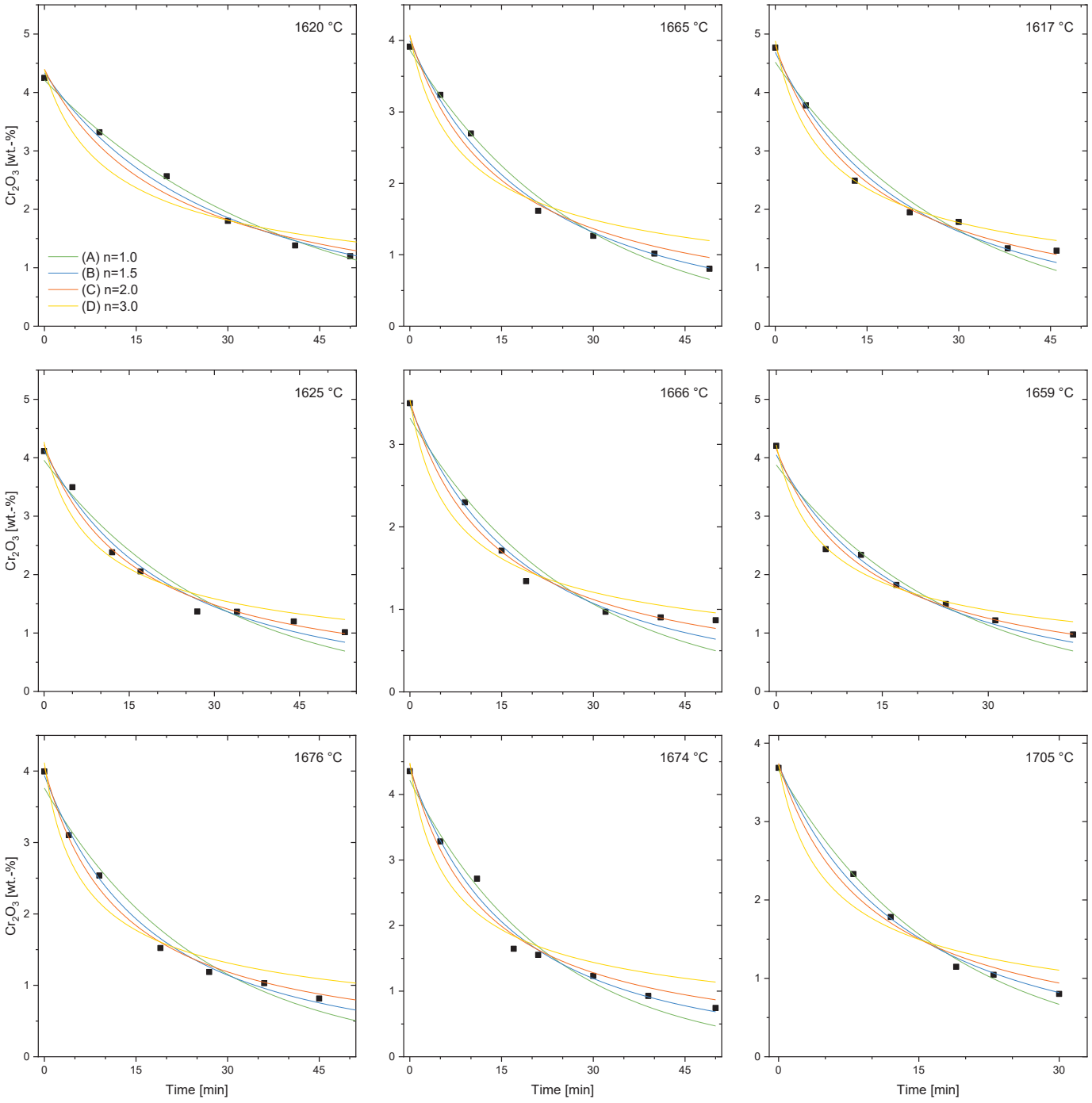

Figure 69: Applying different kinetic models to the experimental data with a non-linear fitting algorithm

Similar to the results of the linear fitting, it is not possible to define the best fitting model via a visual assessment. Therefore, as a first step, the relative deviation was calculated for all models and experiments. Table 12 summarizes the results. The outcome is comparable with that of the linearized fitting; however, the relative deviations are slightly higher for models A and C, but the ranking of the tested models stays the same.

Table 12: Mean relative deviation between the predictions from non-linear fitting and the experimental data

	(A) n=1.0	**(B) n=1.5**	**(C) n=2.0**	**(D) n=3.0**
1,620	5.1 %	4.6 %	10.6 %	20.4 %
1,666	14.9 %	9.0 %	6.0 %	11.2 %
1,676	14.8 %	7.0 %	4.1 %	16.9 %
1,665	6.5 %	3.2 %	8.9 %	19.4 %
1,705	5.8 %	3.7 %	9.3 %	17.0 %
1,674	12.9 %	5.4 %	9.1 %	20.4 %
1,659	11.0 %	6.9 %	3.6 %	7.8 %
1,625	13.5 %	8.4 %	4.5 %	11.2 %
1,617	10.6 %	6.3 %	4.4 %	7.3 %
Average	**10.6 %**	**6.1 %**	**6.7 %**	**14.6 %**

In contrast, the absolute deviations shown in Table 13 are significantly lower, which is why the non-linear fitting gives a visually better description of the experimental analyses. Model B once again gives the most accurate description of the concentration course, although the difference from model C is small. Both models can be used to represent the concentration course in the investigated concentration range for chromium oxide.

Table 13: Mean absolute deviation in wt.-% between the predictions from the non-linear fitting and the experimental data

	(A) n=1.0	**(B) n=1.5**	**(C) n=2.0**	**(D) n=3.0**
1,620	0.07	0.08	0.16	0.30
1,666	0.18	0.10	0.08	0.15
1,676	0.18	0.08	0.07	0.22
1,665	0.08	0.07	0.15	0.29
1,705	0.06	0.06	0.13	0.22
1,674	0.17	0.09	0.15	0.29
1,659	0.20	0.13	0.08	0.12
1,625	0.21	0.13	0.09	0.20
1,617	0.21	0.12	0.09	0.15
Average	**0.15**	**0.10**	**0.11**	**0.22**

The evaluation to find the best fitting kinetic model suggests using model B to explain the concentration course of chromium. Additionally, the temperature dependence on the kinetics has to be described mathematically. The correlation between the rate constant and the

temperature follows the Arrhenius law (Equation 6.14). A detailed description can be found in Chapter 6.1. The Arrhenius equation can be transformed into a linear form, as shown in Formula 7.7. This equation enables the determination of the activation energy and the pre-exponential coefficient via linear regression.

$$\ln k = \ln A - \frac{E_A}{R}\frac{1}{T} \qquad 7.7$$

Each trial provides a pair of values for the temperature and the rate constant. According to Equation 7.7, plotting $\ln k$ versus $\frac{1}{T}$ results in a pair of values that have a linear relation. Figure 70 displays the according Arrhenius plots for the data from the linear fitting (Figure 70a) and the non-linear fitting (Figure 70b). The activation energy results in similar values for both variants. The linear regressions give 217.8 ± 31.6 kJ/mol and the non-linear fitting 232.2 ± 28.4 kJ/mol. Comparing these values with the thermogravimetric investigations, the isoconversional Friedman method in Chapter 6.5 found a comparable value, especially for the later stage of the process. Other authors found comparable values with 219 kJ/mol, 256 kJ/mol, and 242 kJ/mol, although the experimental setups were different. Details can be found in the referencing literature [50,64,65].

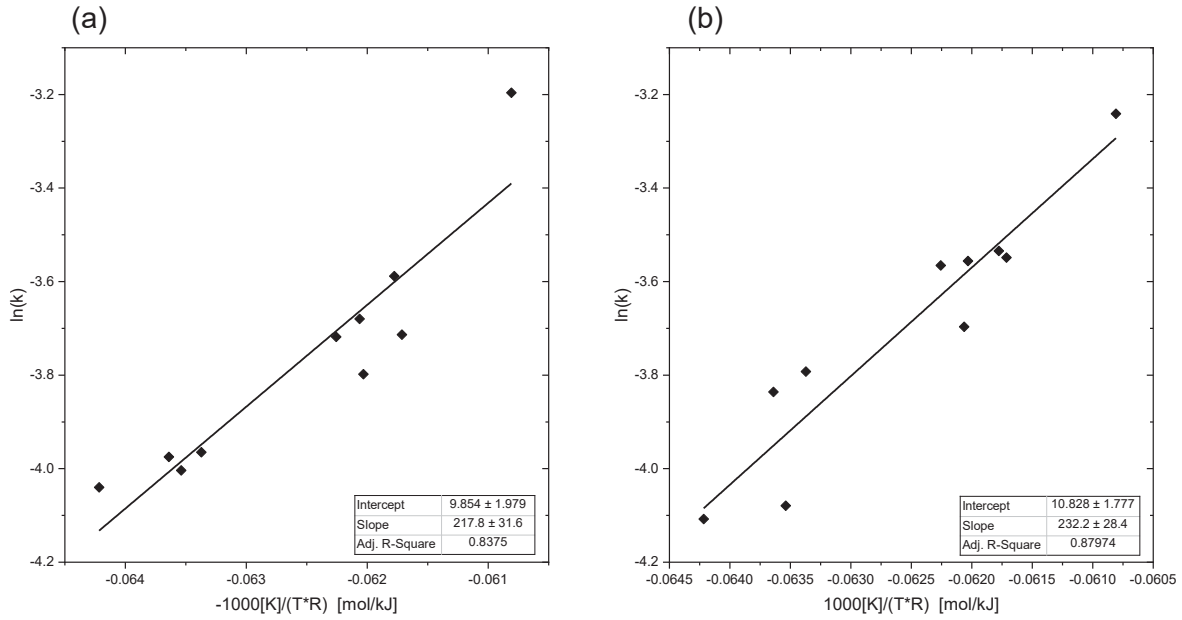

Figure 70: Arrhenius plot for model B from (a) linear and (b) non-linear fitting

After the activation energy, the pre-exponential factor and the kinetic model are determined; the kinetics of the chromium oxide reduction are described in detail for the given slag in the investigated temperature range. The next step is a comparison between calculated values from the models and the experimental data. Figure 71 visualizes this correlation. The difference between the models is minimal; the average deviation was found to be 0.146 for the model

from linear and 0.135 for the model from non-linear fitting. The models give a good description of the concentration course that was found experimentally.

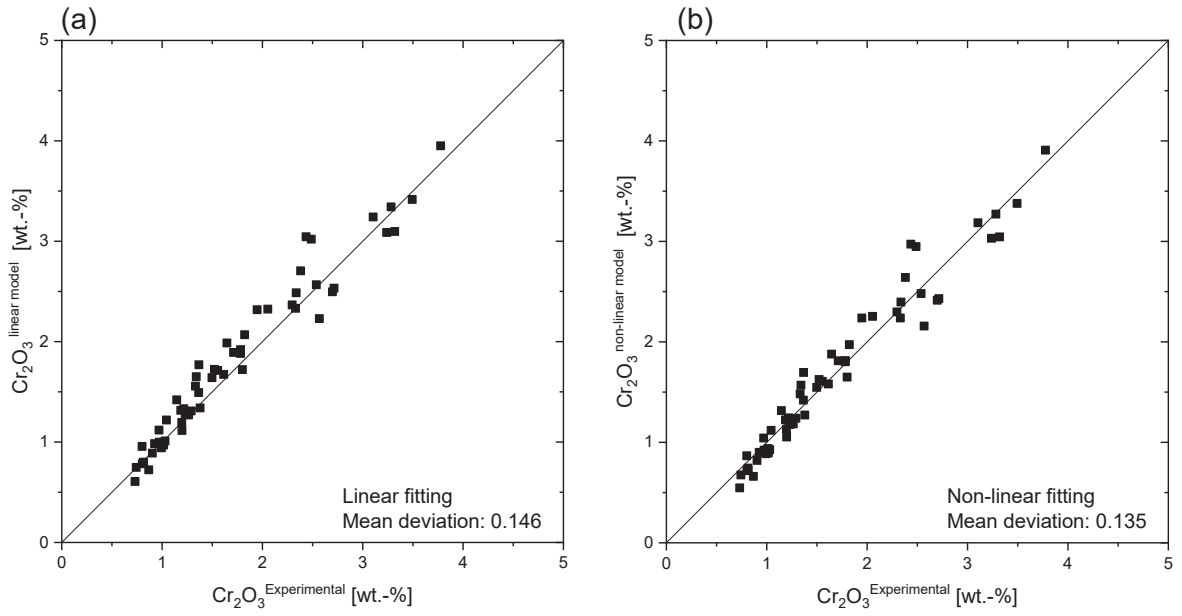

Figure 71: Comparison between predicted and experimental values for (a) linear and (b) non-linear fitting

Finally, it is possible to use the kinetic model in order to calculate the necessary treatment time for reaching a specific final concentration for a given starting concentration at a specific temperature. The transformation of the general formula for order models with respect to the necessary treatment time yields Equation 7.8. Applying model B and the Arrhenius correlation results in Equation 7.9:

$$t = \frac{\left(\frac{1}{[Cr_2O_3]_t{}^{n-1}} - \frac{1}{[Cr_2O_3]_0{}^{n-1}}\right)}{k_{(T)} \cdot (1-n)} \qquad 7.8$$

$$t = 2\frac{\left(\frac{1}{[Cr_2O_3]_t{}^{\frac{1}{2}}} - \frac{1}{[Cr_2O_3]_0{}^{\frac{1}{2}}}\right)}{A \cdot e^{-\frac{E_a}{RT}}} \qquad 7.9$$

Figure 72 visualizes Equation 7.9 in the temperature range from 1,600 °C to 1,700 °C for different starting and final chromium oxide concentrations. Figure 72a was calculated with data from linear fitting and Figure 72b with data from non-linear fitting. Both methods result in nearly the same outcome. Typical EAF slag concentrations can be found in Table 3. They lie roughly between 2 % and 4 %, which is why these values are used as starting concentrations. Additionally, an initial value of 8 % is included in order to illustrate its influence on the necessary treatment time. The final chromium concentration is set to 1.00 %, 0.50 % and

0.36 %. The first two values were used in order to visualize their influence on the necessary treatment time and the good database; the third one because it represents the Austrian legal limit of chromium in the solid slag for road construction applications. However, 0.36 % was never reached during the tests, which is why they have to be seen as an extrapolation that may include uncertainties.

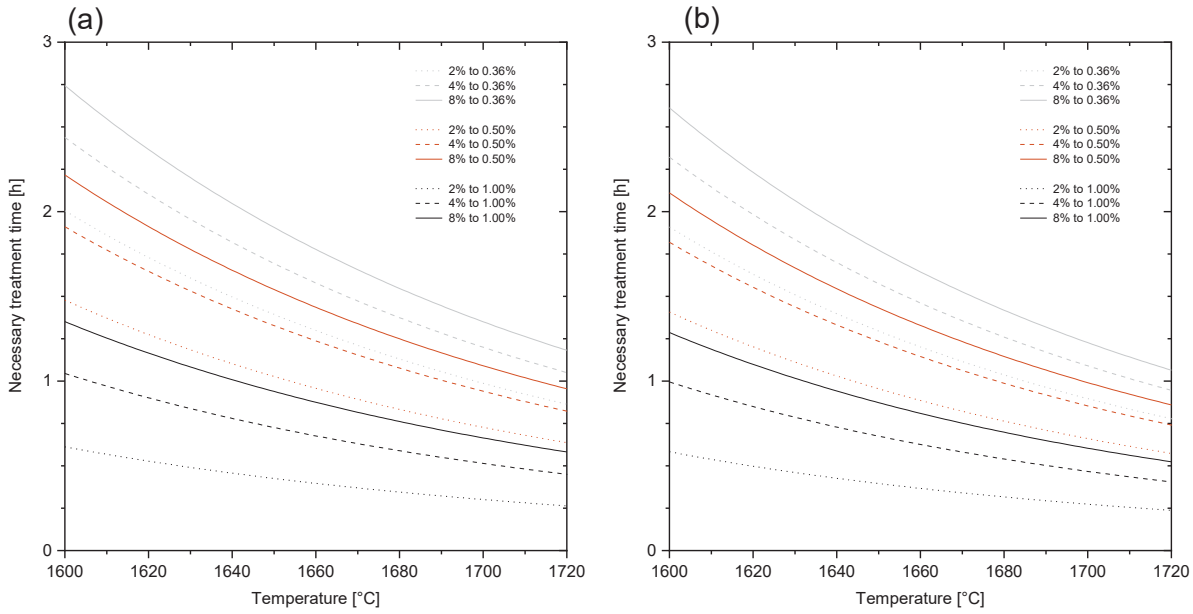

Figure 72: Calculated necessary treatment times depending on the temperature, starting and final chromium oxide concentration in the slag: (a) data from linear and (b) data from non-linear fitting

In contrast to the initial value, the final concentration has a significantly higher influence on the necessary treatment time. The influence of the concentrations decreases substantially at higher process temperatures. Both the temperature and the chromium oxide concentration at the beginning and especially at the end are important parameters. If low final values are required, high process temperatures are mandatory in order to decrease the necessary treatment time.

7.3.2 Summary of the Slag Reduction Kinetics

The campaign performed was the reason why proper temperature control had to be implemented in order to have defined conditions for the experiments. This represents a fundamental requirement to receive representative results. The evaluation was executed with linearized data followed by linear regression and non-linear fitting. While the linear regression results in a lower relative error, the non-linear fitting gives a lower absolute deviation. Since the analyses were performed with an EDX that produces a higher relative error at lower concentrations, the application of the non-linear fitting method is preferable.

The evaluation of the campaign resulted in the determination of a proper kinetic model in which the reaction rate is only influenced by the chromium oxide concentration and the temperature.

Additionally, the activation energy was estimated by using the Arrhenius correlation of the rate constant. Its value was found to be similar to the values found by other authors.

7.4 Kinetics for the Reduction of Chromium Oxide using a Residue Mixture

The previous chapter described the investigation of the kinetics of the chromium oxide reduction for slag. Since the slag contains only a few reducible compounds, pig iron was used as a collector. Chapter 4 describes other residues generated during the stainless steel production. The characterization trials indicate that the simultaneous processing of various materials can help to improve the economic feasibility because the amount of ferroalloy produced can be increased. Additionally, it gives the opportunity to minimize some negative properties of the individual residues. Furthermore, it eliminates the need for a collector metal. For these reasons, the present chapter studies the kinetics of the chromium oxide reduction when the feed material consists not only of slag, but also of dust, mill scale and grinding residue. The experimental setup stays the same, as already described in the preceding chapter. The adapted input mixture is listed in Table 14. The mixing ratio roughly follows the ratio at which the residues arise.

Table 14: Feed material for the chromium oxide's kinetical investigation using a residue mixture

Slag	5,000 g
Dust	500 g
Mill scale	500 g
Grinding residue	500 g
Foundry sand	50 g

The campaign aims to examine the correlation between the treatment temperature and the necessary treatment time. This requires at least 3 trials at different temperatures. The desired range is between 1,600 °C and 1,700 °C. Table 15 describes the nomenclature and the measurement temperature before each tapping.

Table 15: Nomenclature of the performed tests

Identifier	Measured temperature
X	1,598 °C
Y	1,652 °C
Z	1,712 °C

Figure 73 summarizes the concentration courses of the reducible compounds. Besides chromium oxide and manganese oxide, the feed material mixture also contains a notable concentration of iron oxide. In Figure 73a, the concentration course of iron oxide is only slightly influenced by the temperature. The concentration drops rapidly within the first minutes, followed by a slow decrease for the remaining treatment. The higher the temperature, the faster the concentration reaches its bottom limit. In contrast, the concentration course of chromium oxide in Figure 73b shows a higher dependency on the temperature. The reaction rate of the chromium oxide reduction decreases at lower concentrations. Finally, the concentration course of manganese oxide in Figure 73c shows a steady decrease during the reduction treatment. Since the slope of the concentration course stays the same, the reaction rate seems to only be influenced by the treatment temperature and not by the concentration of manganese oxide. This behavior may be caused by overlapping reactions that include iron and chromium. Generally, the manganese oxide reduction speed is slow compared to the others.

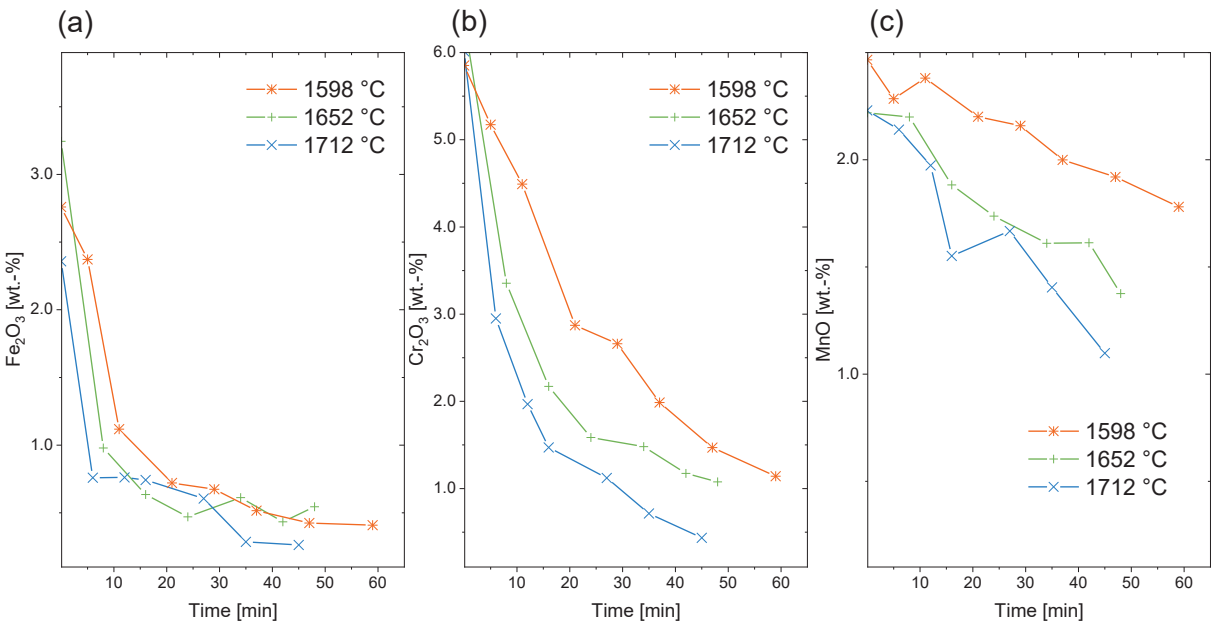

Figure 73: Concentration course for (a) iron oxide, (b) chromium oxide and (c) manganese oxide.

The EAF dust used contains 14.8 % of zinc in form of zinc oxide and zinc ferrite. Vaporization of zinc was observable during the first 10 to 15 minutes for each experiment. However, the detection of zinc in the slag samples was difficult, which is why quantitative values are not included. Its concentration was lower than the detection limit in most analyses. A possible explanation is that zinc vaporizes out of the slag during the sample collection procedure or it does not dissolve homogeneously in the slag. Considering the mixing ratio for the input material, the zinc oxide concentration in the feed material is low, so its influence on the reduction kinetics of other compounds is assumed to be small.

Evaluation of the Kinetics

The evaluation procedure to determine an appropriate kinetic model is similar to that in Chapter 7.3.1. The first step was the calculation of a pair of values regarding time and concentration for the linearized kinetic models from Equations 7.4 and 7.5. Figure 74a-c visualizes the results of these calculations and shows the fitted lines. The slope represents the rate constant for the specific model. Since the starting concentration does not lie on the line, it has to be calculated from the intercept of the fitting. This data was used to draw the model predictions in Figure 74d-f. A visual evaluation makes clear that model A gives a good description of the trial at 1,598 °C but a bad one for the others. In contrast, model B shows a good correlation with all data points except for the first one in the trial at 1,652 °C. Model C overestimates the starting chromium concentration for the trial at 1,598 °C and 1,712 °C, but gives an apt depiction of the course for the trial at 1,652 °C. Finally, model D seems to fit poorly to the experimental data, which is why no further evaluation was done.

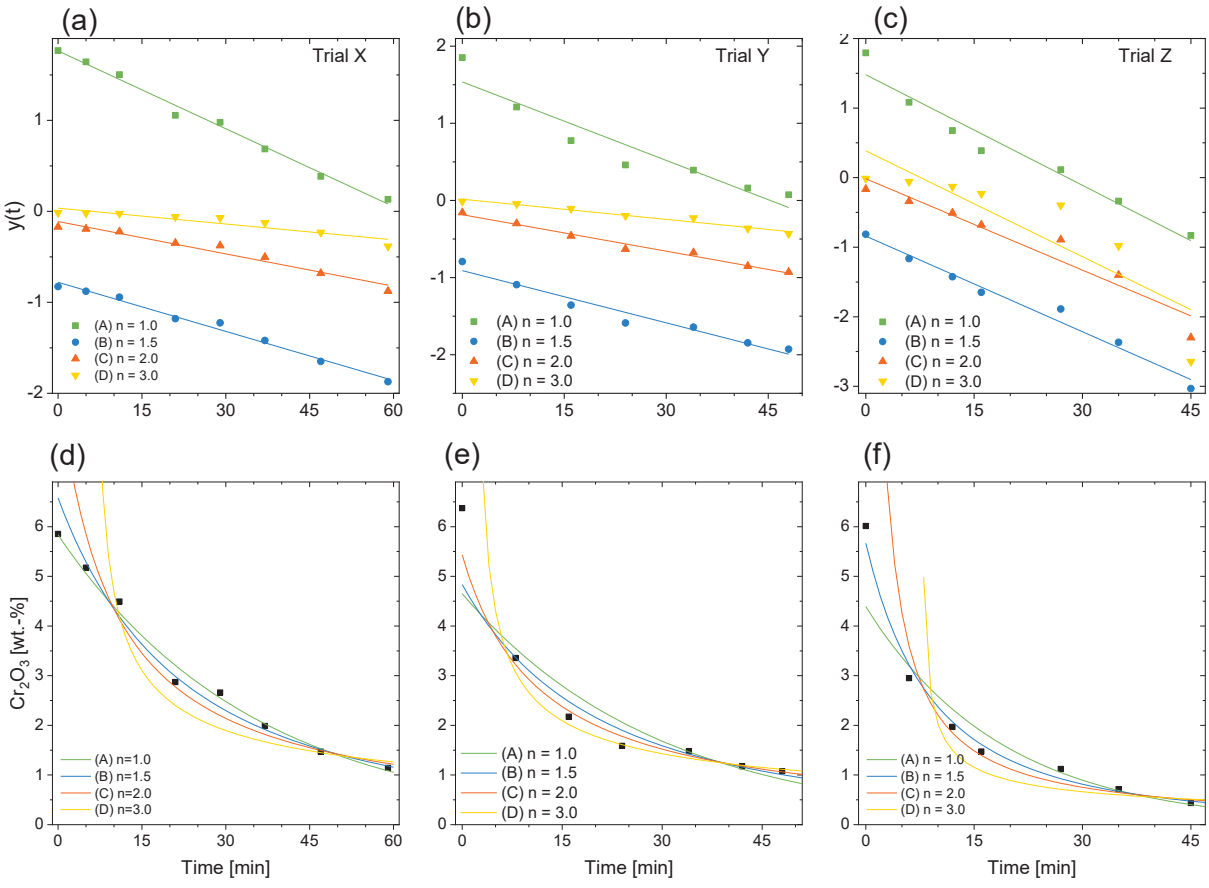

Figure 74: Testing of kinetic models using linear regression (a)-(c) and (d)-(f)

In order to rank the models, the relative and absolute deviations between the predictions and experimental data were calculated following Equation 7.6. Table 16 lists the results. The average deviation is 11.3 % for model A, 8.3 % for B and 10.3 % for C. An important note relates to the calculation of the mean deviation for model C. Looking at the graph in Figure 74f,

model C predicts a much higher starting concentration. While the experimental data gives a value of 6 %, the model predicts 64.3 %. This huge gap demonstrates the problem that arises from the linearization of the experimental data. If this data point is ignored, model C has an average deviation of 10.3 %.

Table 16: Mean relative deviation between predicted and experimental values (from linear fitting)

Trial	(A) n=1.0	(B) n=1.5	(C) n=2.0
X $_{(1,608\ °C)}$	4.3 %	5.8 %	14.2 %
Y $_{(1,647\ °C)}$	15.4 %	10.0 %	6.4 %
Z $_{(1,702\ °C)}$	14.1 %	8.9 %	150.4 % (10.2 %)
Average	**11.3 %**	**8.3 %**	**57.0 % (10.3 %)**

Table 17 lists the mean absolute deviation between the predicted and experimental values for each trial. The tendency when comparing the absolute deviations is the same as for the relative deviations. Model B gives the best description when using linear regression. However, the evaluation showed that the fitting of the linearized data of the kinetic model distorts the outcome when the starting chromium concentration increases. For this reason, the results are compared with the non-linear fitting approach.

Table 17: Mean absolute deviation between predicted and experimental values (from linear fitting)

Trial	(A) n=1.0	(B) n=1.5	(C) n=2.0
X $_{(1,608\ °C)}$	0.12	0.21	0.62
Y $_{(1,647\ °C)}$	0.45	0.33	0.21
Z $_{(1,702\ °C)}$	0.39	0.16	8.50 (0.21)
Average	**0.32**	**0.24**	**3.11 (0.35)**

The non-linear fitting approach displayed in Figure 75 gives a better fit visually. The difference between the results from the linearized equations and the direct model fit is significant. In Figure 75, models B and C seem to fit accurately. Model A predicts a too fast concentration decrease in the later stage of the process for trials Y and Z. In contrast, model D overestimates the reaction rate at higher concentrations. Therefore, model D is not included in the further examination. Since a visual evaluation does not allow for the selection of the best fitting model, the deviations between the model predictions and experimental values were calculated and compared.

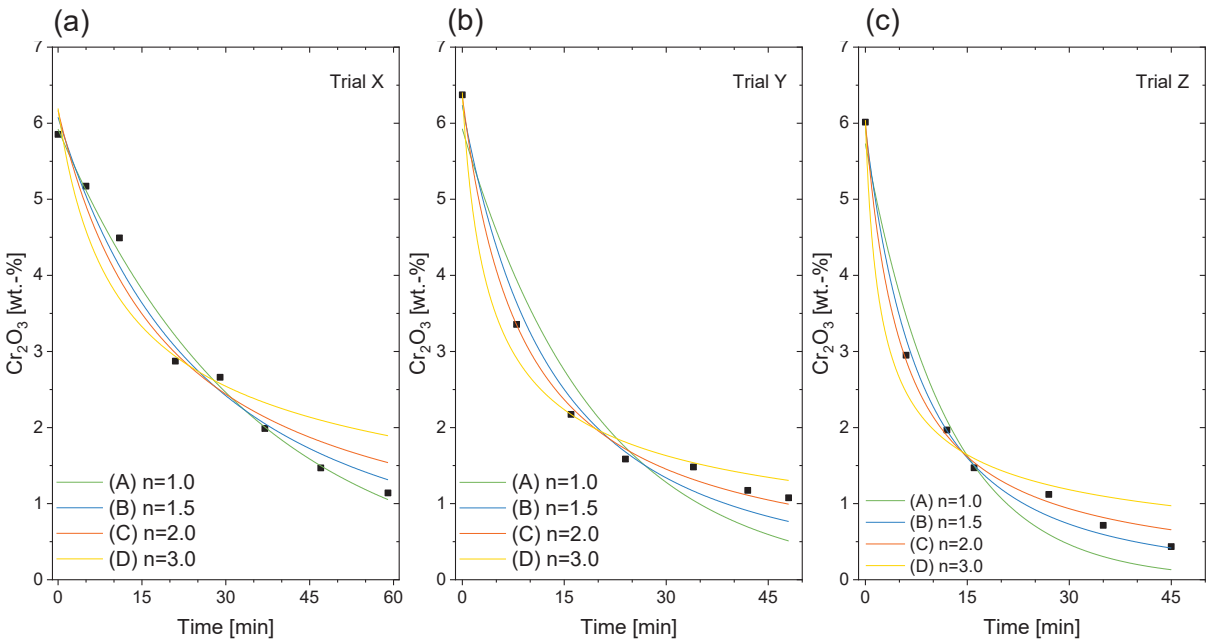

Figure 75: Non-linear model fitting

Table 18 shows the mean relative deviations for each experiment. As expected, models B and C have a significantly better fit than A. While model B gives the best description of experiments X and Z, model C yields the best description of trial Y.

Table 18: Mean relative deviation between predicted and experimental values (from non-linear fitting)

Trial	(A) n=1.0	(B) n=1.5	(C) n=2.0
X (1,608 °C)	4.2 %	7.4 %	12.3 %
Y (1,647 °C)	25.4 %	14.2 %	5.4 %
Z (1,702 °C)	33.3 %	9.4 %	14.2 %
Average	**21.0 %**	**10.3 %**	**10.6 %**

As anticipated, the relative deviations are higher when using the non-linear fitting approach but in contrast, the absolute deviations are considerably lower. Comparing model B and model C by considering the values from Table 19, model B gives the better description of trial X. On the other hand, model C fits best for trial Y. Finally, the models have the same discrepancy between the analyses and their predictions for trial Z.

Table 19: Mean absolute deviation between predicted and experimental values (from non-linear fitting)

Trial	(A) n=1.0	(B) n=1.5	(C) n=2.0
X (1,608 °C)	0.11	0.19	0.29
Y (1,647 °C)	0.44	0.23	0.08
Z (1,702 °C)	0.32	0.11	0.11
Average	**0.29**	**0.18**	**0.16**

Similar to the kinetic investigation in Chapter 7.3, models B and C portray the concentration course with comparable accuracy. Since the difference between the models is minimal, model B has been selected for further investigations in order to ensure a better comparability with the results from Chapter 7.3.

The approach that included the linearized form of the equations does not attach enough weighting to the samples with higher chromium concentrations. The prediction of the models during the first stage is inadequate when applying linear regression, which is why it is not included in the further evaluation. The Arrhenius plot in Figure 76 determines the activation energy to be 314.6 ± 31.8 kJ/mol. This is considerably higher than the activation energy found in Chapter 7.3. This deviation can be caused by the more complex reduction reactions that take place because notable iron oxide concentrations are present. Additionally, the slag composition differs slightly from the trials in 7.3. Nonetheless, the difference between the values is small.

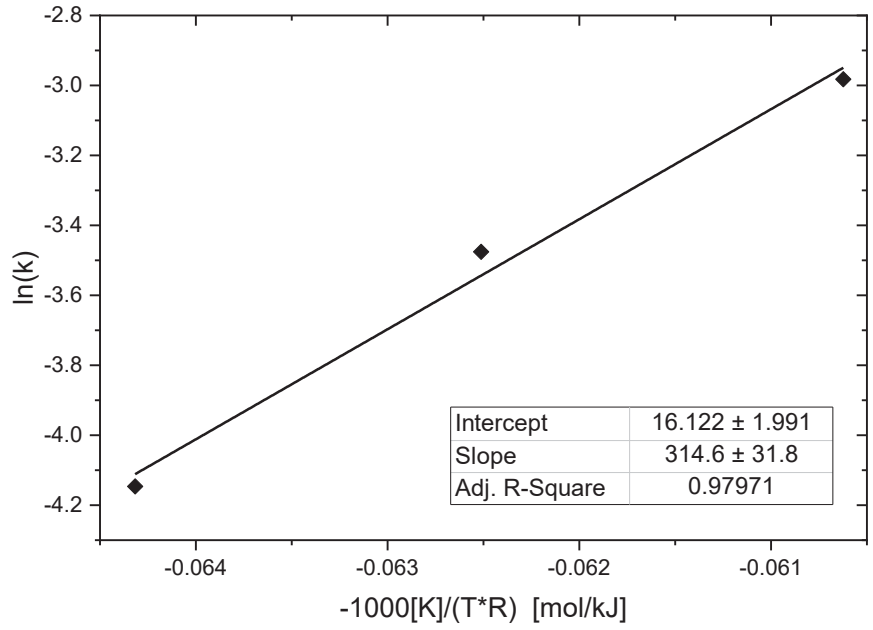

Figure 76: Arrhenius plot with the kinetic constants from the non-linear fitting

The Arrhenius plot determines the activation energy and the pre-exponential factor. These values can subsequently be used to calculate the rate constant for the kinetic model at different

temperatures. Similar to above, Figure 77a displays a diagram that depicts the necessary treatment time to reach a specific final concentration for different initial values with respect to the temperature. The model that was estimated using the residue mixture gives similar predictions to the one in Chapter 7.3. A direct comparison for the concentration course with a starting chromium oxide concentration of 8 % and a temperature of 1,650 °C can be seen in Figure 77b. The model that arises from the experiments in this chapter predicts a slightly higher reaction rate compared to the model in Chapter 7.3. Nevertheless, the difference between the models is minor.

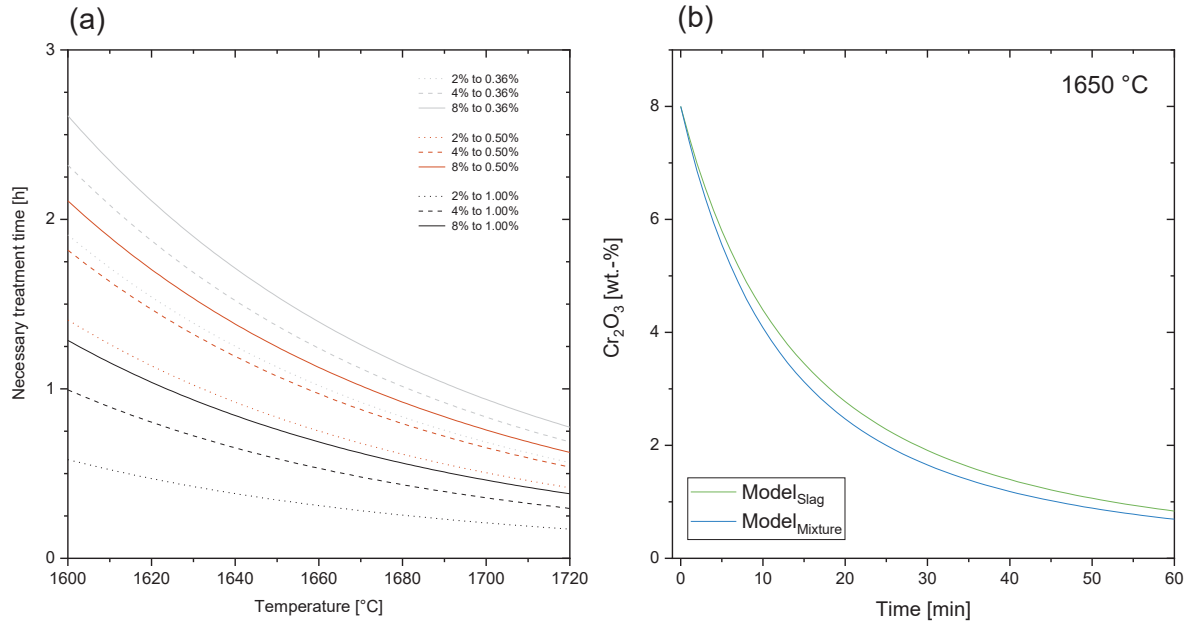

Figure 77: (a) Prediction for the necessary treatment time (b) comparison between different models

The kinetic studies resulted in a kinetic model that is capable of illustrating the concentration course of chromium oxide at the investigated temperature. The model indicates that the reaction rate decreases rapidly with lower concentrations. In order to reach a final chromium oxide concentration of 0.36 %, either a higher temperature or longer treatment time is required. The model from the slag trials is similar to the model that arises from the trials performed with a residue mixture. Since the different slag systems do not seem to have a strong influence on the kinetics, the temperature is assumed to be the major influencing parameter for the chromium reduction.

8 Electric Arc Furnace

After the successful evaluation of a kinetic model for the induction furnace trials, a scale-up in order to implement an electric arc furnace was planned. Since the Chair of Nonferrous Metallurgy did not own an electric arc furnace at the time, a new furnace was planned and built.

8.1 Planning and Construction

The planning concluded that the EAF should fit to a load of 10 kg of slag. Considering an average density of 3 g/cm³ and a maximum filling level of 50 %, the necessary volume results in 6.7 liters. The refractory lining was planned to consist of two layers:

- ramming mass for the wear lining and
- lightweight refractory bricks for thermal insulation.

The dimensions of the furnace were designed larger than required to obtain some flexibility for the ratio between diameter and height. This flexibility is required because the maximum voltage and current are limited, which is why the possible power input depends on the electrical resistance of the melt. The welding transformer GTF 1004 from Kjellberg with the following specifications was selected to be used as the power provider:

- maximum permanent current of 1000 amps
- a no-load voltage of 65 volts
- a working voltage of maximum 44 volts at 1000 amps

The furnace should be operated in resistance-heating mode. The possible power input can be calculated using Ohm's law from Equation 8.1 and the electric power law in Equation 8.2 in combination with Equation 8.3. The variables in Equation 8.3 are:

- the slag height h,
- the cross-section area of the furnace A
- and the electrical conductivity σ of the slag

$$U = I \cdot R \tag{8.1}$$

$$P = U \cdot I \tag{8.2}$$

$$R = \frac{h}{\sigma \cdot A} \tag{8.3}$$

Figure 78 gives an overview of the possible power input for different ratios between the diameter and the height of the melt. The figure indicates that such a small-scale EAF requires a relatively small ratio of diameter to height. For the same capacity, a larger diameter results

in a lower height. The area where the current flows increases while the length decreases. This leads to a drop in the electric resistance of the system, and consequently, when applying the transformer's maximum voltage, the current would exceed the allowed maximum. Hence, the exact dimensions of the lining have to be adjusted depending on the heated slag system.

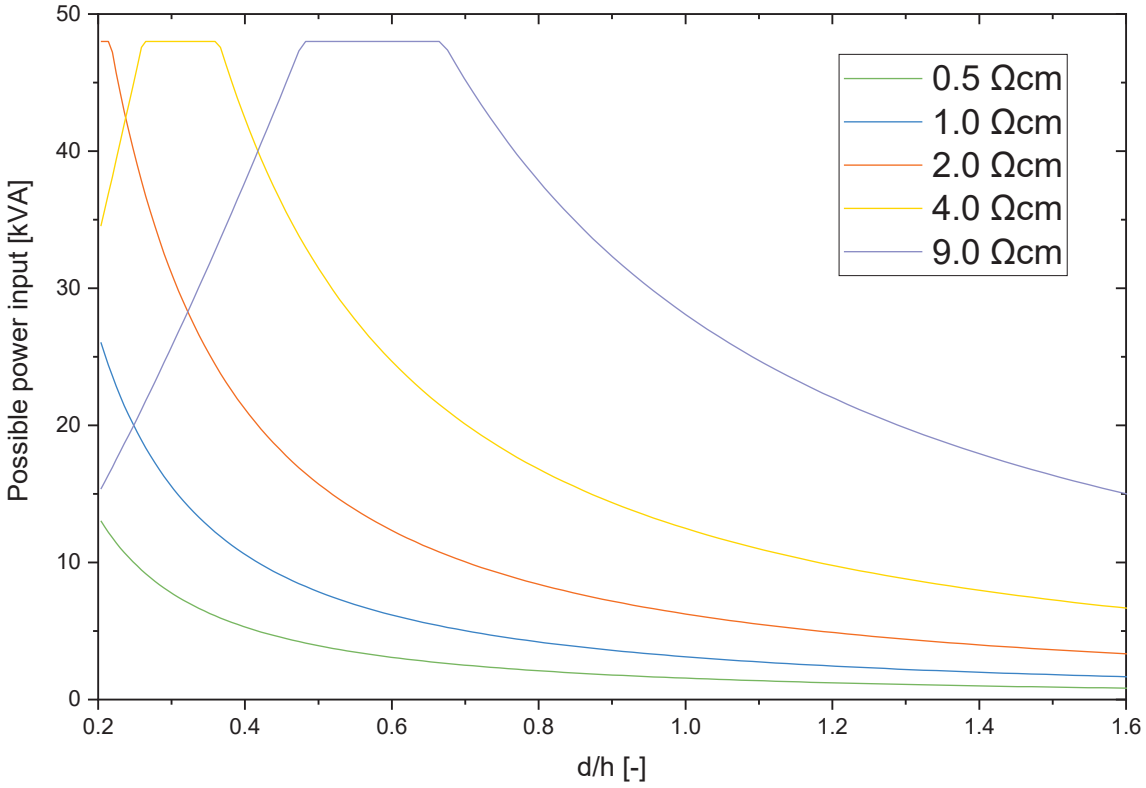

Figure 78: Maximum possible power input with respect to the ratio between diameter and height for different specific resistances

The furnace vessel was planned to have the following dimensions:

- outer diameter: 506 mm
- thickness: 10 mm
- height: 350 mm

The cover of the vessel had an opening to connect it to the existing off-gas system. This ensures that all dust and process gases are sucked away into the off-gas system. The furnace vessel is mounted on bearings in order to have a possibility to tilt the furnace for the tapping procedure. The electrode is mounted on a modified core drilling rig that is equipped with a DC motor. The material of the bottom electrode was chosen to be stainless steel due to its low thermal conductivity. This prevents the outer part of the electrode from getting hot, which would damage the insulation of the connected copper. Generally, the top electrode is connected to the minus and the bottom electrode to the plus pole of the transformer. A schematic picture of the whole furnace is shown in Figure 79.

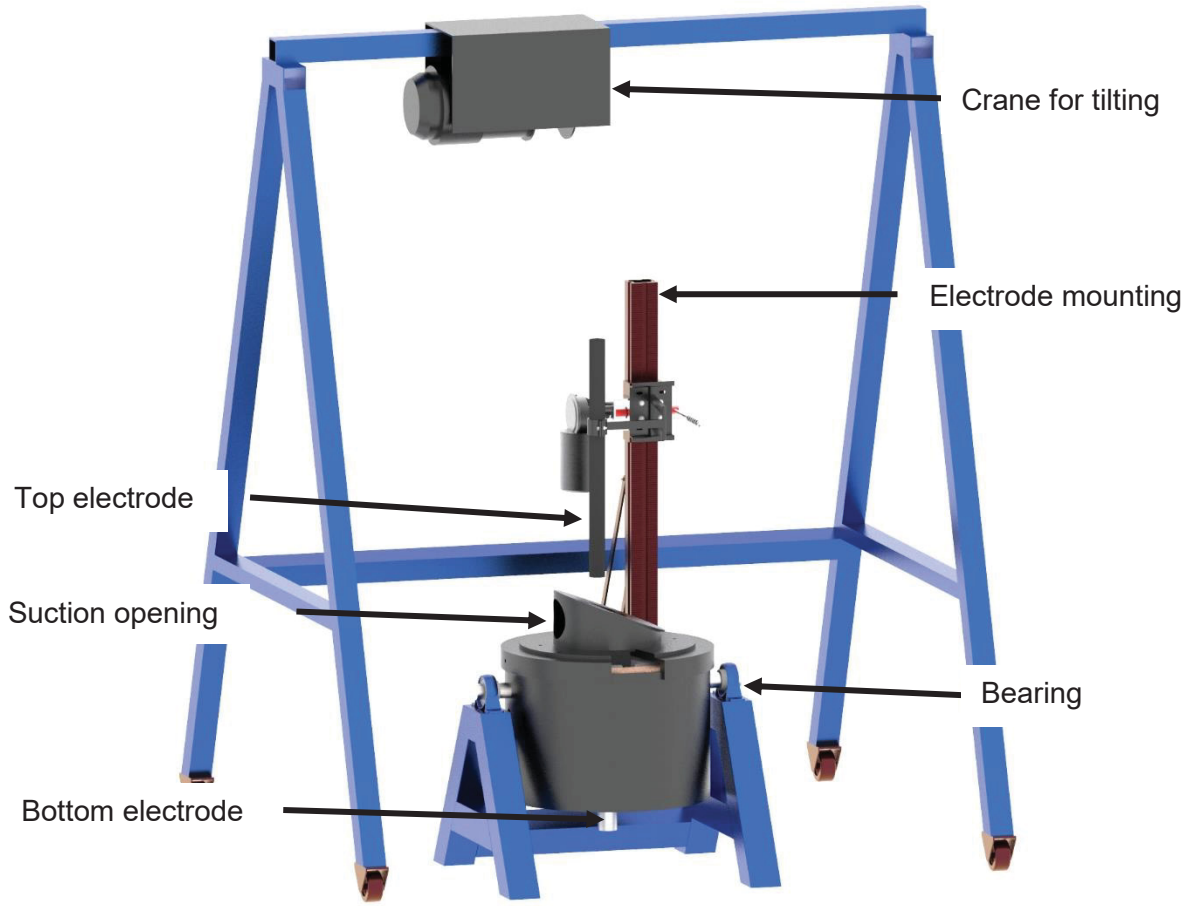

Figure 79: Schematic illustration of the furnace

8.2 Preheating System

In order to preheat the furnace for a lower temperature gradient between the melt and the refractory, a preheating system was constructed. The requirements were:

- control of the temperature
- possible wear lining temperature of at least 1,000 °C
- easy installation and removal

The easiest solution found was the use of Kanthal wire as the heating source. The selected Kanthal A1 is a ferritic iron-chromium-aluminum alloy with 20.5 to 23.5 % chromium and 5.8 % aluminum. It can be used for temperatures up to 1,400 °C. The standard power socket gives 230 V AC and a maximum current output of 16 amps. This leads to a maximum power of 3.6 kVA when the electrical circuit has a resistance of 14.4 Ω. A lower resistance leads to more than 16 amps and therefore, results in an overload of the power socket. In order to have some tolerance, the heating system was designed to have a resistance of 16 Ω. This leads to a current of 14.4 amps and maximum electrical power of 3.3 kVA. The chosen heating wire has a diameter of 1 mm with a nominative electrical resistivity of 1.8 Ω /m, so the length of the wire had to be 8.9 meters. The wire was then coiled on a lightweight refractory brick. In order to

prevent the brick from tensile stress when it is removed after the preheating, a stainless steel threaded rod was used to bind the refractory brick. Figure 80 displays the preheating system.

Figure 80: Preheating system for the EAF

Figure 81 portrays the temperature distribution during the preheating phase. It displays the temperature in the oven chamber, the temperature between the ramming mass and lightweight refractory bricks and the hull temperature. An interesting fact is that the time to reach a steady state seems to be only slightly influenced by the temperature in the furnace. When running the preheating system at full power, a temperature of approximately 950 °C can be reached after roughly 10 hours. The outside of the furnace reaches 113 °C for an oven chamber temperature of 400 °C and 190 °C for 950 °C. Figure 82 shows a comparison of the measured values with a model that was simulated by using HSC 8. The measurement does not include information from the bottom or top of the furnace. The heat flow calculation presumes a cylinder. Most of the material data required to calculate the heat flow through the lining is included in the HSC 8 database. Additionally, the datasheets of the ramming mass and isolation bricks used explain their thermal conductivity. The outside was painted black, which is why the emission coefficient of the hull was assumed to be one. Although the calculated and measured values do not conform, the heat flow model gives a good description of the temperature distribution in the furnace. The calculation results in a heat flow of 2.3 kW for a temperature of 950 °C in the oven chamber. This value does not consider heat losses through the bottom and top of the furnace. It is in good agreement with the 3.3 kW offered by the preheating device.

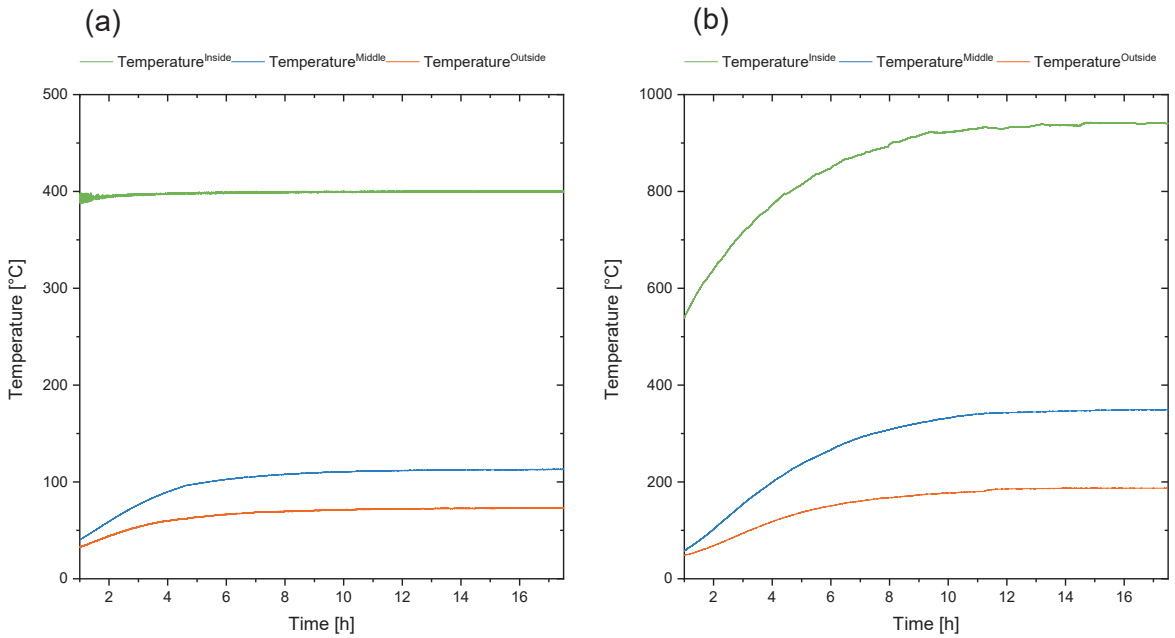

Figure 81: Temperature distribution during the preheating phase

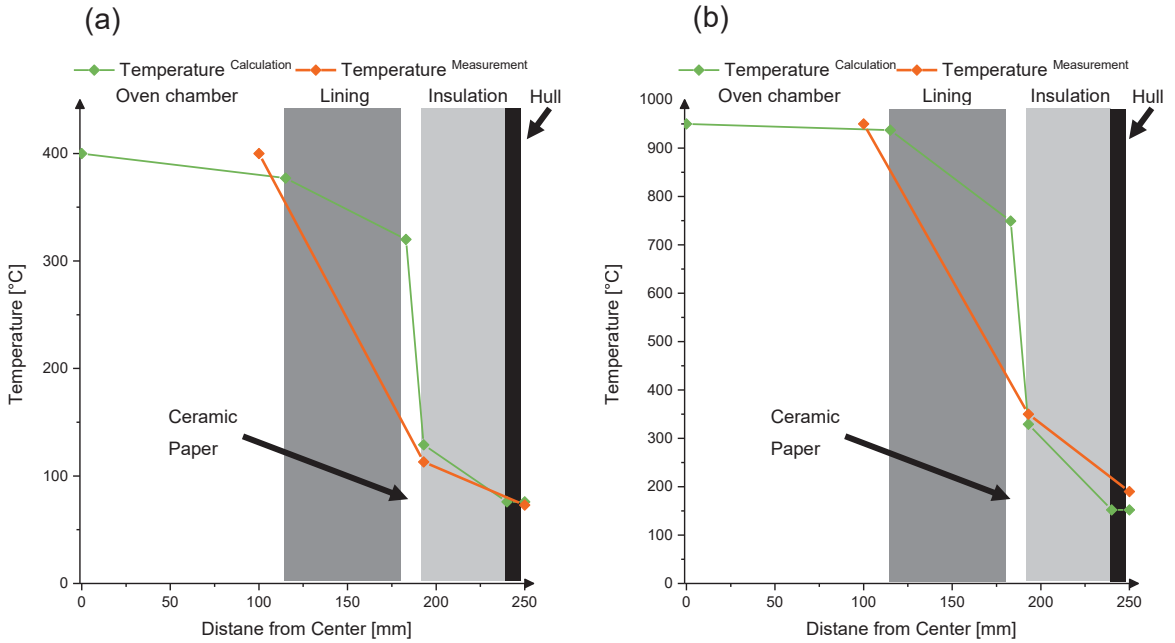

Figure 82: Comparison of the measured temperature distribution with a model that was calculated using HSC 8 for (a) 400 °C and (b) 950 °C

8.3 Test Trial

A test trial was performed in order to evaluate if the reduction behavior is comparable to one of the induction furnace trials. To do this, a ramming mass “Permasit DGO” from RHI Magnesita was used for the wear lining and a graphitic ramming paste “RST 16” from the SGL Group was used to cover the bottom electrode and protect it from the melt.

Before the slag was fed into the furnace, some carbon pieces were placed on the graphitic ramming mass. Then the graphite electrode was lowered in order to close the electrical circuit. As soon as the electrode comes into contact with the carbon pieces, the electrical circuit is closed and an electric arc forms. Then, 10 kg of slag were fed into the furnace. After 40 minutes, the slag was fully liquefied. After that, 1 kg of pig iron granules was fed to work as a collector for the chromium oxide. This was also set as the starting point of the experiment. During the following 70 minutes, 10 slag samples were taken. The sampling was performed via inserting a cold steel rod into the melt, forcing some liquid slag to solidify on the rod. The samples were analyzed with the SEM-EDX. Additionally, the temperature was measured with a thermal probe. However, the high temperature gradient in the furnace made it difficult to obtain reproducible results.

During the first half of the experiment, some slag foaming – caused by the formation of carbon monoxide due to the reduction of chromium oxide – was detectable. The formation of a thin solid slag layer was observable. This is caused by thermal radiation in combination with the lowered thermal conductivity of the foamed slag. Figure 83 shows a picture of the oven chamber during the treatment.

Figure 83: Inside the EAF showing a small solid layer at the top of the melt

After 110 minutes, the melt was tapped into a mold. At the beginning of the tapping, the slag dominated because of its lower density. Just before the furnace was empty, some metal was detectable in the flowing melt. After cooling, a good separation between the metal and slag phases was observable. It was possible to separate the phases by hammer blows to weigh them subsequently. The mass balance of the trial is shown in Figure 84a. The values of the reduction agent and off-gas are calculated because their measurement is difficult. The reduction reactions decrease the slag amount by 0.4 kg or 4 %, which is comparable to the

3 % that were found in the characterization trial in Chapter 4. The slag was crushed in a jaw crusher. The high cooling rates caused by the small-scale trial led to a dense slag, displayed in Figure 84b.

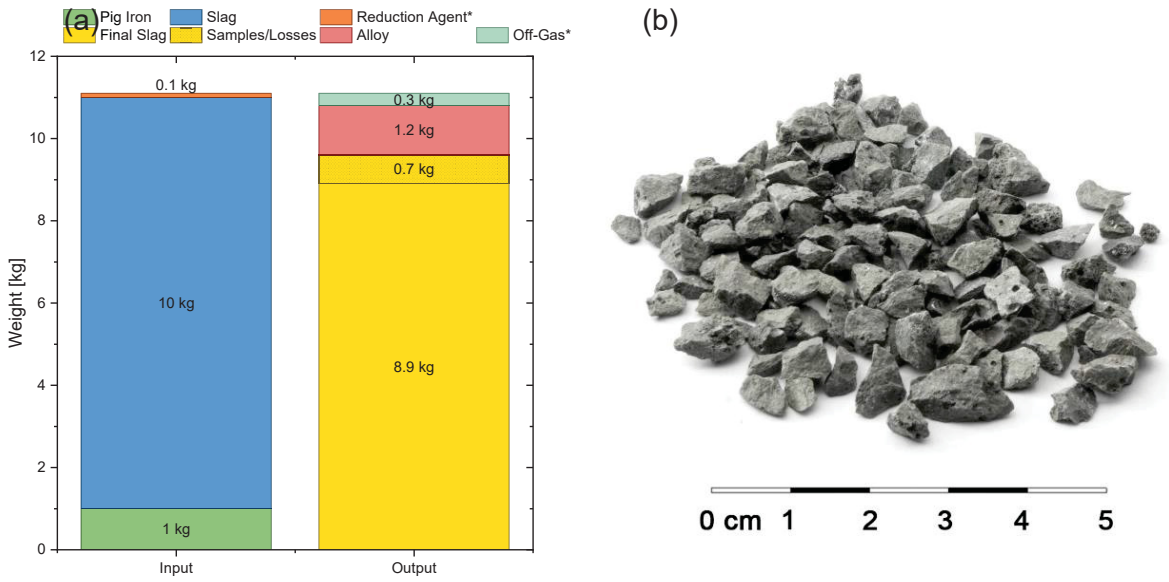

Figure 84: (a) Mass balance and (b) picture of the crushed slag

The concentration course of the major slag building compounds can be seen in Figure 85. Their overall concentration increases during the process because chromium, manganese and iron oxide are reduced out of the slag to form a metal phase. The ratio between the slag-building compounds is stable, which indicates that dissolution of the refractory lining is not observable.

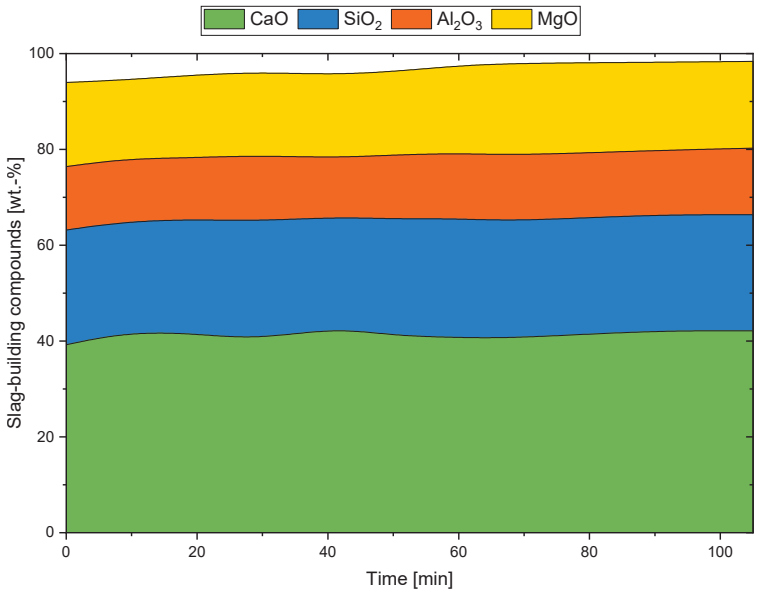

Figure 85: Concentration course of the slag-building compounds

Figure 86 provides an overview of the concentration course for chromium, iron and manganese oxide. The measured temperatures are also displayed. As mentioned above, the temperature measurement was difficult because of the high temperature gradient in the furnace. The iron oxide concentration starts at 0.75 % and decreases steadily until it reaches 0.31 % after 105 minutes. The higher iron and manganese oxide concentration in the fifth sample is most probably caused by a metal inclusion. The manganese oxide concentration is in the range between 1.8 and 2.1 % during the first 50 minutes, after which a constant decrease is observable until it reaches 1.0 % after 105 minutes. The chromium oxide concentration shows a decline for the first four samples. Then, its concentration stays nearly the same until it decreases again. The slower reduction rate after 30 minutes is likely caused by the measured temperature drop. Finally, the reduction reaction seems to be very slow for the last three samples, with a final value of 0.32 % for the chromium oxide. This is slightly lower than Austria's legislative limit (0.36 %) for road construction purposes.

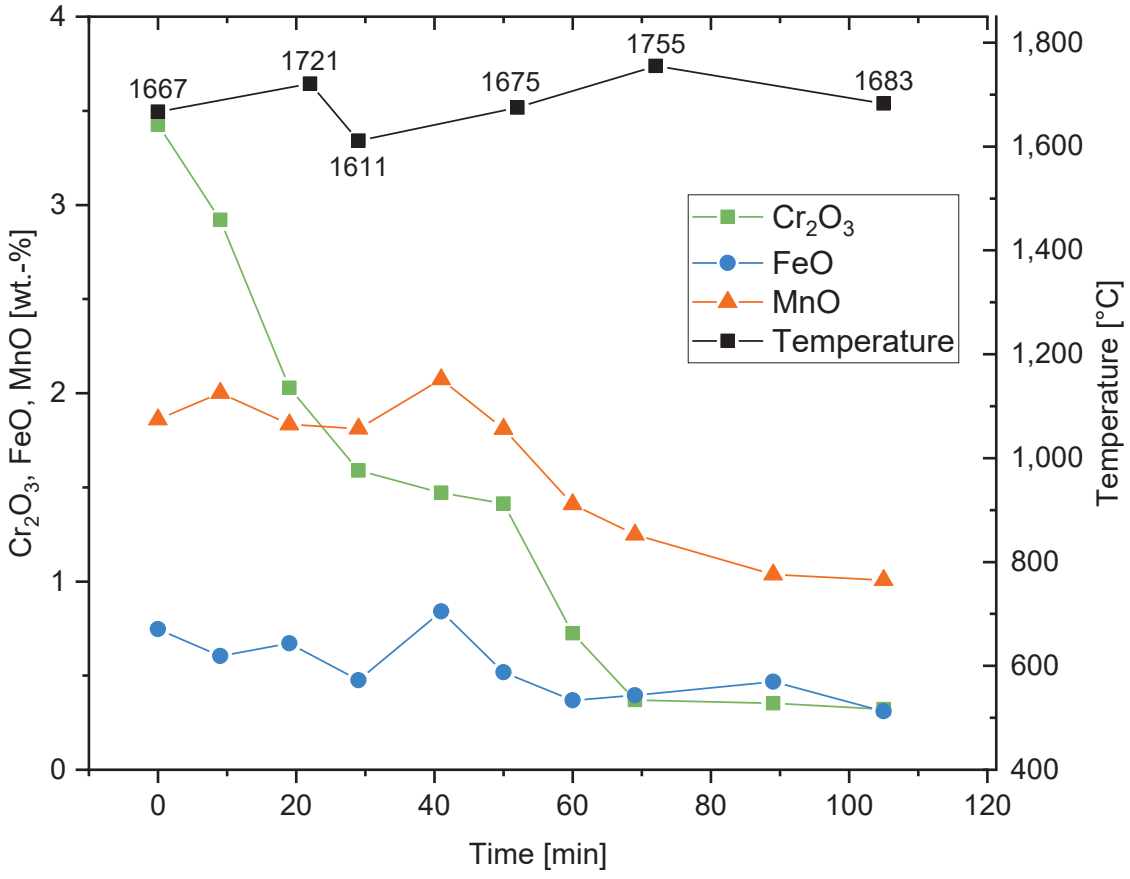

Figure 86: Temperature and concentration course of reducible compounds

The evaluation of the trial shows that the mass flow found in the EAF is comparable to that found in the characterization trials. The same can be said for the concentration courses of the slag-building and reducible compounds. The final chromium concentration in the slag is lower than the legal limit to apply steelwork slag for road construction purposes. The chromium concentration during the later stage of the process seems to be steady. This indicates that an

equilibrium state was reached. In order to perform a detailed evaluation in the EAF, reproducible results are mandatory. This requires a precise measurement and control of the process temperature, which, compared to the induction furnace, is more complicated because the use of a pyrometer is not possible. Furthermore, using a thermocouple is problematic due to the high corrosive properties of the investigated slag system. Further development has to focus on a possibility of overcoming these problems in order to allow for a continuous temperature measurement. Consequently, it would be achievable to implement a temperature control system in a similar way to that done for the induction furnace. Despite the high fluctuations in the slag temperature, the trial performed proves – high process temperatures and sufficient treatment time presumed – the technical feasibility of a melting reduction treatment to get final chromium oxide concentrations that are lower than the minimum required limit of 0.36 %.

9 Conclusions and Outlook

The thesis outlines the necessity of alternatives to the common landfilling of wastes from the stainless steel industry. These wastes include slags, dusts, mill scale and grinding residues. Their landfilling not only leads to costs for the disposal, but also to a raw material loss. The costs are expected to rise due to stricter environmental laws and limited space for the depositing in the surrounding areas of industrial plants. For these reasons, it is essential to significantly reduce the amount of wastes that are landfilled. A strategy is the evaluation of possible markets to reuse these materials in other industrial sectors and the development of processes that produce marketable products from wastes that cannot be recycled directly. A possible recovery process includes, for example, a pyrometallurgical treatment in order to produce a ferroalloy and a clean slag that could be applied in the construction sector. The main challenge of such a treatment is to reduce the chromium oxide concentration in the slag to meet the legal requirements.

The literature study gives an overview of the recovery concepts that have already been developed. They can be divided into pyrometallurgical, hydrometallurgical and mechanical approaches. The first part of this thesis dealt with a hydrometallurgical approach in order to recover zinc from the dust fraction. A literature study showed that most of the effort was placed into residues from carbon steel production. Different leaching methods were described. A small campaign tested the usability of ammonium chloride and sulfuric acid as leaching solutions at different temperatures and concentrations. The experiments found the fraction of zinc that is bound in zinc ferrite to be roughly 50 %. Therefore, the use of ammonium chloride or low-concentrated sulfuric acid results in low recovery rates for zinc. In contrast, using highly concentrated sulfuric acid at raised temperatures leaches 90 % of the zinc but produces a complex solution that does not only contain zinc, but also iron, chromium, nickel, manganese, copper, magnesium and aluminum. For this reason, further processing would require expensive purification steps. Finally, the main problem when considering a hydrometallurgical approach is the generation of sludges that have to be dumped again, which is in conflict with the idea of a zero waste concept.

The pyrometallurgical approach gives – compared to the hydrometallurgical and mechanical methods – more possibilities of adjusting the properties of the resulting products. This higher flexibility is the reason why it is assumed to be the most promising approach. A detailed study of the thermodynamics in respect of a reductive smelting process was done. The most important parameters were found to be the process temperature, chromium oxide activity, slag viscosity, reduction agent and liquidus temperature. While temperature and reduction agent can be adjusted easily, it is more difficult to vary the oxide activity, slag viscosity and the liquidus temperature. These properties depend on the slag composition and treatment temperature, rendering it impossible to modify them individually. An important parameter is the

basicity B_2 that is defined as the ratio of lime to silicon oxide. Higher slag basicity results in increased oxide activity and lower slag viscosity. Generally, network-forming compounds such as silicon oxide or phosphorus oxide increase the slag viscosity. Finally, the influence of the slag composition on the liquidus temperature can be calculated by the use of thermodynamic data from thermochemical database systems like FactSage.

After the evaluation of the optimum process parameters, different materials from the stainless steel industry were characterized. The thesis investigated a slag, a dust, a mill scale and a grinding residue. The characterization included chemical analyses as well as mappings to show the elemental distribution. Additionally, a reductive melting was performed to investigate the concentration course of the reducible compounds. Analyses in the hot stage microscope were used to examine the melting behavior in detail. Finally, the mass flow yielded was compared with theoretical calculations. While the slag contains a low concentration of reducible compounds and hence, generates mostly slag and only little ferroalloy, the mill scale and the grinding residue mainly consist of reducible compounds. For this reason, they can be used to increase the economic feasibility of a reductive melting process. The dust also contains zinc that evaporates to the off-gas system during the treatment and leads to the formation of a zinc-enriched dust fraction that can be captured as a third product. The hot stage microscope analyses showed that the slag has the best melting behavior, with melting points in the range between 1,420 °C and 1,450 °C. The other materials included some high melting phases at the beginning of the treatment. For that reason, the blending of different materials can improve the properties of the resulting slag phase.

The characterization trials were used to determine an optimized material mixture and create a complex mass flow model. An experiment to investigate the simultaneous recycling of the characterized residues was performed. The treatment processes generated three products – a ferroalloy, a slag and a zinc-enriched dust fraction. In order to capture the zinc-enriched dust, a bag house filter was implemented. The analyses of this dust fraction showed that it contained only few impurities. This can be explained by the conditions in the small-scale induction furnace that neither produced carry-over nor led to evaporations, as it happened in the electric arc furnace. The resulting ferroalloy contained chromium, nickel and molybdenum. The analysis of the generated slag phase detected a notable chromium oxide concentration. Since low chromium concentrations are the basic requirement for the marketability of the slag phase, a detailed investigation on the reduction kinetics of chromium oxide was planned.

Thermogravimetric analysis can be used to detect the mass development of a sample during a defined heating program. The reduction reaction of chromium oxide with carbon generates carbon monoxide, which is why the mass of the sample over time can be used to calculate the extent of conversion. The thesis gives a short overview of possible methods to evaluate the kinetic triplet – the activation energy, the pre-exponential coefficient and the reaction model –

of the chromium oxide reduction from thermogravimetric data. The application of the often-used Kissinger method found the activation energy to be 371.2 kJ/mol. An extended approach arising from the Kissinger method resulted in an activation energy of 321.9 kJ/mol. The isoconversional methods described an increase in the activation energy during the progress of the reaction. The use of so-called master plots in combination with the model fitting approach found the reaction to follow a three-dimensional diffusion model. However, the change in the activation energy with the reaction progress leads to the assumption that a transition of the rate-limiting step takes place. This transition seems to be seamless because the decrease in the activation energy is steady. Nonetheless, the data collected does not allow for a more detailed evaluation. Regardless of this incomplete evaluation, the thermogravimetric analyses can be used for a comparison with the results from experiments in the melting lab.

The following investigations in an induction furnace demonstrated that temperature control is important in order to get reproducible results. Many trials aiming to develop a solid experimental setup found the use of a pyrometer to measure the bottom temperature of a graphite crucible to be the best solution to monitor the temperature. The final step to obtain high quality data was the implementation of a self-developed PID controller that allowed for a deviation of only ± 2.5 °C. The evaluation of the experimental data was done by applying two different approaches – linear fitting for linearized data and non-linear fitting for raw data. The non-linear approach was found to be preferable, because it minimizes the absolute deviation. In contrast, the linearization lowers the accuracy of the fitting due to a distortion that arises from the logarithm function. The error increases for data points of higher concentration. The activation energy for the chromium reduction when using only slag was found to be 232 kJ/mol. A second experimental campaign with a residue mixture containing slag, dust, mill scale and grinding residue found an effective activation energy of 314 kJ/mol. The difference in the activation energy can be explained by the change in the slag system. The residue mixture contains more reducible compounds, which is why the running reactions are more complex. Iron oxide, for example, inhibits the reduction kinetics of the investigated compound because chromium can react with iron oxide to iron and chromium oxide. However, the determined models gave similar predictions regarding the concentration course of chromium oxide for the slag trials and the trials with the residue mixture. A comparison with the results from the thermogravimetric analyses shows that all determined values for the activation energy are within the same range. Finally, the induction furnace trials prove that the temperature can be seen as the major influencing parameter on the reduction kinetics. Additionally, the investigations led to the development of a solid experimental setup to investigate carbothermic reduction reactions. Further investigations should be done in order to evaluate the influence of the slag composition on the kinetics.

The final step of the pyrometallurgical part was a scale-up project to compare the induction furnace results with the results from the electric arc furnace. The thesis contains a brief outline of the construction phase and includes some calculations performed during the planning, some necessary adaptations as well as the construction of a preheating unit. The major problem in the electric arc furnace is the temperature measurement, which compared to the induction furnace is more difficult. The direct application of a thermocouple was found to be impossible because the slag damages its protective alumina mantle. The use of “Type S” thermal probes results in strongly fluctuating measurement values, caused by the high temperature gradient in the furnace. A test trial was performed and the concentration course of chromium was found to be comparable to the results from the induction furnace. Further effort has to be invested in order to develop a temperature measurement system and consequently, a PID controller. It might be possible to use a graphite hull to protect the alumina of the thermocouple. Initial trials showed that the oxidic atmosphere in the upper part of the furnace – caused by the suction – quickly oxidizes the graphite. For this reason, further considerations should focus on protective materials or on a solution to lower the oxygen activity around the graphite cover.

In summary, the melting campaigns proved that a pyrometallurgical treatment process is suitable to recycle residues from the stainless steel industry. The main challenge is that the final chromium oxide concentration in the final slag has to be lower than the legislative limit. The smelting campaigns performed indicate that the realization of such low concentrations requires long treatment times at high temperatures. The kinetic investigations give a detailed description of the influence of the temperature on the necessary treatment time. Further research can use this knowledge to estimate the required dimensions of an industrial-scale furnace. However, an industrial-scale furnace involves further challenges such as the prevention of metal droplets in the slag, which is necessary to achieve a complete separation between the slag and metal phases during the tapping. Furthermore, a measurement system to monitor the temperature in the laboratory electric arc furnace has to be implemented. Only then can further kinetic investigations be executed in order to evaluate scale-up effects on the reduction kinetics.

10 References

[1] “Global stainless steel production from 2005 to 2017,” https://www.statista.com/statistics/223028/world-stainless-steel-production/.

[2] G. Stubbe, G. Harp, D. Schmidt et al., “New technology for the recovery of chromium from EAF stainless steelmaking slag | Neue Technologie zur Chromrückgewinnung aus Elektrolichtbogenofenschlacken,” *Stahl und Eisen*, vol. 131, no. 5, pp. 45–50, 2011.

[3] Z. Huaiwei and H. Xin, “An overview for the utilization of wastes from stainless steel industries,” *Resources, Conservation and Recycling*, vol. 55, no. 8, pp. 745–754, 2011.

[4] F. López, A. López-Delgado, and N. Balcazar, “Physico-chemical and mineralogical properties of EAF and AOD Slags,” *Afinidad*, vol. 53, 1996.

[5] A. Kern, “Harsco: Warten auf positiven Bescheid,” https://www.meinbezirk.at/bruck-an-der-mur/c-wirtschaft/harsco-warten-auf-positiven-bescheid_a1226877.

[6] K. Morita, K. Tsukiashi, M. Kimura et al., “Activity of Chromium Oxide in CaO-SiO 2 based Slags at 1873 K,” *steel research international*, vol. 76, no. 4, pp. 279–283, 2005.

[7] G. Schneeberger, *Verfahrensentwicklung und Anlagenoptimierung beim Recycling von Filterstäuben aus der Eisen- und Stahlindustrie,* Doctoral Thesis, 2013.

[8] J. L. Roth, R. Frieden, T. Hansmann et al., “PRIMUS, a new process for recycling by-products and producing virgin iron,” *Revue de Métallurgie*, vol. 98, no. 11, pp. 987–996, 2001.

[9] T. Suetens, B. Klaasen, K. van Acker et al., “Comparison of electric arc furnace dust treatment technologies using exergy efficiency,” *Journal of Cleaner Production*, vol. 65, pp. 152–167, 2014.

[10] A. Fleischanderl, U. Gennari, and A. Ilie, “ZEWA – metallurgical process for treatment of residues from steel industry and other industrial sectors to generate valuable products,” *Ironmaking & Steelmaking*, vol. 31, no. 6, pp. 444–449, 2004.

[11] W. Burrows, *Zinc oxide recovery process*, Google Patents, 1974.

[12] M. Olper and M. Maccagni, “From C.Z.O. to Zinc Cathode without any Pretreatment: The EZINEX Process,” in *International Symposium on Lead and Zinc Processing Lead and Zinc 2008*, pp. 85–98.

[13] G. Diaz and D. Martin, “Modified Zincex process: The clean, safe and profitable solution to the zinc secondaries treatment,” *Resources, Conservation and Recycling*, vol. 10, 1-2, pp. 43–57, 1994.

[14] “Modified Zincex Process by Tecnicas Reunidas,” https://ddtp.tecnicasreunidas.es/wp-content/uploads/2016/11/P-ZINCEX-technology-information-II.pdf.

[15] M.K. Jha, V. Kumar, and R.J. Singh, “Review of hydrometallurgical recovery of zinc from industrial wastes,” *Resources, Conservation and Recycling*, vol. 33, no. 1, pp. 1–22, 2001.

[16] D. K. Xia, *Recovery of Zinc from Zinc Ferrite and Electric Arc Furnace Dust,* Doctoral Thesis, 1997.

[17] R. S. Kunter and W. E. Bedal, “Chloride-process treatment of smelter flue dusts,” *JOM*, vol. 44, no. 12, pp. 35–38, 1992.

[18] N. Leclerc, E. Meux, and J.-M. Lecuire, “Hydrometallurgical recovery of zinc and lead from electric arc furnace dust using mononitrilotriacetate anion and hexahydrated ferric chloride,” *Journal of hazardous materials*, vol. 91, 1-3, pp. 257–270, 2002.

[19] Z. Youcai and R. Stanforth, “Integrated hydrometallurgical process for production of zinc from electric arc furnace dust in alkaline medium,” *Journal of hazardous materials*, vol. 80, 1-3, pp. 223–240, 2000.

[20] P. W. Atkins and J. de Paula, *Atkins' physical chemistry*, Oxford University Press, Oxford, New York, 2006.

[21] Outotec Technologies, *HSC Chemistry 8*.

[22] R. F. Sebenik, A. R. Burkin, R. R. Dorfler et al., “Molybdenum and Molybdenum Compounds,” in *Ullmann’s Encyclopedia of Industrial Chemistry*, American Cancer Society, 2000.

[23] J.-f. XU, L.-j. SU, D. CHEN et al., “Experimental Investigation on Viscosity of CaO-MgO(-Al2O3)-SiO2 Slags and Solid-liquid Mixtures,” *Journal of Iron and Steel Research, International*, vol. 22, no. 12, pp. 1091–1097, 2015.

[24] Y. Xiao and L. Holappa, “Determination of Activities in Slags Containing Chromium Oxides,” *ISIJ International*, vol. 33, no. 1, pp. 66–74, 1993.

[25] A. V. Pavlov, D. Y. Ostrovskii, and Y. V. Glavatskikh, “Valence state of chromium in molten slag,” *Steel in Translation*, vol. 41, no. 3, pp. 193–196, 2011.

[26] T. Nakasuga, K. Nakashima, and K. Mori, “Recovery Rate of Chromium from Stainless Slag by Iron Melts,” *ISIJ International*, vol. 44, no. 4, pp. 665–672, 2004.

[27] Y. Xiao and L. Holappa, “Thermodynamics of Slags Containing Chromium Oxides,”.

[28] Y. Xiao, M. A. Reuter, and L. Holappa, “Oxidation state and activities of chromium oxides in CaO-SiO2-CrOx slag system,” *Metallurgical and Materials Transactions B*, vol. 33, no. 4, pp. 595–603, 2002.

[29] T. Jiang, J.-Y. Hwang, G. R. F. A. F., et al., eds., *6th International Symposium on High-Temperature Metallurgical Processing*, John Wiley & Sons, Inc, Hoboken, NJ, USA, 2015.

[30] T. SAITO, K. MARUYA, and others, “Diffusion of calcium in liquid slags,” *Science reports of the Research Institutes, Tohoku University. Ser. A, Physics, chemistry and metallurgy*, vol. 10, pp. 306–314, 1958.

[31] J.-Y. Choi, H.-G. Lee, and J.-S. Kim, “Dissolution Rate of Al2O3 into Molten CaO-SiO2-Al2O3 Slags,” *ISIJ International*, vol. 42, no. 8, pp. 852–860, 2002.

[32] M. Kekkonen, H. Oghbasilasie, and S. Louhenkilpi, “Viscosity models for molten slags,” *(None)*, 12/2012, 2012.

[33] G. Urbain, “Viscosity estimation of slags,” *Steel Research*, vol. 58, no. 3, pp. 111–116, 1987.

[34] K.C. Mills, L. Yuan, and R.T. Jones, “Estimating the physical properties of slags,” *Journal of the Southern African Institute of Mining and Metallurgy*, vol. 111, pp. 649–658, 2011.

[35] L. Forsbacka, L. Holappa, T. Iida et al., “Experimental study of viscosities of selected CaO-MgO-Al2O3-SiO2 slags and application of the Iida model,” *Scandinavian Journal of Metallurgy*, vol. 32, no. 5, pp. 273–280, 2003.

[36] K. C. Mills and S. Sridhar, “Viscosities of ironmaking and steelmaking slags,” *Ironmaking & Steelmaking*, vol. 26, no. 4, pp. 262–268, 1999.

[37] A. Kondratiev, E. Jak, and P. C. Hayes, “Predicting slag viscosities in metallurgical systems,” *JOM*, vol. 54, no. 11, pp. 41–45, 2002.

[38] G. Adegoloye, A.-L. Beaucour, S. Ortola et al., “Concretes made of EAF slag and AOD slag aggregates from stainless steel process: Mechanical properties and durability,” *Construction and Building Materials*, vol. 76, pp. 313–321, 2015.

[39] H. Shen and E. Forssberg, “An overview of recovery of metals from slags,” *Waste Management*, vol. 23, no. 10, pp. 933–949, 2003.

[40] M. Tossavainen, F. Engstrom, Q. Yang et al., “Characteristics of steel slag under different cooling conditions,” *Waste management (New York, N.Y.)*, vol. 27, no. 10, pp. 1335–1344, 2007.

[41] B. Adamczyk, R. Brenneis, C. Adam et al., “Recovery of Chromium from AOD-Converter Slags,” *steel research international*, vol. 81, no. 12, pp. 1078–1083, 2010.

[42] Q. Yang, F. Engström, M. Tossavainen et al., “Treatments of AOD Slag to enhance recycling and resource conservation,” SweMin, 2005.

[43] G. Ma and A. M. Garbers-Craig, “Stabilisation of Cr(VI) in stainless steel plant dust through sintering using silica-rich clay,” *Journal of hazardous materials*, vol. 169, 1-3, pp. 210–216, 2009.

[44] M. I. Domínguez, F. Romero-Sarria, M. A. Centeno et al., “Physicochemical characterization and use of wastes from stainless steel mill,” *Environmental Progress & Sustainable Energy*, vol. 29, no. 4, pp. 471–480, 2010.

[45] T. Sofilić, A. Rastovcan-Mioc, S. Cerjan-Stefanović et al., *Characterization of steel mill electric-arc furnace dust*: *4th WSEAS International Conference on Waste Management, Water Pollution, Air Pollution, Indoor Climate (WWAI '10) : Kantaoui, Sousse, Tunisia*, WSEAS Press, [S.l.], 2004.

[46] T.J. Goff and G.M. Denton, “DIRECT SMELTING OF STAINLESS STEEL PLANT DUST,” in *Proceedings of the Tenth International Ferroalloys Congress*: *Cape Town, South Africa, 1 - 4 Februar 2004*, South African Institute of Mining and Metallurgy, Marshalltown, South Africa, 2004.

[47] G.M. Denton, “EAF Stainless Steel Dust Processing,” in *Sustainable Developements in Metals Processing*, pp. 273–284, 2005.

[48] M. Mortimer and P. Taylor, *Chemical kinetics and mechanism*, Royal Society of Chemistry : Open University, Cambridge, UK, 2002.

[49] M. P. Antony, R. Vidhya, C. K. Mathews et al., “Studies on the kinetics of the carbothermic reduction of chromium oxide using the evolved gas analysis technique,” *Thermochimica Acta*, vol. 262, pp. 145–155, 1995.

[50] N. S. S. MURTI and V. SESHADRI, “Kinetics of reduction of synthetic chromite with carbon,” *ISIJ International*, vol. 22, no. 12, pp. 925–933, 1982.

[51] M. E. Brown, *Introduction to Thermal Analysis*: *Techniques and Applications*, Springer Netherlands, Dordrecht, 2004.

[52] S. gVyazovkin, A. K. Burnham, J. M. Criado et al., “ICTAC Kinetics Committee recommendations for performing kinetic computations on thermal analysis data,” *Thermochimica Acta*, vol. 520, 1-2, pp. 1–19, 2011.

[53] P. Šimon, “Isoconversional methods,” *Journal of Thermal Analysis and Calorimetry*, vol. 76, no. 1, pp. 123–132, 2004.

[54] H. E. Kissinger, “Reaction Kinetics in Differential Thermal Analysis,” *Analytical Chemistry*, vol. 29, no. 11, pp. 1702–1706, 1957.

[55] R. L. Blaine and H. E. Kissinger, “Homer Kissinger and the Kissinger equation,” *Thermochimica Acta*, vol. 540, pp. 1–6, 2012.

[56] J. Farjas, N. Butchosa, and P. Roura, “A simple kinetic method for the determination of the reaction model from non-isothermal experiments,” *Journal of Thermal Analysis and Calorimetry*, vol. 102, no. 2, pp. 615–625, 2010.

[57] S. Vyazovkin, *Isoconversional Kinetics of Thermally Stimulated Processes*, Springer International Publishing, Cham, 2015.

[58] H. L. Friedman, “Kinetics of thermal degradation of char-forming plastics from thermogravimetry. Application to a phenolic plastic,” *Journal of Polymer Science Part C: Polymer Symposia*, vol. 6, no. 1, pp. 183–195, 1964.

[59] M.J. Starink, “The determination of activation energy from linear heating rate experiments: A comparison of the accuracy of isoconversion methods,” *Thermochimica Acta*, vol. 404, 1-2, pp. 163–176, 2003.

[60] T. Ozawa, “Kinetic analysis of derivative curves in thermal analysis,” *Journal of Thermal Analysis*, vol. 2, no. 3, pp. 301–324, 1970.

[61] C. D. Doyle, “Kinetic analysis of thermogravimetric data,” *Journal of Applied Polymer Science*, vol. 5, no. 15, pp. 285–292, 1961.

[62] J. H. gDowning, P. D. Deeley, and R. Fichte, “Chromium and Chromium Alloys,” in *Ullmann’s Encyclopedia of Industrial Chemistry*, Wiley-VCH Verlag GmbH & Co. KGaA, 2000.

[63] “PID Algorithm,” in *Process control*: *A practical approach,* M. King, Ed., pp. 35–111, Wiley, Southern Gate Chichester West Sussex United Kingdom, 2016.

[64] D. Chakraborty, S. Ranganathan, and S. N. Sinha, “Investigations on the carbothermic reduction of chromite ores,” *Metallurgical and Materials Transactions B*, vol. 36, no. 4, pp. 437–444, 2005.

[65] P. Weber and R. H. Eric, “The reduction of chromite in the presence of silica flux,” *Minerals Engineering*, vol. 19, no. 3, pp. 318–324, 2006.

11 List of Figures

12 List of Tables